

2-D TRANSITION METAL CYANIDE NANOSHEETS AS PRECURSOR
MATERIAL FOR AN ULTRA-LOW PLATINUM
GROUP METAL CATALYST

by

Tyler Nash, B.S., M.S.

A dissertation submitted to the Graduate Council of
Texas State University in partial fulfillment
of the requirements for the degree of
Doctor of Philosophy
with a Major in Materials Science, Engineering, and Commercialization
May 2014

Committee Members:

Gary W. Beall, Chair

Clois E. Powell

Benjamin R. Martin

Chang Ji

Vishag A. Badrinarayanan

COPYRIGHT

by

Tyler Nash

2014

FAIR USE AND AUTHOR'S PERMISSION STATEMENT

Fair Use

This work is protected by the Copyright Laws of the United States (Public Law 94-553, section 107). Consistent with fair use as defined in the Copyright Laws, brief quotations from this material are allowed with proper acknowledgment. Use of this material for financial gain without the author's express written permission is not allowed.

Duplication Permission

As the copyright holder of this work I, Tyler Lee Nash, authorize duplication of this work, in whole or in part, for educational or scholarly purposes only.

ACKNOWLEDGEMENTS

I would like to thank my advisor, Dr. Beall for his guidance throughout my academic career. I would also like to thank Dr. Martin, Dr. Powell, and Dr. Ji for taking the time to teach me many of the technical and problem solving skills I have acquired throughout my education. I would like to thank Dr. Badrinarayanan for his guidance in market research and commercial aspects of the program. I would like to acknowledge the learning experience and opportunity provided by the Director of the MSEC Program, Dr. Myers. The skills and knowledge imparted by the aforementioned individuals will be carried into my professional career and life. I would also like to thank all of the members of Dr. Beall's research group for their support and camaraderie.

Most of all I would like to thank my wife, Yelena, for her patience and understanding through the duration of the MSEC Program. Her knowledge of chemistry and high level of support helped me to overcome obstacles encountered along the way. Without her, I would not have achieved many of the accomplishments I have today. I would also like to thank my parents for supporting me throughout my education. I would not be in the place I am today had it not been for their persistent guidance and aid.

I would like to extend special thanks and acknowledgement to Analysys, Inc. and the Edwards Aquifer Research & Data Center for their assistance in ICP-AES analysis.

I would to acknowledge and thank the National Science Foundation for their support in the acquisition of instrumentation utilized in this paper under grant NSF-MRI

0821254 (Single Crystal diffractometer) and NSF-MRI 0923509 (Scanning Electron Microscope).

TABLE OF CONTENTS

	Page
ACKNOWLEDGEMENTS	v
LIST OF TABLES	ix
LIST OF FIGURES	x
ABSTRACT	xiv
 CHAPTER	
1. INTRODUCTION	1
1.1 An Introduction to 2-D Transition Metal Cyanide Materials	1
1.2 Background of the Problem	3
1.3 Bimetallic PGM Catalysts and Theory: A Solution.....	5
1.4 Methods of Bimetallic PGM Catalyst Synthesis	8
1.4.1 “Dry” and “Wet” Impregnation	8
1.4.2 Co-precipitation and Deposition/Precipitation	11
1.4.3 Colloidal Synthesis	12
1.4.4 Alternative Methods.....	13
1.4.5 Catalysts from Cyanide-Bridged Metal Precursors	14
2. EXPERIMENTAL METHODS.....	16
2.1 Preparation of the Catalyst Material	16
2.1.1 The “Dip and Dry Method” – No pH Modification	16
2.1.2 Nickel(II) desorption from activated carbon – pH Dependence.....	18
2.1.3 The “Precipitation Method” - pH Modification.....	19
2.1.4 The “Dip and Dry Method” - pH Modification	20
2.1.5 Standard Platinum Catalyst Preparation	21
2.2 Scanning Electron Microscopy and Energy-Dispersive X-Ray Spectroscopy	22
2.3 X-Ray Photoelectron Spectroscopy	22
2.4 Catalysis Testing Method – Hydrogenation of Styrene to Ethylbenzene.....	22
2.5 GC-MS and FID Analysis.....	23

2.6 ICP-AES Analysis	24
2.7 Wide Angle X-Ray Diffraction.....	25
3. RESULTS AND DISCUSSION	26
3.1 Preparation and Reduction of Nanosheets on Activated Carbon Substrate.....	26
3.1.1 The “Dip and Dry Method” – no pH Modification.....	27
3.1.2 Nickel(II) Desorption from Activated Carbon – pH Dependence.....	32
3.1.3 The “Precipitation Method” – pH Modification	38
3.1.3.1 SEM/EDS Analysis Before Pyrolysis	38
3.1.3.2 Thermogravimetric Analysis and Wide Angle X-Ray Diffraction of NiPt(CN) ₄	42
3.1.3.3 SEM/EDS Analysis After Pyrolysis	44
3.1.3.4 XPS Analysis	50
3.1.4 The “Dip and Dry Method” – pH Modification.....	53
3.1.5 ICP-AES Results.....	56
3.2 Styrene Hydrogenation Results.....	57
4. CONCLUSIONS.....	62
4.1 Summary	62
4.2 Future Work	62
APPENDIX SECTION	64
LITERATURE CITED	72

LIST OF TABLES

Table	Page
1. Concentration of reactants used in $\text{Ni}_x\text{Pt}_{(2-x)}(\text{CN})_4 \cdot 6\text{H}_2\text{O}$ synthesis on carbon	17
2. ICP-AES analysis method data from Anlaysys, Inc.	25
3. Quality assurance data from Analysys, Inc.....	25
4. Ni atomic percent and pH of carbon granules from Ni desorption experiment.....	33
5. Metal content of samples based on ICP-AES results.....	56
6. Styrene conversion on a platinum molar basis	61
A1-1. Internal standard calibration integration results plot 1	64
A1-2. Internal standard calibration integration results plot 2	65
A1-3. Internal standard calibration integration results plot 3	66
A3-1. GC-FID data for hydrogenation with raw activated carbon	70
A3-2. GC-FID data for hydrogenation with the 2 mM “precipitation method” catalyst	70
A3-3. GC-FID data for hydrogenation with the 4 mM “precipitation method” catalyst	70
A3-4. GC-FID data for hydrogenation with the 8 mM “precipitation method” catalyst	71
A3-5. GC-FID data for hydrogenation with the pH-modified “dip and dry method” catalyst.....	71
A3-6. GC-FID data for hydrogenation with the 8 mM platinum standard catalyst.....	71

LIST OF FIGURES

Figure	Page
1. Projections of $\text{Fe}(\text{H}_2\text{O})_2\text{Ni}(\text{CN})_4 \cdot 4\text{H}_2\text{O}$	2
2. Projections of $\text{Fe}(\text{H}_2\text{O})_2\text{Ni}(\text{CN})_4 \cdot \text{H}_2\text{O}$	3
3. Nickel(II) desorption experiment pH vs time plot.....	19
4. Untreated activated carbon	27
5. SEM images of the “1 (1:20 Pt:Ni)” sample (A) before and (B) after pyrolysis.....	28
6. SEM images of the “1/8th (1:20 Pt:Ni)” sample (A) before and (B) after pyrolysis....	29
7. SEM images of the “1/8th (2:3 Pt:Ni)” sample (A) before and (B) after pyrolysis.....	29
8. SEM images of the “salts only” sample (A) before and (B) after pyrolysis.....	30
9. SEM image and EDS data from the “1 (1:20 Pt:Ni)” sample before pyrolysis.....	31
10. SEM image and EDS data from the “1/8th (2:3 Pt:Ni)” sample before pyrolysis.....	31
11. SEM image and EDS data from the “salts only” sample before pyrolysis	32
12. SEM image and EDS data from granule 1	34
13. SEM image and EDS data from granule 2.....	34
14. SEM image and EDS data from granule 3	35
15. SEM image and EDS data from granule 4.....	35
16. SEM image and EDS data from granule 5	36
17. SEM image and EDS data from granule 6.....	36
18. SEM image and EDS data from granule 7	37

19. SEM image and EDS data from granule 8.....	37
20. SEM image and EDS data from granule 9.....	37
21. SEM images of the 2 mM “precipitation method” sample before pyrolysis	39
22. SEM image and EDS data from the 2 mM “precipitation method” sample before pyrolysis.....	39
23. SEM images of the 4 mM “precipitation method” sample before pyrolysis	40
24. SEM images of the 8 mM “precipitation method” sample before pyrolysis	41
25. SEM image and EDS data from the 4 mM “precipitation method” sample before pyrolysis.....	41
26. SEM image and EDS data from the 8 mM “precipitation method” sample before pyrolysis.....	42
27. Weight percent versus temperature plot showing water loss in air	43
28. PtNi(CN) ₄ •6H ₂ O powder diffraction pattern with tentative peak assignments	44
29. SEM images of the 2 mM “precipitation method” sample after pyrolysis.....	45
30. SEM images of the 4 mM “precipitation method” sample after pyrolysis	45
31. SEM images of the 8 mM “precipitation method” sample after pyrolysis	46
32. SEM images of the 2 mM “precipitation method” sample after pyrolysis	47
33. SEM image and EDS data from the 2 mM “precipitation method” sample after pyrolysis.....	48
34. SEM image and EDS data from the 4 mM “precipitation method” sample after pyrolysis.....	48
35. SEM image and EDS data from the 8 mM “precipitation method” sample after pyrolysis.....	49

36. XPS data for the platinum 4f5/2 and 4f7/2 peaks of the 8 mM sample before pyrolysis	51
37. XPS data for the platinum 4f5/2 and 4f7/2 peaks of the 8 mM sample after pyrolysis	52
38. SEM images of the pH-modified "dip and dry method" sample before pyrolysis	54
39. SEM image and EDS data from the pH-modified "dip and dry method" sample before pyrolysis	54
40. SEM images of the pH-modified "dip and dry method" sample after pyrolysis	55
41. SEM image and EDS data from the pH-modified "dip and dry method" sample after pyrolysis	55
42. Molar loading versus reactant concentration	57
43. Concentration versus time plot for pH-modified "dip and dry method" catalyst	59
44. Concentration versus time plot for 2 mM "precipitation method" catalyst	60
45. Concentration versus time plot for 4 mM "precipitation method" catalyst	60
46. Concentration versus time plot for 8 mM "precipitation method" catalyst	61
47. Concentration versus time plot for 8 mM standard catalyst	61
A1-1. Internal standard calibration plot 1	64
A1-2. Internal standard calibration plot 2	65
A1-3. Internal standard calibration plot 3	66
A2-1. Electron trajectories in Monte Carlo simulation	67
A2-2. Electron energy by position	67
A2-3. X-ray intensity as a function of depth from the sample surface – platinum	68
A2-4. X-ray intensity as a function of depth from the sample surface – nickel	68

A2-5. X-ray intensity as a function of depth from the sample surface – carbon	69
---	----

ABSTRACT

Two methods were developed to coat activated carbon with $\text{NiPt}(\text{CN})_4$ nanosheets by reacting potassium tetracyanoplatinate(II) with nickel(II) sulfate in the presence of the carbon substrate. The modification of pH released nickel(II) ions from the carbon surface to participate in the reaction. Upon pyrolysis, a Pt-Ni alloy was formed. Based on EDS and XPS data, platinum had segregated to the surface of the metallic structure in higher concentration samples. The Pt-Ni catalyst exhibited significant activity in the hydrogenation of styrene to ethylbenzene. When compared to a catalyst prepared by traditional methods, the Pt-Ni catalyst prepared from $\text{NiPt}(\text{CN})_4$ nanosheet precursors exhibited up to 2.8x the activity on a platinum metal basis.

CHAPTER 1

Introduction

1.1 An Introduction to 2-D Transition Metal Cyanide Materials

Metal cyanide-bridged frameworks such as the pigment Prussian blue have been used in various applications as pigments, medicine, and analytical chemistry reagents. More recently such frameworks have been used as polymerization catalysts.^{1,2} Another class of metal cyanide-bridged frameworks is the Hofmann-type clathrates, which have been studied for their unique structural properties.^{3,4} These compounds are composed of two-dimensional networks of square planar nickel atoms linked via cyanide bridges to another metal that forms octahedral coordination with the four bridging cyanide ligands and two molecules, typically amines, on either side of the sheet. Aromatic interlayer molecules usually occupy space between the layers in a Hofmann-type clathrate. The structures utilized in this work are similar to these clathrates, with the exception that the amines and aromatic compounds are not present. Structural studies have been carried out on three similar compounds; $\text{Ni}(\text{H}_2\text{O})_2\text{Ni}(\text{CN})_4 \cdot 4\text{H}_2\text{O}$, $\text{Co}(\text{H}_2\text{O})_2\text{Ni}(\text{CN})_4 \cdot 4\text{H}_2\text{O}$ and $\text{Cd}(\text{H}_2\text{O})_2\text{Ni}(\text{CN})_4 \cdot 4\text{H}_2\text{O}$.^{5,6,7} Work at Texas State University resulted in the solutions to two more structures of this type, $\text{Fe}(\text{H}_2\text{O})_2\text{Ni}(\text{CN})_4 \cdot 4\text{H}_2\text{O}$ and $\text{Mn}(\text{H}_2\text{O})_2\text{Ni}(\text{CN})_4 \cdot 4\text{H}_2\text{O}$.⁸ A partially dehydrated structure, $\text{Fe}(\text{H}_2\text{O})_2\text{Ni}(\text{CN})_4 \cdot \text{H}_2\text{O}$, was also solved in this body of work. The structures of $\text{Fe}(\text{H}_2\text{O})_2\text{Ni}(\text{CN})_4 \cdot 4\text{H}_2\text{O}$ and $\text{Fe}(\text{H}_2\text{O})_2\text{Ni}(\text{CN})_4 \cdot \text{H}_2\text{O}$ are shown in Figure 1 and Figure 2, respectively. A structure of this type with varying octahedral coordinated metals will be referred to as $\text{M}(\text{H}_2\text{O})_2\text{Ni}(\text{CN})_4 \cdot 4\text{H}_2\text{O}$, where M refers to transition metals in the +2 valence state such as iron(II), manganese(II), nickel(II), cadmium(II), cobalt(II), copper(II), and others.

A method for separating individual nanosheets of these materials from the parent $M(H_2O)_2Ni(CN)_4 \cdot 4H_2O$ compounds used intercalation and subsequent exfoliation in dodecyl pyrrolidone (DDP). This was confirmed by atomic force microscopy (AFM) and scanning electron microscopy (SEM). This dissertation utilizes knowledge and understanding of the structure and behavior of these systems gained in our previous work. This work focuses on the use of these nanosheets for precursors for ultra-low platinum group metal (PGM) catalysts.

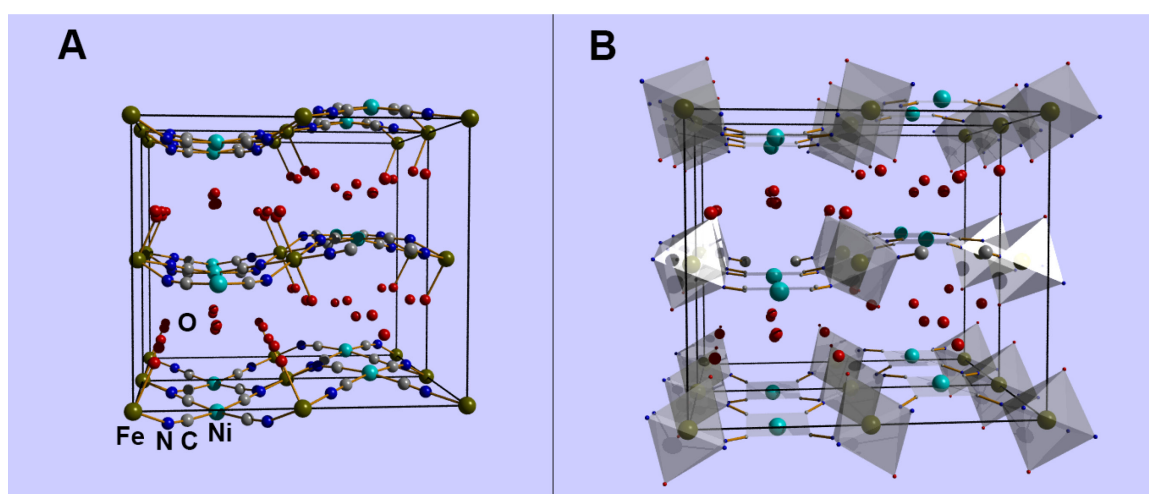


Figure 1. Projections of $Fe(H_2O)_2Ni(CN)_4 \cdot 4H_2O$. A (A) ball and stick projection of $Fe(H_2O)_2Ni(CN)_4 \cdot 4H_2O$ down the c-axis is shown along with a (B) representation of the octahedral and square planar coordination down the same axis. The unit cell is denoted by the black lines around the structures.

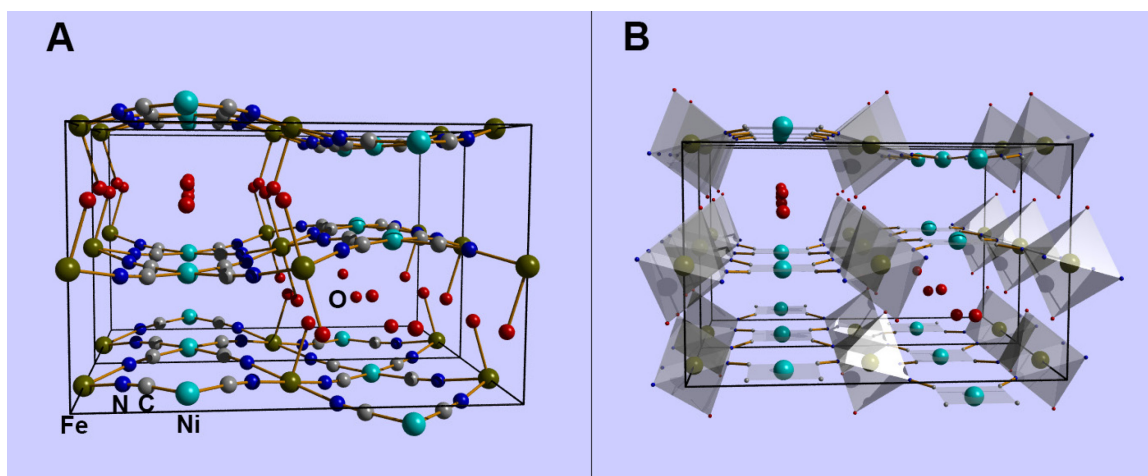


Figure 2. Projections of $\text{Fe}(\text{H}_2\text{O})_2\text{Ni}(\text{CN})_4 \cdot \text{H}_2\text{O}$. A (A) ball and stick projection of $\text{Fe}(\text{H}_2\text{O})_2\text{Ni}(\text{CN})_4 \cdot \text{H}_2\text{O}$ down the a-axis is shown along with a (B) representation of the octahedral and square planar coordination down the same axis. The unit cell is denoted by the black lines around the structures.

1.2 Background of the Problem

Traditionally, Platinum group metal (PGM) catalysts have utilized high loadings of pure precious metals to achieve the activity required for catalysis. Only the metal exposed on the surface of these catalysts is active. Therefore, traditional PGM catalysts are only able to use a small percentage of the total PGM, resulting in a very inefficient use of the metals. The high precious metal content renders this type of catalyst component very costly and sensitive to price fluctuation in platinum group metals. There has been a substantial effort by researchers to find alternative catalysts that use lower precious metal content or non-precious metal alternatives to achieve the same activity.

Two recent drivers have accelerated the need for a solution to the PGM catalyst problem:

- 1) *Fuel cells* – for portable power units, large stationary power units, and transportation – as a source of clean alternative energy have a significant cost barrier associated with large-scale commercialization. One study found that the

catalysts typically comprise 21% of the cost of a fuel cell.⁹ The Department of Energy's Fuel Cell Technologies Office Multi-Year Research, Development and Demonstration Plan established the following goals for fuel cell catalysts:¹⁰

- PGM total loading of 0.125 mg PGM/cm² electrode area and 0.125 g/kW output by 2017 for proton exchange membrane (PEM) fuel cells.
- For direct methanol fuel cells (DMFC), PGM loading of <2.7 mg Pt/cm² by 2015.
- For phosphoric acid fuel cells, PGM loading of 0.35 mg Pt/cm² by 2018.

2) *Increasing emissions regulations* around the globe strains the capabilities of currently used autocatalysts. Of all the platinum sold (by weight) in 2011, 31% was used in the manufacture of autocatalysts.¹¹ Of all palladium sold, 68% was used for autocatalysts.¹² Of all rhodium sold, 69% was used for auto catalysts.¹³ These numbers indicate the importance of use PGM catalysts in the automotive industry. In the United States, California has taken the lead with its Low and Zero Emissions Vehicle programs; the rest of the United States has followed suit with similar regulations. The European Union has enacted its "Euro 5" standards in 2010, and will begin enforcing more stringent "Euro 6" standards in 2014. The catalyst component is key in emissions reduction. More efficient PGM catalyst technology is required to keep costs down after new regulations are introduced.

The subset of autocatalysts impacted the most by new regulation is the heavy duty diesel autocatalyst. Diesel engines do not burn at an ideal air/fuel ratio like gasoline engines; they burn with a high excess of air in the mixture. This "lean burn" requires higher activity heavy duty diesel (HDD) catalysts to neutralize the exhaust emissions. HDD

catalysts typically contain more platinum than standard catalysts to meet emission standards which drives up the cost. New diesel regulations have been introduced in regions such as China, Russia, India, Brazil, and the Republic of Korea.¹⁴ To keep diesel vehicles cost-effective, a catalyst technology that reduces the amount of PGM is required. These new restrictions are driving the search for a more efficient HDD catalyst that uses smaller amounts of precious metals.

The previously mentioned new driving factors have accelerated the push for ultra-low PGM catalysts. Many existing technologies also strive to reduce catalyst cost and increase catalyst efficiency for certain processes. Ultra-low PGM catalysts are beneficial as petroleum refining catalysts and chemical processing catalysts that have significant PGM content. One industrially significant catalytic reaction is the hydrogenation of organic compounds. Current catalysts have challenges associated with selectivity toward the desired product, not being cost effective, and inefficient utilization of the PGMs in the catalyst. New, more efficient catalysts are actively sought for this family of reactions.

1.3 Bimetallic PGM Catalysts and Theory: A Solution

Many efforts are being directed toward ultra-low PGM catalysts and non-PGM catalysts. The literature review will focus on the most relevant advances toward ultra-low PGM catalysts that lead to the work proposed in this dissertation.

Alloying PGMs with other metals in binary and ternary alloys is an effective method of increasing activity in oxygen reduction reactions (ORR) and hydrogenation reactions with decreasing platinum content. The ORR reaction is the reaction that occurs at the cathode of a fuel cell. The driving factor is thought to be the change in Pt-Pt nearest-neighbor distance upon alloying.^{15,16,17} The ORR is not fully understood. The rate

determining step in the ORR reaction is the rupture of the O-O bond by a dual-site mechanism.¹⁸ The Pt-Pt distance decreases upon alloying with different metals. As it nears the optimal distance for O-O binding, activity in the catalyst system increases.¹⁶ Increased ORR activity upon alloying is also due to an increase in platinum d-band vacancies.^{19,20} Ternary Pt alloys have increased ORR catalytic activity over binary catalysts to four times that of Pt alone.²¹

At the anode side of the fuel cell, a Pt/Ru catalyst is the mainstay in DMFCs.²² Ru must be added to prevent the Pt from CO poisoning. Ru is an expensive precious metal. Research shows the viability of other Pt/metal complexes for the anode side of the fuel cell.²³ Work done on PEM fuel cell anodes is focused on reduction of the Pt content and full utilization of Pt metal rather than alloying.^{24,25,26,27} PGM/non-PGM alloys at the anode can significantly reduce the amount of Pt required. Research has tended to focus on the reduction of Pt at the anode via thinner Pt layers. More needs to investigate the use of alloys such as Pt/Ni.

Advances in the development of heterogeneous hydrogenation catalysts have shown that single atoms can be highly selective and catalytically active.^{28,29,30} By dispersing single atoms on the surface of a support, 100% utilization of PGMs can be achieved. A study by Kyriakou et al., shows that higher hydrogenation activity and high selectivity is achieved by dispersing single Pd atoms onto a Cu surface.³¹ For bulk PGM catalysts, a trade-off occurs between facile dissociation of hydrogen and weak binding of intermediates. It is desirable to have both traits for high activity and high selectivity. In the study, both facile dissociation of hydrogen and weak binding of intermediates can be achieved by a synergistic relationship between the single Pd atoms and the bulk Cu. The

Pd atoms dissociated the hydrogen, which desorbed onto the neighboring Cu atoms for weak intermediate binding with the Cu. Other studies indicated simultaneous increase of hydrogenation activity and selectivity using bimetallic catalysts.³² Han, et al. reported that Pt bimetallic catalysts with Cr, Mn, Fe, Co, Ni and Cu increased activity and selectivity for hydrogenation of chloronitrobenzene.³³ The activity for hydrogenation of nitrobenzene in a Pd/Ni system was found to be 3.5 times that of pure Pd.³⁴ Bimetallic catalysts reduce cost, improve selectivity, and increase the activity of hydrogenation catalysts. The synergistic mechanisms of different bimetallic systems warrant further research.

One of the primary concerns in the regulation of diesel emissions is the ability to convert harmful NO_x emissions to N₂. It is difficult to convert NO_x to N₂ in the lean burning conditions of diesel vehicles. The catalyst becomes “oxygen-poisoned” under these conditions. Oxygen poisoning occurs due to the catalyst’s high affinity for O₂. The catalyst becomes saturated with O₂, inhibiting NO adsorption and dissociation. One solution involves the trapping of NO_x emissions and periodically initiating a rich burn cycle in which the NO_x is released and converted to N₂.^{35,36,37} Reversing to rich burn can be an effective way to convert NO_x to N₂, but it reduces fuel economy and NO_x trap storage can be hindered by sulfates.³⁸ A more direct solution to the NO_x conversion problem is through the use of selective catalytic reduction. The catalyst is tailored to reduce NO_x in the presence of O₂. Studies show that Pt on alumina support converts NO_x with high activity in the presence of CO, hydrogen, or propene.³⁹ When NO_x binds to the surface, a decomposition step leaves oxygen on the Pt site. This blocks the site from reacting with other NO_x molecules. The CO, hydrogen, or propene molecules reduce the

absorbed oxygen. The site is again available to react with NO_x . In the hydrogenation work by Kyriakou, et al, atoms can desorb from Pd atoms to a weak binding Cu atom.³⁰ A bimetallic catalyst with isolated Pt atoms may function in a similar way for NO_x conversion to N_2 . The catalyst prepared in this work is a prime candidate for this investigation.

1.4 Methods of Bimetallic PGM Catalyst Synthesis

A myriad of methods are available to synthesize bimetallic catalysts. The method to be used depends on the desired loading, particle size, atomic arrangement, crystal orientation, and morphology. The method of preparation will also differ based on whether the product will be used in fundamental studies or commercial applications. Common methods of preparation for fundamental studies include electron beam sputtering, magnetron sputtering, pulsed laser deposition, and physical evaporation using a thermal filament.⁴⁰ These physical vapor deposition methods are used for preparing very high purity bimetallic surfaces for fundamental ultra-high vacuum studies and are not commercially viable. Commercially viable methods exist for preparation of bimetallic catalysts. These methods are directed toward cost-effective synthesis of the catalyst on a support and will be the focus of the remainder of this section.

1.4.1 “Dry” and “Wet” Impregnation

Impregnation is one of the most common methods used for bimetallic catalyst synthesis. The first step of this method is to immerse the support in a solution of the catalyst precursor. “Dry”, or “incipient wetness” impregnation, is the term used when the volume of precursor solution is less than the volume of the pores in the support.⁴¹ When excess precursor solution is used, the method is termed “wet” or “soaking” impregnation.

The most common solvent is water. Acetone⁴², toluene⁴³, ethylene glycol⁴⁴, and formic acid⁴⁵ have also been reported. Factors that affect loading are concentration of precursor solution and the affinity of the support for adsorption of the precursor.

After soaking the support in the precursor solution, the support is dried at temperatures ranging from 80 °C to 200 °C.¹⁵ The temperature ramp, final temperature, and drying atmosphere determine the distribution of the catalyst precursor on the surface of the support.⁴⁶ Slow evaporation rates, in which the solution on the support surface evaporates first, causes migration of the precursor with the solution into the pores of the support, resulting in little deposition on the support's external surface. Very fast drying rates can cause temperature gradients, resulting in the solution being pushed to the surface and deposition primarily on the surface. To obtain uniform deposition, the drying rate should be faster than the rate of diffusion and homogenization of the solution, but it should not be so high that a significant temperature gradient is formed.

After drying, the catalysts are calcined at elevated temperatures to decompose the metal precursor to leave a metal oxide. Each system has an ideal temperature range for calcination in which the metals are most evenly distributed. A volcano-type relationship between catalytic activity and calcination temperature is common.⁴⁷ The final step in the process is reduction, usually in dilute hydrogen atmosphere, to yield the metallic catalyst. Sometimes the calcination step is skipped, and the decomposition and reduction to metallic state occurs in the same step.

The sequence of impregnation of the two metals has a significant effect on the properties of the catalyst. Metals can be deposited sequentially by two complete impregnation, drying, and calcination/reduction cycles with a different metal precursor.

The order of impregnation plays a role in the activity and selectivity of the catalyst. In a Pt-Ni system, catalysts with Pt-first impregnation showed significantly more activity than Ni-first impregnation.⁴⁸ Simultaneous, or co-impregnation, involves one impregnation cycle with both metals present in the precursor solution. Bimetallic catalysts prepared by simultaneous impregnation have higher activity than those prepared via sequential impregnation.⁴⁹ Simultaneous impregnation may present homogeneity problems when one metal precursor absorbs preferentially over another.

Traditionally, metallic salts have been used as precursors, but organometallic compounds exhibit significant advantages over metallic salts as precursors for bimetallic catalysts.^{50,51,52} Organometallic precursors require only one impregnation step, avoiding sequential impregnation of two metals. The bimetallic bond is already present in many cases, leading to a higher number of bimetallic bonds in the final product. This leads to increased activity and selectivity. Organometallic clusters have been used to deliver metals into the support pores and surfaces in the desired atomic ratios.^{53,54,55,56} Clusters can avoid the problem of preferential diffusion into support pores of one precursor over another. Organometallic cluster-derived catalysts have exhibited increased activity and selectivity over traditional metallic salt impregnation catalysts. This is not always the case, and the bimetallic bonds are not always retained.⁵⁷ Organometallic and organometallic cluster precursors can be expensive to produce and difficult to synthesize, and production of catalysts from them requires close control over many factors, leading to expensive large-scale production.⁵⁸

1.4.2 Co-precipitation and Deposition/Precipitation

Co-precipitation and deposition precipitation are common synthetic methods for monometallic and bimetallic catalysts.^{15,59,60,61,62} In co-precipitation, a solution containing precursor(s) for the catalyst and precursor(s) for the support are present in solution. Base is vigorously mixed into the solution, causing the precipitation of hydroxides or carbonates. Precipitation conditions such as pH, stir rate, temperature, reaction time, and order and rate of reactant addition must be carefully controlled. After precipitation, the product is washed and filtered with the appropriate agent and procedure. After washing, the precipitate is calcined and/or reduced in a manner similar to that in the impregnation method. The atmosphere must be carefully controlled to achieve homogeneity, avoid metal segregation, and avoid formation of unwanted impurities or poisons such as sulfides.

Deposition/precipitation is similar to co-precipitation, but the support is already present in the reaction slurry. Metal hydroxides/carbonates are precipitated onto the support surface by the addition of base. Controlling the rate and point of nucleation of the hydroxides/carbonates is crucial to obtaining a catalyst with high homogeneity. This has been attained by using urea as a source of ammonium hydroxide.⁶³ The urea can be homogenized in solution, and then heated to release ammonium hydroxide uniformly. Reactions between the precipitate or the precursor and the support have been shown to increase homogeneity.

Although a common monometallic catalyst, Ni on alumina support, is commercially prepared by precipitation methods, scale-up of precipitation syntheses can be difficult.¹⁵ The aforementioned factors that affect precipitation, such as efficient

mixing, pH, temperature, reaction time, and order and rate of reactant addition, must be closely controlled. The addition of a second metallic component in bimetallic precipitation can further complicate these issues. Industrial processing often requires the addition of additives to bind precipitates in forms such as pellets and prevent unwanted by-products from forming.

1.4.3 Colloidal Synthesis

In colloidal synthesis, bimetallic colloids are formed and then adhered to a substrate. To form the colloidal particles, metal salts are added to a solution containing cationic surfactants to react and form micelle-like organometallic formations with metal clusters. The dispersion is heated under reducing conditions or exposed to a reducing agent to produce bimetallic nanoparticles. For example, Pt-Pd nanoparticles can be formed by adding K_2PdCl_4 and K_2PtCl_4 to tetradecyltrimethylammonium bromide with subsequent reduction using NaBH_4 .⁶⁴ After formation of the nanoparticles, they are dried and re-dispersed in a solvent for uniform dispersion and suspension. Adherence of the nanoparticles to the support has been achieved by impregnation and/or adsorption followed by sonication or heating and by grafting particles to the surface by coordinating ligands.^{65,66,67} Colloidal synthesis can provide excellent control over stoichiometry and size distribution in some systems, but carbon contamination from the decomposition of surfactants is a persistent issue.¹⁴

Core-shell nanoparticle synthesis is a variation of colloidal synthesis. Core nanoparticles are synthesized via colloidal synthesis – commonly using ethylene glycol as the solvent, polyvinyl alcohol as the surfactant, and NaBH_4 as the reducing agent. The core is coated with one or few-layer PGM shells by exposure to solutions of PtCl_2 at

elevated temperature.⁶⁸ Nanoparticles can be affixed to the support using similar methods as those in standard colloidal synthesis. Core-shell structures have been produced by annealing Pt-Co nanoparticles in a CO environment.⁶⁹ Co@Pt, Ni@Pt, and Fe@Pt core-shell catalysts exhibit potential as high activity, low cost replacements for commercial platinum catalysts in NH_3BH_3 hydrolysis.^{70,71}

Reverse micelle synthesis is similar to colloidal synthesis of bimetallic catalysts with a narrow size distribution of nanoparticles.^{72,73} The metal precursor is dissolved in the presence of a nonionic surfactant in aqueous media. The reducing agent is dissolved in an oil phase and added to the solution with stirring. Reverse micelles are formed, allowing the reduction of the precursor to metallic nanoparticles. To immobilize the nanoparticles to a support, the reverse micelles are disrupted with a solvent such as acetone. This method is advantageous because it allows control of over particle size via water-to-surfactant ratio and the amount of reducing agent to control micelle size and nucleation rate, respectively.

1.4.4 Alternative Methods

Several other methods of synthesis exist to produce bimetallic catalysts. Many of these methods involve deposition of a second metal onto a preexisting monometallic catalyst. Reductive deposition precipitation is a notable method of this type. In reductive deposition precipitation, a preexisting monometallic catalyst is exposed to a hydrogen atmosphere to adsorb hydrogen on the surface. The catalyst is exposed to a precursor of the second metal. The metal reacts with the surface hydrogen and is reduced in the hydrogen atmosphere. The primary result is an alloy with bimetallic bonds, but it has been observed that the secondary metal also occurs in isolated deposits on the support in

Pt-Ge and Rh-Ge systems.^{74,75} Pt-Sn and Pt-Ga are other examples of catalysts that have been prepared via reductive deposition precipitation.^{76,77}

Dendrimer-encapsulated nanoparticles have been used to synthesize bimetallic catalysts.^{78,79,80} The nanoparticles are formed by extracting metallic precursor ions on dendrimers terminated by hydroxyl, followed by chemical reduction of the precursors. The particle size can be precisely controlled by controlling the size of the dendrimer. The resulting particles are highly monodisperse. The nanoparticles, typically under 3 nm, are immobilized on a support via impregnation.

Microwave-assisted polyol reduction (MAPR)⁸¹, instead of calcination/pyrolysis or chemical reduction, reduces impregnation-prepared catalysts using a microwave reactor. MAPR has very high energy efficiency. The reduction can be performed in a matter of minutes or seconds. This method can lead to high homogeneity by shortening crystallization time and reducing surface mobility.

1.4.5 Catalysts from Cyanide-Bridged Metal Precursors

Research has shown that cyanide-bridged metal compounds are suitable precursors for bimetallic catalysts. Work by Di Noto, et al. has focused on the use of 3-D networks of cyanide-bridged metals and organic binders as precursors to produce Pt-Ni, Pt-Fe, and Pd-Co bimetallic catalysts.^{82,83,84,85,86,87} This method of catalyst preparation resulted in a bimetallic catalyst material supported on a carbon nitride core. The precursor was prepared via the combination of a tetracyano- or hexacyano-metallate and a salt of the second metal in the presence of an organic binder such as sucrose. The result was a polymeric cyanide-bridged metal structure with the organic binder coordinated in different positions in the structure. In the precursor material, the organic binder acted as a

source of carbon and/or nitrogen for the formation of a carbon nitride core upon thermal treatment. After precursor preparation, a two-step thermal treatment was administered, and an activation step was used to prepare the final catalyst product. Surface platinum atom concentration increased with increasing temperature in the second thermal treatment step for the Pt-based catalysts. It was suggested that these carbon nitride bimetallic catalyst particles could be supported via various metal oxide supports.

The process presented in this manuscript differs from that developed by Di Noto, et al. The precursor presented here does not contain an organic binder. It is comprised of individual sheets of cyanide-bridged Pt and Ni metals, with the empirical formula $\text{PtNi}(\text{CN})_4 \cdot x\text{H}_2\text{O}$, where x is the degree of hydration between individual layers. Activated carbon is coated with a thin layer of this precursor that is atomically thick to multiple layers thick. The thermal treatment utilized by Di Noto, et al. requires two steps. The thermal treatment herein requires one pyrolysis step. At temperatures less than 500 °C, nickel was found in higher surface concentrations in the process by Di Noto, et al.⁸³ Platinum concentration was found to segregate to the surface over nickel at 450 °C in the work described here. The process developed in this work can be extended to other bimetallic and trimetallic catalysts by varying the metal precursors and their stoichiometric ratios. The coating process is versatile and can be adapted to a variety of different substrates, depending on the application.

CHAPTER 2

Experimental Methods

2.1 Preparation of the Catalyst Material

Three methods were explored to coat an activated carbon substrate with layers of $\text{Ni}_{(1+x)}\text{Pt}_{(1-x)}(\text{CN})_4 \cdot 6\text{H}_2\text{O}$ nanosheets. The first method, termed the “dip and dry” method, involved the submersion of the substrate into two different reactants with subsequent drying after each submersion. This method ultimately did not result in the formation of the desired $\text{Ni}_{(1+x)}\text{Pt}_{(1-x)}(\text{CN})_4 \cdot 6\text{H}_2\text{O}$ precursor. The second method, termed the “precipitation method”, involved precipitation of $\text{Ni}_{(1+x)}\text{Pt}_{(1-x)}(\text{CN})_4 \cdot 6\text{H}_2\text{O}$ nanosheets in the presence of the activated carbon substrate. This resulted in the successful coating of the carbon with layers of $\text{Ni}_{(1+x)}\text{Pt}_{(1-x)}(\text{CN})_4 \cdot 6\text{H}_2\text{O}$. The third method, a pH-modified “dip and dry” method, ultimately resulted in the formation of $\text{Ni}_{(1+x)}\text{Pt}_{(1-x)}(\text{CN})_4 \cdot x\text{H}_2\text{O}$ on the surface of the activated carbon. A standard platinum catalyst was prepared via a common conventional impregnation method for comparison with the bimetallic catalysts.

Caution: Cyanogen and hydrogen cyanide gases are formed during pyrolysis of the precursor compounds. All work must be performed under a hood with proper precautionary measures in place.

2.1.1 The “Dip and Dry Method” – No pH Modification

For each trial, 1 g of activated carbon (Aqua Solutions, 8-12 mesh, coconut-derived) was weighed and placed in a mesh steel basket for submersion. In the first submersion, dilute solution of either potassium tetracyanonickelate hydrate (Aldrich) or potassium tetracyanoplatinate trihydrate (Alfa Aesar, 99.9%) were prepared. The mesh steel basket containing the activated carbon was submerged in the solution and placed

under vacuum for 20 minutes to facilitate filling the pores of the activated carbon. The steel basket was hung in an oven at 80 °C to dry for 1 hour. A second dilute solution was prepared with nickel(II) sulfate hexahydrate (Alfa Aesar, 98%) or a combination of nickel(II) sulfate hexahydrate and sodium tetrachloroplatinate trihydrate (Alfa Aesar, Premion® 99.95%) in a 250mL beaker. The mesh steel basket containing the treated activated carbon was submerged in the solution and held under vacuum for 20 minutes. After releasing vacuum, the tea ball was hung to dry in an oven at 80 °C for 1 hour. The concentrations of reactants used are shown in Table 1. Note that the “Salts only” samples contains no tetracyanometallate. This sample was used as a reference to determine if the desired structures were formed on the surface of the carbon.

Table 1. Concentration of reactants used in $\text{Ni}_x\text{Pt}_{(2-x)}(\text{CN})_4 \cdot 6\text{H}_2\text{O}$ synthesis on carbon.

Name	$\text{K}_2\text{Ni}(\text{CN})_4 \cdot \text{H}_2\text{O}$ (mM)	$\text{NiSO}_4 \cdot 6\text{H}_2\text{O}$ (mM)	$\text{Na}_2\text{PtCl}_4 \cdot 3\text{H}_2\text{O}$ (mM)
1 (1:20 Pt:Ni)	4.000	4.000	0.4000
1/8th (1:20 Pt:Ni)	0.5000	0.5000	0.05000
1/8th (1:20 Pt:Ni, "Salts only")	0.0000	1.0000	0.05000
1/8th (2:3 Pt:Ni)	0.5000	0.5000	0.6667

After treating the activated carbon, the granules were placed in a furnace to undergo pyrolysis. A Lindberg 54232 tube furnace with a Lindberg 59344 power supply and controller was used. A TA PMR2-010011 flow controller was used to control Ar and H_2 flow. The granules were placed in a quartz boat, and the boat was placed inside a quartz tube with a smaller ceramic tube as a liner. The tube was purged for a minimum of 2 hours under a flow of 135 mL/min Ar. After purging with argon, hydrogen was introduced into the tube with H_2 flow of 5-7 mL/min and an Ar flow of 125 mL/min. The

heating was started after 15 minutes at these settings. The timer was started after the furnace reached the target temperature. Samples were held at 450 °C for 2 hours. After heating ceased, H₂ flow was stopped, and Ar flow was reduced to 30 mL/min until the furnace cooled. The boat was removed from the furnace, and the granules were placed in a desiccator for storage.

2.1.2 Nickel(II) Desorption from Activated Carbon – pH Dependence

Based on the results of the original “dip and dry method”, a new procedure was employed to coat activated carbon with Ni_(1+x)Pt_(1-x)(CN)₄•6H₂O sheets. This procedure incorporated a pH modification step to facilitate the release of nickel(II) from the activated carbon surface.

An experiment was carried out to determine at what pH the nickel(II) is completely released from the surface. First, 0.0263 g of NiSO₄•6H₂O was added to 200 mL of deionized water. The pH was 5.01. A mass of 1.0005 g activated carbon was added to the solution and stirred for 5 minutes. The pH was 7.68 after stirring. The beaker containing the solution and activated carbon was placed under vacuum for 20 minutes. After releasing vacuum, the activated carbon was placed in a mesh steel basket and placed in an oven to dry at 80 °C. After the drying, the activated carbon was submerged in 200 mL deionized water and placed under vacuum for 20 minutes. The pH was 7.71. Over the course of 2 hours and 45 minutes, the pH of the stirred solution was lowered using dropwise addition of 1.18 M HCl. Single carbon granules were removed from the solution at different intervals as the pH was lowered. Upon removal, the granules were dried at 80°C. In Figure 3, a pH versus time plot shows the intervals at which samples were taken and HCl was added. The pH rose slowly between additions of HCl. The

carbon granules were analyzed for surface features and nickel content using scanning electron microscope imaging and energy-dispersive X-ray spectroscopy.

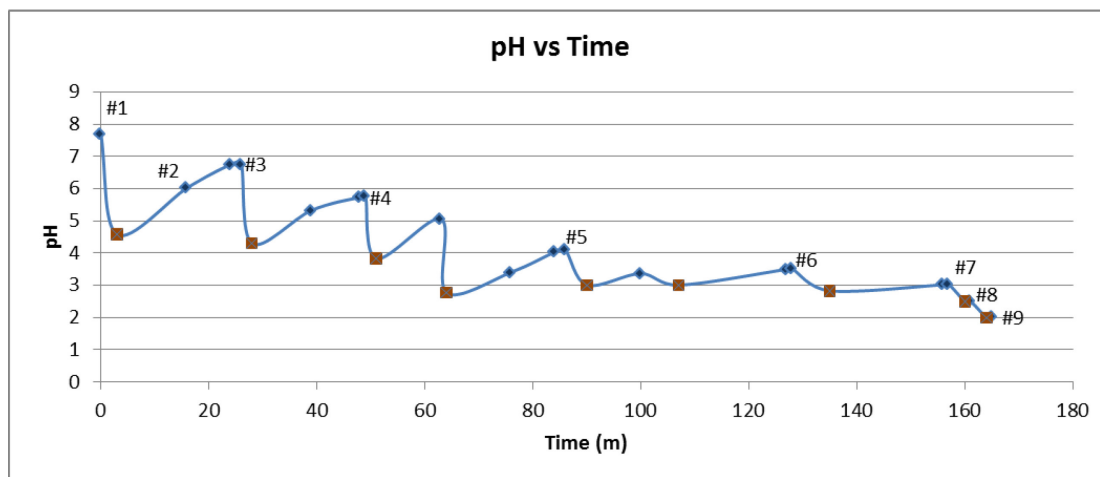



Figure 3. Nickel(II) desorption experiment pH vs time plot. The numbers indicate the time and pH at which granules were removed, and the “” symbol indicates when HCl was added.

2.1.3 The “Precipitation Method” - pH Modification

This method involved the precipitation of $\text{Ni}_x\text{Pt}_{(2-x)}(\text{CN})_4 \cdot 6\text{H}_2\text{O}$ sheets in the presence of activated carbon. Reactant concentrations of 8 mM, 4 mM, and 2mM were used in three separate syntheses. One 50 mL solution of potassium tetracyanoplatinate(II) was prepared, and another 50 mL solution of nickel(II) sulfate was prepared. While stirring, 0.25 g of activated carbon was placed in the nickel(II) sulfate solution and placed under vacuum for 20 minutes. The solution was brought to pH 3.00 by dropwise addition of HCl. The pH was considered stable when it did not rise by more than 0.10 in a 5 minute time span. Upon meeting this criterion, the potassium tetracyanoplatinate(II) solution was added over a period of 6 minutes. The solution was stirred for 30 minutes. The solutions took on a cloudy appearance in the 8 and 4 mM concentration syntheses. After stirring, the solution was placed under vacuum for 20 minutes. The activated carbon granules were filtered out using a coarse steel mesh filter and were rinsed with

100 mL deionized water. After sitting for a few minutes, films were observed forming in the bottom of the filtrate flasks with all three concentrations. The precipitate from the 8 mM sample was collected and air-dried for wide angle X-Ray diffraction (WAXD) analysis. The nanosheet-coated activated carbon granules were placed in an oven to dry at 80 °C for 1 hour.

All of the activated carbon samples were pyrolyzed in a tube furnace in the same manner as those in the “dip and dry method”. For all three samples, the oven temperature was held at 450 °C for 2 hours. The samples were immediately placed in a dessicator for storage after removal from the furnace.

2.1.4 The “Dip and Dry Method” - pH Modification

This method is similar to the first “dip and dry” method, but a pH modification step was introduced to release the nickel(II) from the surface of the activated carbon. In the first step, 1 g of activated carbon was added to 200 mL of 0.5 mM nickel(II) sulfate solution while stirring. The pH before and after adding the carbon was 4.73 and 7.79, respectively. The solution was placed under vacuum for 20 minutes. The carbon was then removed from the solution and placed in a mesh steel basket to dry for 1 hour at 80 °C.

After removal from the oven, the activated carbon was added to 200 mL of 1 mM potassium tetracyanoplatinate(II) solution while stirring. The pH before and after adding the carbon was 5.59 and 7.58, respectively. The solution was placed under vacuum for 20 minutes. The pH was 8.31 after release from vacuum. In order to release the nickel(II) from the carbon surface in the presence of the tetracyanoplatinate (II) ion, the pH was adjusted to 3. The solution was stirred for 24 hours and kept at pH 3. The carbon was removed from the solution and dried in a mesh steel basket for 1 hour at 80 °C.

The nanosheet-coated activated carbon was placed in a tube furnace under the same conditions as the previous two methods. The furnace was held at 450 °C for two hours. The sample was immediately placed in a dessicator upon removal from the furnace.

2.1.5 Standard Platinum Catalyst Preparation

A platinum catalyst was prepared via the impregnation and subsequent reduction of chloroplatinic acid on carbon. Chloroplatinic acid ($\text{H}_2\text{PtCl}_6 \cdot (\text{H}_2\text{O})_6$) was prepared by dissolving elemental platinum in hot aqua regia. To eliminate unwanted byproducts after dissolving the platinum, hydrochloric acid was added to the solution until production of gases ceased. The liquid was removed under vacuum at room temperature, producing an orange powder.

The catalyst was prepared according to common impregnation preparation methods for carbon-supported platinum.^{88,89,90} A mass of 0.0156 g of chloroplatinic acid was added to 1 mL of deionized water to produce a yellow solution. The same carbon substrate (Aqua Solutions, 8-12 mesh, coconut-derived) that was used for the Pt/Ni catalysts was used for the standard catalyst. A mass of 0.5000 g carbon was added to the solution, and the solution immediately became clear upon absorption of the chloroplatinic acid. The solution was placed under vacuum for 20 minutes. After releasing vacuum, the carbon granules were filtered and dried at 80 °C for one hour. The filtrate was gently heated to evaporate the liquid. No solid component remained from the filtrate. This indicated that all of the chloroplatinic acid was adsorbed by the carbon. To reduce the chloroplatinic acid, the carbon was heated in a hydrogen atmosphere at 350 °C for two hours after purging with argon.

2.2 Scanning Electron Microscopy and Energy-Dispersive X-Ray Spectroscopy

Samples from before and after pyrolysis were examined by scanning electron microscopy (SEM) using a Helios NanoLab 400 dual beam system from FEI Company. SEM equipment was acquired through the support of the National Science Foundation (Award #0923509). Samples were examined by mounting the granules to carbon tape on the SEM sample mounts. Several random granules from each sample were examined to determine if coatings were uniformly deposited on all granules. Secondary electron images and energy dispersive X-ray spectroscopy data (EDS) were taken at a current of 86 pA and a voltage of 5 kV. EDS data were analyzed using TeamEDS software.

2.3 X-Ray Photoelectron Spectroscopy

X-ray photoelectron spectroscopy (XPS) was carried out using a VG Scienta 2002 hemispherical analyzer with a dual anode Al($\kappa\alpha$) and Mg($\kappa\alpha$) source. Peak fitting and deconvolution were performed using FitXPS Version 2.12 by David L. Adams. Spectrum shift was corrected by using the graphitic carbon peak with a binding energy of 284.6 eV, which was the highest intensity carbon signal in all samples.

2.4 Catalysis Testing Method – Hydrogenation of Styrene to Ethylbenzene

To test the catalytic activity of the Ni/Pt catalysts, the hydrogenation of styrene to ethylbenzene was used. A 10 vol. % styrene (Acros Organics, 99% extra pure) in cyclohexane (Sigma-Aldrich, CHROMASOLV® Plus, 99.9%) solution was prepared for the reaction. For higher activity catalysts, initial concentrations of 13.33% and 15% were used to keep the measured data in the same concentration range. The solution was added to a Teflon® sleeve. For each run with the Ni/Pt catalyst on activated carbon, 0.1500 g of catalyst was added to the solution before sealing in a steel container in a Parr 4524 Stirred

Pressure Vessel. The vessel was purged by charging with ultra-high purity hydrogen to 200 psi for 5 minutes, and then releasing pressure slowly over the course of 10 minutes. This was carried out for a total of three times to complete the purge. After purging, the vessel was charged to 800 psi with ultra-high purity hydrogen, and the heating program was started. The solution was stirred at 600 rpm. The vessel was ramped to 80 °C over a period of 30 minutes using a Watlow Series 981 temperature controller in a Parr 4843 controller unit. The vessel was then allowed to stay at 80 °C for one hour before the first sample was withdrawn. A total of five 10 mL aliquots were withdrawn at one hour intervals using a Parr 4351 Sample Collection Vessel Assembly. The intervals were reduced to 30 minutes for the 2 mM and 4 mM “precipitation method” samples and the “pH-modified dip and dry method” sample. The interval was reduced to 15 minutes for the 8 mM “precipitation method” sample. After each withdrawal, 20 psi of pressure was released and then added to clear the withdrawal tube. The sample collection vessel was removed and dried with compressed air between each withdrawal. After withdrawing an aliquot, it was immediately diluted for gas chromatography–mass spectrometry (GC-MS) and GC flame ionization detector (FID) analysis.

2.5 GC-MS and FID Analysis

Catalysis products were analyzed via GC-MS and FID. An Agilent Technologies 5973 Network Mass Selective Detector, 6890N Network GC System, 59864B Ionization Gauge Controller, and GC/MSD ChemStation Software were utilized in the analysis. The internal standard method was used for quantitative analysis. The internal standard used was n-decane (Alfa Aesar, 99%), and the solvent used was cyclohexane (Sigma-Aldrich, CHROMASOLV® Plus, 99.9%). A series of standard solutions was prepared with

known concentrations of styrene and n-decane. The n-decane concentration used for the internal standard solution was 0.5 mM, and the styrene concentrations were 0.06 mM, 0.11 mM, 0.23 mM, 0.45 mM, and 0.90 mM. All quantitative measurements were carried out using the GC FID detector. Internal standard calibration was re-run for each set of measurements to alleviate the effect of instrumental drift. The integration results and internal standard calibration plot for each calibration are listed in Appendix I.

Samples were prepared for GC by using a micropipette to add 11.49 μ L of reaction solution to a 10 mL volumetric flask and diluting with 0.5 mM n-decane. A 0.5 μ L amount was injected into the instrument for GC FID runs, and a 0.2 μ L amount was injected for GC-MS runs. The results of all FID runs were analyzed using the Agilent Technologies GC/MSD ChemStation software suite.

After each catalysis run, samples were analyzed via GC-MS to determine the composition of products. The compounds were identified by comparing results to those in the NIST 02 MS database using the Agilent Technologies GC/MSD ChemStation software suite. The retention times of the known peaks from GC-MS were compared to the retention times of peaks from FID runs to determine their compositions.

2.6 ICP-AES Analysis

Inductively coupled plasma atomic emission spectroscopy (ICP-AES) was used to determine the nickel content of the catalysts. Samples from the first “dip and dry method” were run by the Edwards Aquifer Research & Data Center using a Spectro Genesis ICP-AES and EPA Method 200.7 modified for solid samples.

The samples from the other two methods were analyzed courtesy of Analysys, Inc. The reporting quantification limits (RQL), blank signals, and method used are shown

in Table 2. Quality assurance data, including precision, analyte recovery percentages, calibration verification (CCV) percentages, and laboratory control sample (LCS) percentages provided by Analysys, Inc. are shown in Table 3.

Table 2. ICP-AES analysis method data from Anlaysys, Inc.

Sample	Parameter	Units	RQL	Blank	Method
	Metals Dig.- Total	---	---	---	3050B
Dip and Dry- pH Mod.	Nickel/ICP	mg/Kg	123	<123	6010C & 200.7
Precip.-2mM	Nickel/ICP	mg/Kg	119	<119	6010C & 200.7
Precip.-4mM	Nickel/ICP	mg/Kg	526	<526	6010C & 200.7
Precip.-8mM	Nickel/ICP	mg/Kg	476	<476	6010C & 200.7

Table 3. Quality assurance data from Analysys, Inc.

Prec.	Recov.	CCV	LCS
1.49	97.76	101.38	98.48

2.7 Wide Angle X-Ray Diffraction

All wide angle X-ray diffraction measurements were carried out using a Bruker D8 Focus diffractometer using a Cu K α radiation source. The air-dried powder precipitate from the 8 mM “precipitation method” was used for powder XRD.

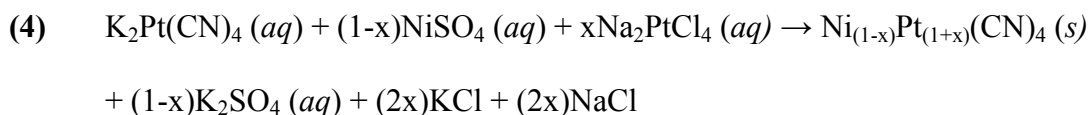
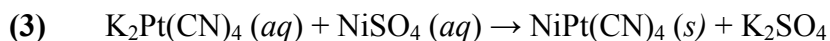
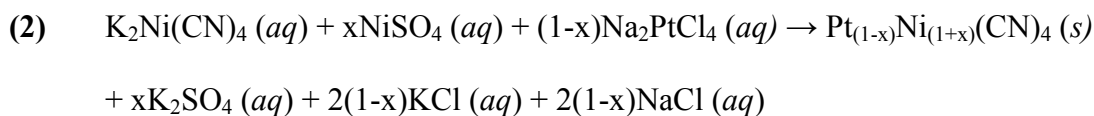
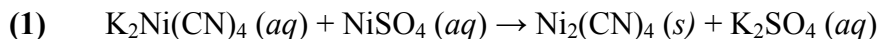
CHAPTER 3

Results and Discussion

3.1 Preparation and Reduction of Nanosheets on Activated Carbon Substrate

Activated carbon derived from coconut shell was chosen as the support for the catalyst material due its high porosity and associated surface area. The activated carbon also plays an active role in the adherence of precursor material due to the high number and diverse functionality of its polar surface groups.⁹¹ The initial concentrations for the precursor solution were established based on previous experiments which focused on synthesizing monolayers of $\text{MNi}(\text{CN})_4 \cdot 6\text{H}_2\text{O}$ at an aqueous-organic liquid-liquid interface. Initial catalyst precursor concentrations were similar to the concentrations at which mono- or few-layer sheets formed in the liquid-liquid interface synthesis. Liquid-liquid interface work is underway and will be reported elsewhere.

The proposed reaction equations for the formation of nanosheets on the surface of the activated carbon are as follows:



Equation (1) is the reaction for a monometallic Ni precursor, $\text{Ni}_2(\text{CN})_4$. Equation (2) is the reaction for a bimetallic precursor, $\text{Pt}_{(1-x)}\text{Ni}_{(1+x)}(\text{CN})_4$, consisting of 0-50% Pt and using $\text{K}_2\text{Ni}(\text{CN})_4$ as a reactant. Replacing $\text{K}_2\text{Ni}(\text{CN})_4$ with $\text{K}_2\text{Pt}(\text{CN})_4$ yields the reactions

in Equation (3) and (4) to produce a bimetallic precursor, $\text{Ni}_{(1-x)}\text{Pt}_{(1+x)}(\text{CN})_4$, with 50-100% Pt content.

The untreated activated carbon was analyzed via SEM for comparison to the treated carbon. SEM images from the untreated activated carbon are shown in Figures 4A and 4B. The images reveal a low contrast bulk surface with significant amount smaller pieces of carbon adhered to the surface.

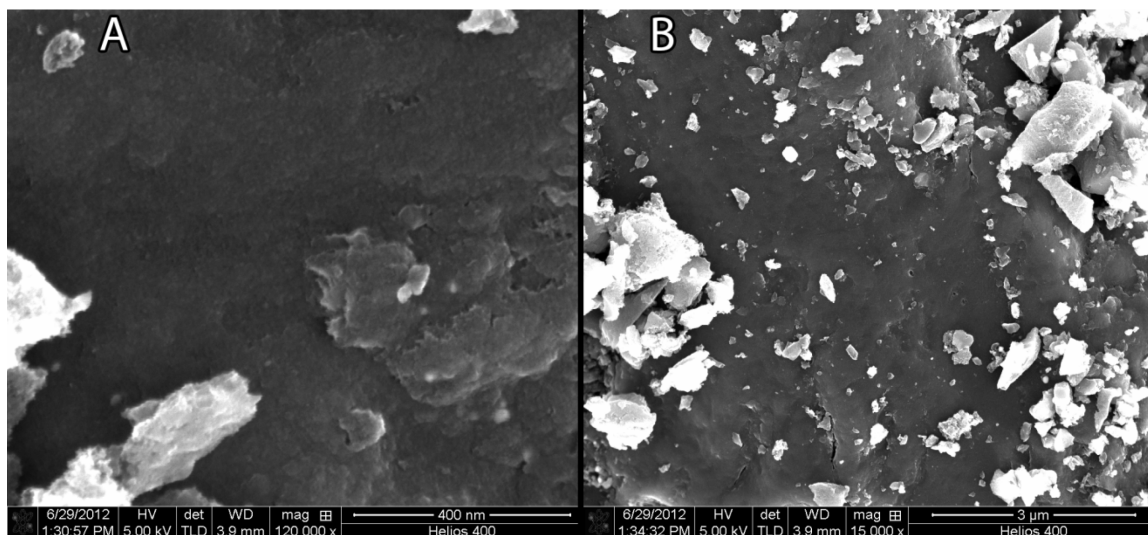


Figure 4. Untreated activated carbon. SEM images of untreated activated carbon are shown at (A) 120,000x and (B) 15,000x magnification.

3.1.1 The “Dip and Dry Method” – no pH Modification

Initially, focus was directed toward obtaining a layer of nanosheets with a simple 2-step submersion and drying process. No pH modification was carried out in these experiments. The pH modification proved to be a necessary step in the formation of nanosheets as found in the two other methods explored. The water-soluble platinum(II) salt $\text{Na}_2\text{PtCl}_4 \cdot 3\text{H}_2\text{O}$ was used to introduce platinum(II) ions via the second immersion step of the process. The reactant concentrations and Pt-Ni ratios of reactants corresponding to the names used here can be found in Table 1.

The SEM images of the “1 (1:20 Pt:Ni)”, “1/8th (1:20 Pt:Ni)”, and “1/8th (2:3 Pt:Ni)” samples are shown before and after pyrolysis in Figures 5, 6, and 7, respectively. The surface of all three samples had an evenly distributed mottled appearance from a coating on the carbon surface. After pyrolysis, the “1/8th (1:20 Pt:Ni)” and “1/8th (2:3 Pt:Ni)” sample surfaces were covered in spheres that were around 3-10 nm in diameter. Due to the higher concentration of reactants, the “1 (1:20 Pt:Ni)” sample had a larger distribution of spherical features, generally in the range of 3-100 nm in diameter.

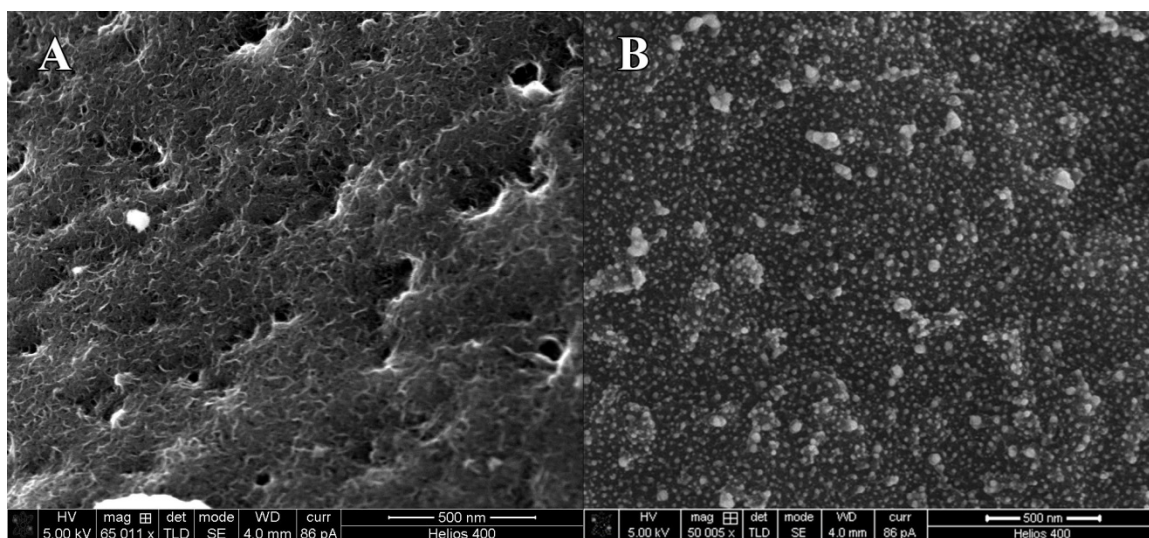


Figure 5. SEM images of the “1 (1:20 Pt:Ni)” sample (A) before and (B) after pyrolysis.

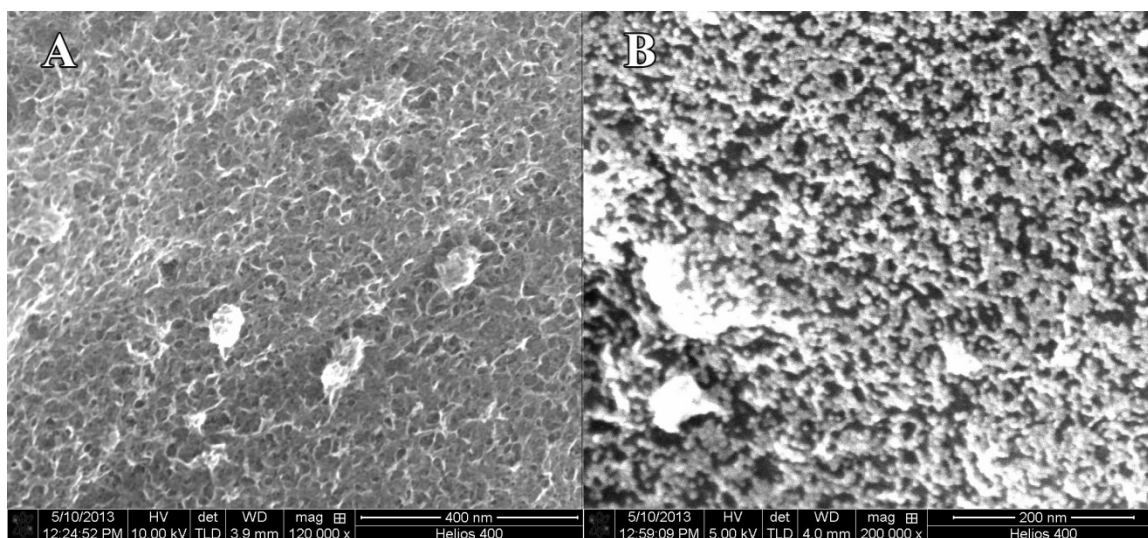


Figure 6. SEM images of the “1/8th (1:20 Pt:Ni)” sample (A) before and (B) after pyrolysis.

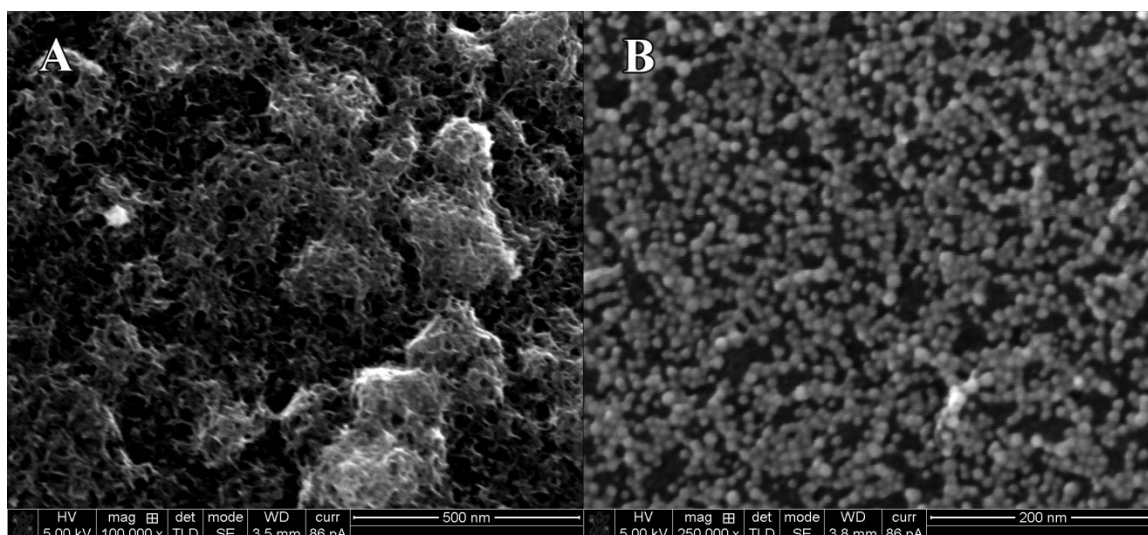


Figure 7. SEM images of the “1/8th (2:3 Pt:Ni)” sample (A) before and (B) after pyrolysis.

A sample was prepared without using potassium tetracyanonickelate(II) to compare with the previous three samples. Without potassium tetracyanonickelate(II), the formation of nanosheets would not be possible, and the samples could be evaluated for formation of nanosheets against this material, labeled “salts only”. The concentration of nickel(II) sulfate was doubled to keep the Pt:Ni ratio at 1:20. The surface of the “salts

only” sample is shown before and after pyrolysis in Figure 8. The majority of the surface before pyrolysis appeared similar to the previous three samples. The only difference was the occurrence of clusters of reactant on the surface, attributed to the higher concentration of nickel(II) sulfate. This similarity indicated that $\text{Pt}_{(1-x)}\text{Ni}_{(1+x)}(\text{CN})_4$ nanosheets had not formed on the surface of the carbon.

The EDS spectra for the “1 (1:20 Pt:Ni)” and “1/8th (2:3 Pt:Ni)” samples before pyrolysis, shown in Figures 9 and 10, confirmed that no nanosheets had formed. The absence of any nitrogen signal meant that the cyanide ligands could not be present, but the presence of nickel indicated that nickel(II) had been adsorbed by the activated carbon surface. If platinum was present, it was below the limit of detection for the instrument. Platinum was detected in the EDS spectrum for the “salts only” sample before pyrolysis, shown in Figure 11. Since activated carbon is known to also adsorb platinum(II), it is likely that platinum was also present in trace amounts in the other samples. After analysis of this series of samples, it was clear that no nanosheets were formed and modifications to the procedure were necessary.

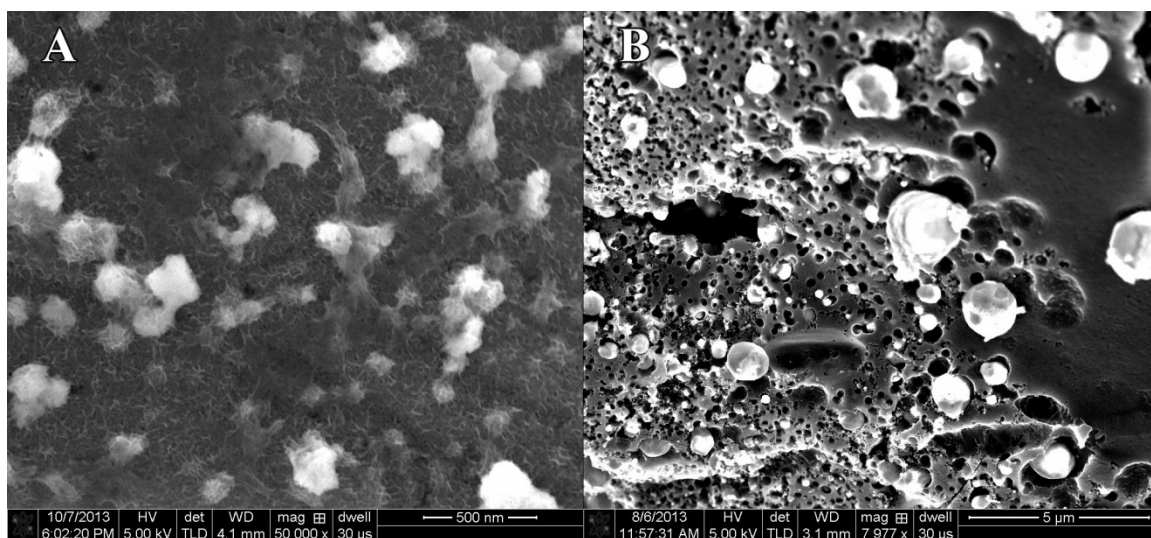


Figure 8. SEM images of the “salts only” sample (A) before and (B) after pyrolysis.

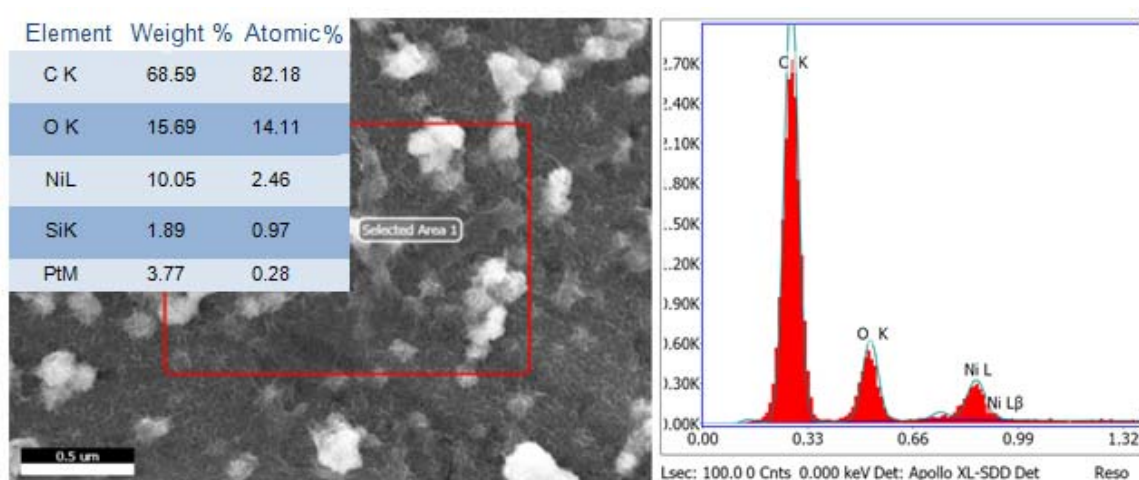


Figure 11. SEM image and EDS data from the “salts only” sample before pyrolysis.

3.1.2 Nickel(II) Desorption from Activated Carbon – pH Dependence

Upon examination of the results from the first “dip and dry method”, it was determined that the high affinity of the activated carbon surface for nickel(II) ions kept the reaction from proceeding to form nanosheets. Study by Kadirvelu, et al. has shown that coconut-derived activated carbon has the ability to adsorb significant amounts of nickel(II) from solution.⁹² At a carbon concentration of 400 mg/L and a nickel(II) concentration of 40 mg/L, the carbon was shown to adsorb 64.38 mg/g nickel(II) at an equilibrium time of 40 minutes, or 64.38% of nickel(II) in the solution. This is a nickel(II)/carbon mass ratio of 0.1. In our work, the step 2 solution in the “1 (1:20 Pt:Ni)” sample synthesis had a nickel(II)/carbon ratio of 0.2103. According to Kadirvelu, et al., at a carbon concentration of 400 mg/L and a nickel(II) concentration of 10 mg/L, the carbon was shown to adsorb 20.63 mg/g nickel(II) at an equilibrium time of 40 minutes, or 82.52% of nickel(II) in the solution. This sample had a nickel(II)/carbon mass ratio of 0.025. In our work, the “1/8th (1:20 Pt:Ni)” sample had a nickel(II)/carbon mass ratio of 0.0263 in step 2 of the synthesis. Based on this comparison, it is likely that a significant

amount of nickel(II) was adsorbed by the activated carbon before the formation of sheets could occur. Based on the absence of platinum in the EDS results from the “1/8th (2:3 Pt:Ni)” sample, nickel(II) adsorbed preferentially over platinum(II).

In the study by Kadirvelu, et al., the ability of activated carbon to adsorb nickel(II) was found to be strongly dependent on pH. The adsorption ability decreases rapidly with decreasing pH between pH 5 and pH 2. The primary reason for decrease in absorption is the ion exchange occurring on surface groups of the carbon. Initially, the nickel(II) is absorbed by the surface sites of the carbon, but, as pH is decreased, the reaction equilibrium is shifted toward protonation of the surface sites and release of the nickel(II) ions.

An experiment, presented in Section 2.1.2, was carried out to determine the pH-nickel(II) absorption relationship in our system. The primary goal of this experiment was to determine at what pH the carbon completely releases the nickel(II) from the surface, so that the catalyst precursor synthesis could be carried out under those conditions. This would allow the nickel(II) ions freedom to react with the tetracyanometallate ion and form nanosheets on the surface. A summary of the experimental results is shown in Table 4.

Table 4. Ni atomic percent and pH of carbon granules from Ni desorption experiment.

Granule #	1	2	3	4	5	6	7	8	9
pH	7.70	6.03	6.76	5.76	4.10	3.52	3.03	2.51	2.02
Atomic % Ni	0.82	1.00	0.61	0.64	0.39	0.12	0.00	0.00	0.00

The SEM images and EDS analyses for granules 1-4 are shown in Figures 12-15. These granules have the highest nickel content, ranging from 0.61 to 1.00 atomic percent. Nickel content variations in these samples can be explained by local variation in the

surface site concentration of the activated carbon. The mottled appearance of the surface stems directly from nickel(II) absorption on the surface. This appearance is very similar to the appearance of the carbon surface in the first “dip and dry method” trials. This similarity reinforces the conclusion that adsorbed nickel(II) dominated the surface of those samples, preventing the nanosheet material from forming on the surface.

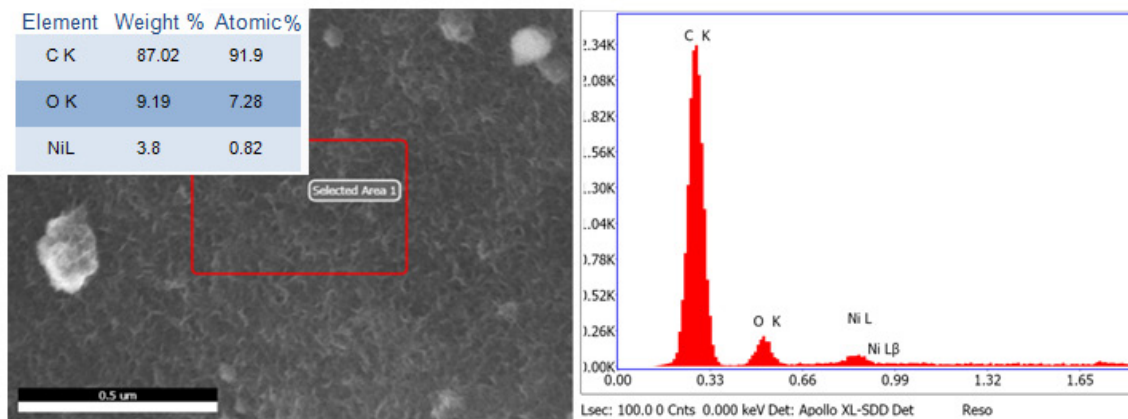


Figure 12. SEM image and EDS data from granule 1.

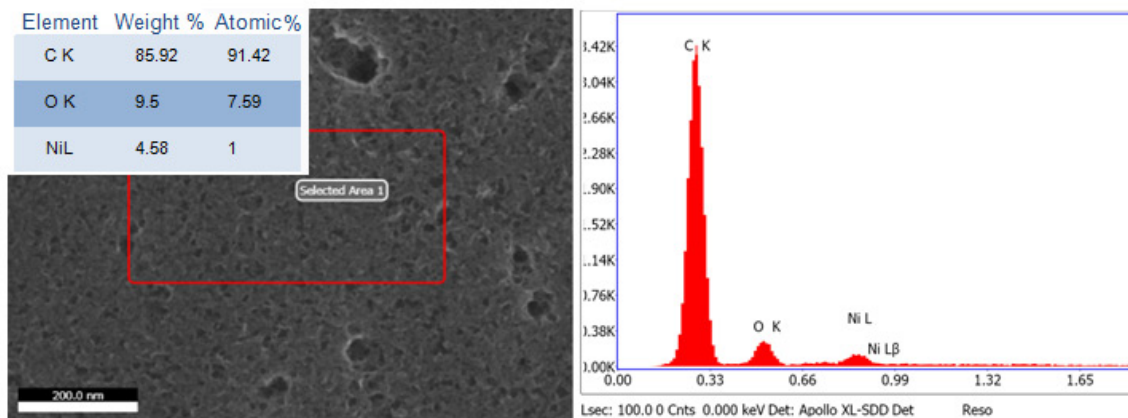


Figure 13. SEM image and EDS data from granule 2.

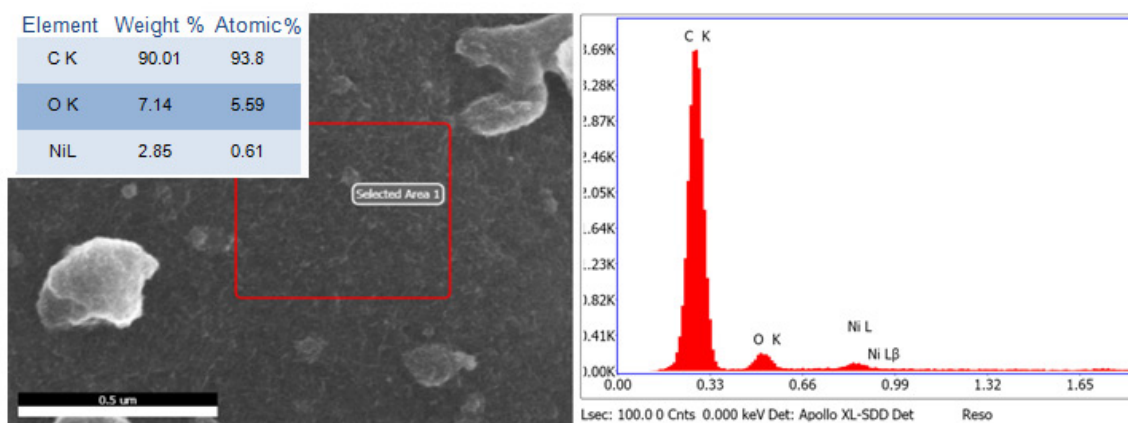


Figure 14. SEM image and EDS data from granule 3.

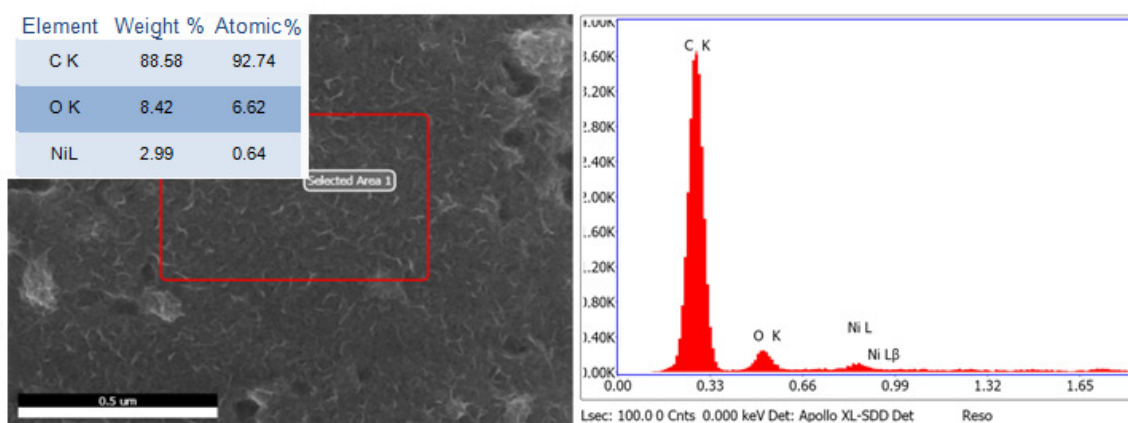


Figure 15. SEM image and EDS data from granule 4.

The SEM images and EDS data from granules 5-9 are shown in Figures 16-20. The nickel content begins to drop in granule 5, taken at pH 4.10, as the surface groups are protonated. The data published by Kadirvelu, et al., indicates that the nickel(II) absorption ability decreases rapidly below pH 5. Granule 6, taken at pH 3.52, is the last sample in which any detectable nickel was found. It is also the last sample in which the mottled pattern appears. Granules 7-9 have no detectable nickel content. Their surfaces are comparable to that of the virgin carbon shown in Figure 4. At a pH of 3.03, granule 7 is the first in the series with no detectable nickel. Based on this information, pH 3 is the ideal pH for the catalyst precursor synthesis. The synthesis should not be carried out a pH

lower than 3 to avoid the formation of hazardous decomposition products from cyanometallate compounds.

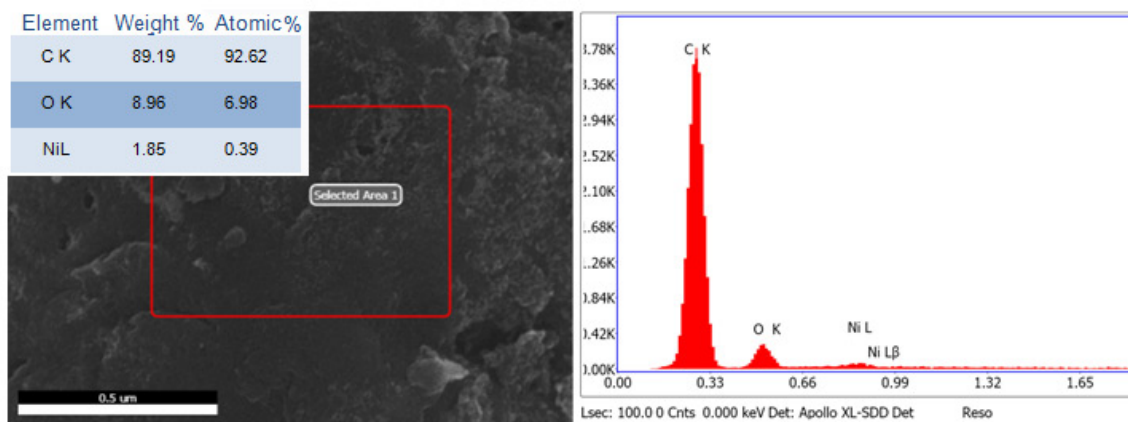


Figure 16. SEM image and EDS data from granule 5.

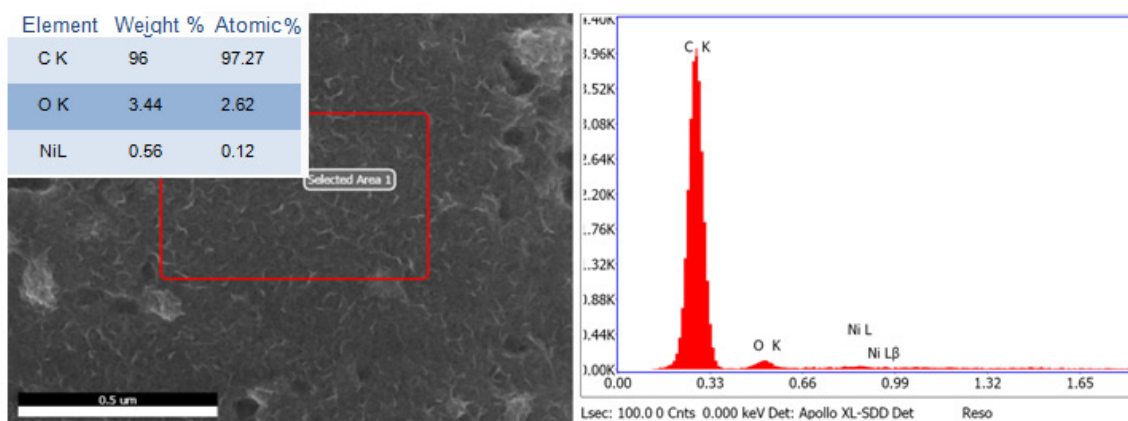


Figure 17. SEM image and EDS data from granule 6

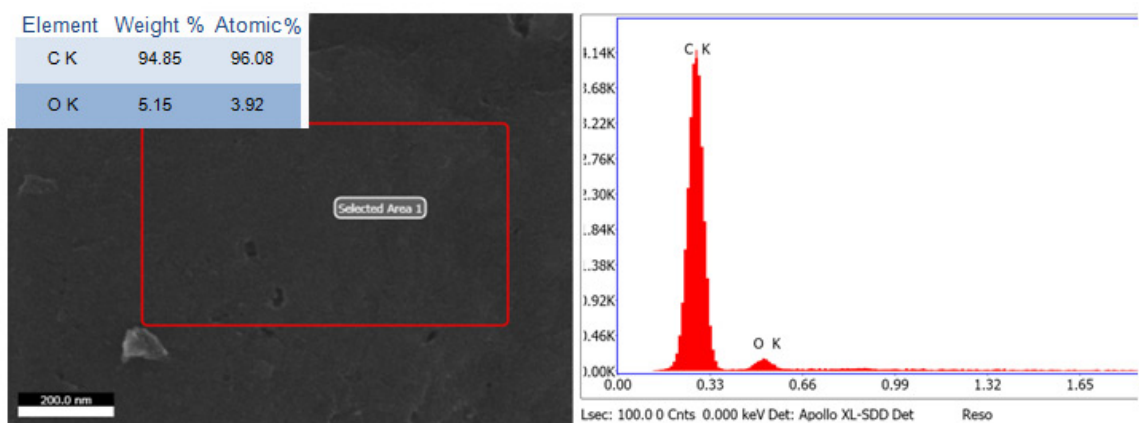


Figure 18. SEM image and EDS data from granule 7.

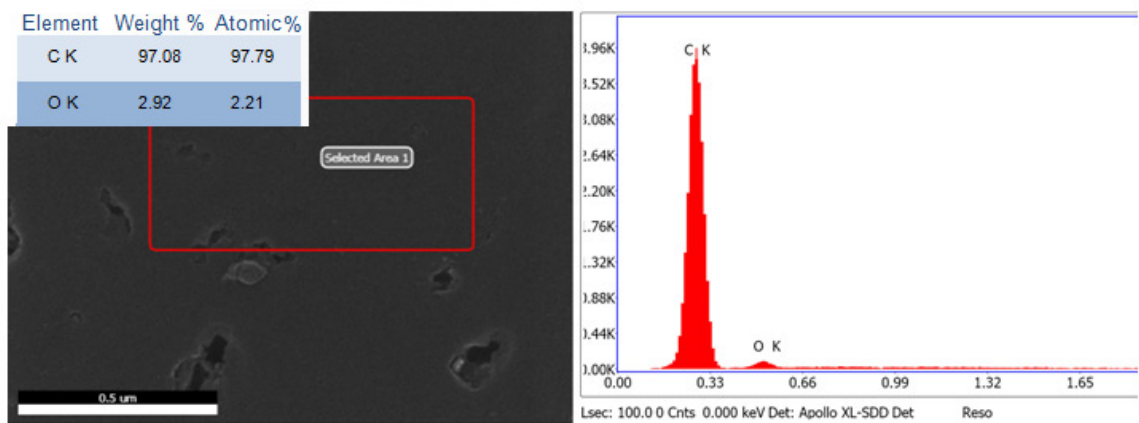


Figure 19. SEM image and EDS data from granule 8.

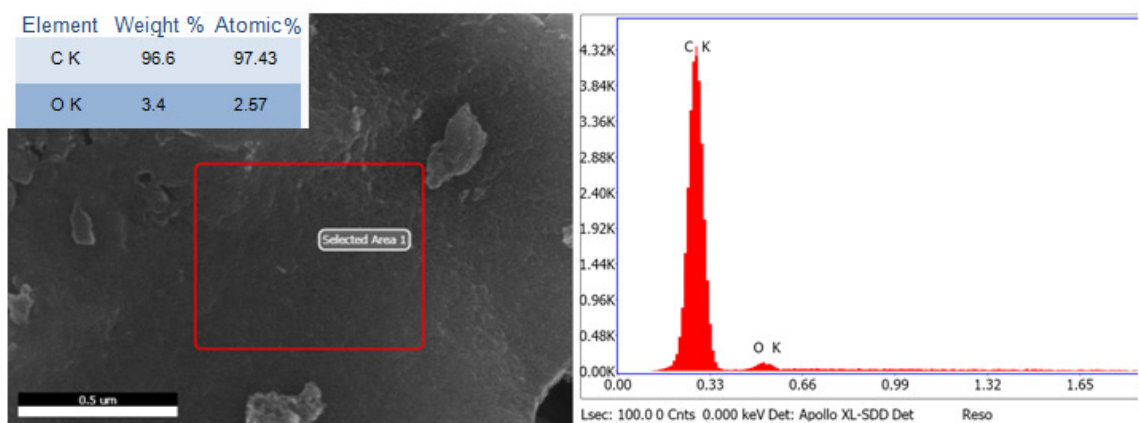


Figure 20. SEM image and EDS data from granule 9.

3.1.3 The “Precipitation Method” – pH Modification

3.1.3.1 SEM/EDS Analysis Before Pyrolysis

The “Precipitation Method” was developed based on the results from the previous pH-nickel(II) desorption experiment. The samples were analyzed for surface morphology and composition before and after pyrolysis via SEM and EDS. The eZAF Smart Quant Results are shown for EDS but should be considered semi-quantitative. Due to the nanoscale thickness of the surface features and the relatively large interaction area of the electron beam, the carbon from the support appears as the most intense peak in the EDS spectra of the carbon granules.

SEM images of 2 mM sample before pyrolysis is shown in Figure 21, and the EDS spectrum for the 2 mM sample before pyrolysis is shown in Figures 22. No distinguishable surface features can be seen, even though both platinum and nickel metals can be detected in the EDS spectrum. At this lower concentration, with the large number of nucleation sites on the carbon, it is likely that the nanostructures are very small in size in all dimensions, and, therefore, undetectable via SEM imaging. The nickel/platinum ratio was very close to a 1:1 ratio, and nitrogen was present in the spectrum. No nitrogen occurs in the EDS spectrum of the virgin carbon, so the nitrogen can only be attributed to the cyanide group in the precursor compound. This would be expected for the $\text{NiPt}(\text{CN})_4$ precursor compound. There are no signals corresponding to potassium or sulfur atoms, indicating that the K^+ and SO_4^{2-} ions left with the excess solution from the reaction. The presence of carbon, nitrogen, nickel, and platinum, combined with the absence of potassium and sulfur atoms, indicate the presence of $\text{PtNi}(\text{CN})_4$ nanosheets in the 2 mM sample.

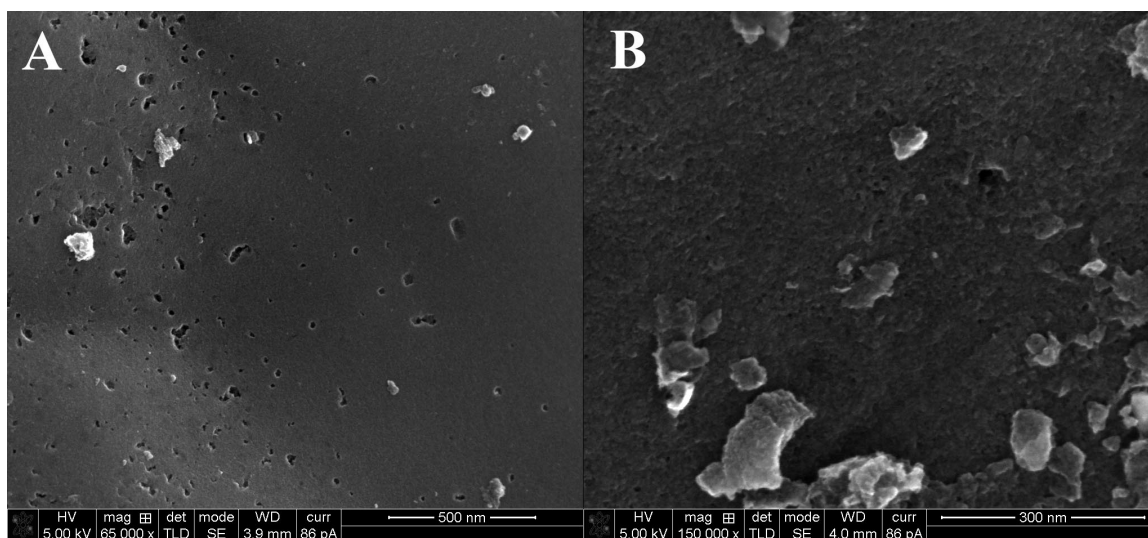


Figure 21. SEM images of the 2 mM “precipitation method” sample before pyrolysis. The surface is shown at (A) 65,000x and (B) 150,000x magnification.

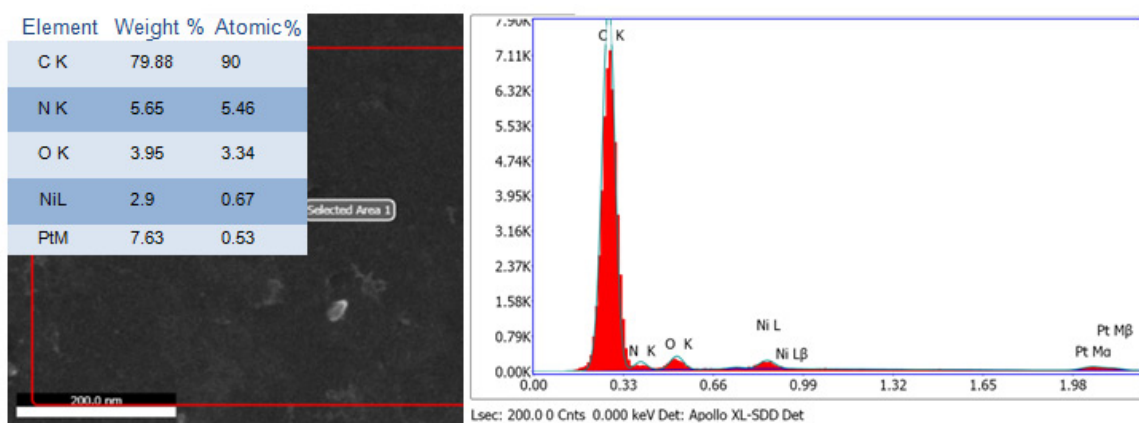


Figure 22. SEM image and EDS data from the 2 mM “precipitation method” sample before pyrolysis.

SEM images of the 4 mM and 8 mM samples before pyrolysis are shown in Figures 23 and 24, and the EDS spectra for the 4 mM and 8 mM samples before pyrolysis are shown in Figures 25 and 26, respectively. In the SEM images, nanosheets can be seen protruding from the surface of the activated carbon. These sheets are on the order of a few hundred nanometers in two dimensions and have sub-10 nm thickness. The sheet

formation began at a nucleation site on the activated carbon and extended outward once contact was made with another growing sheet. This explains why initial growth occurs parallel to the carbon surface but turns perpendicular to the surface in areas of higher concentration. Figure 23B shows where the edges of two sheets have met and began to rise from the surface. Although there were isolated areas of greater nanosheet concentration, the majority of the surface was coated evenly in the 4 mM sample. The 8 mM sample had an increase in isolated areas with more prolific growth. Figure 24A shows one such area.

The EDS spectra for both samples indicate the presence of the $\text{NiPt}(\text{CN})_4$ precursor. The platinum/nickel ratios are close to 1:1, with nitrogen present. No potassium or sulfur was detectable, indicating the absence of K^+ and SO_4^{-2} ions.

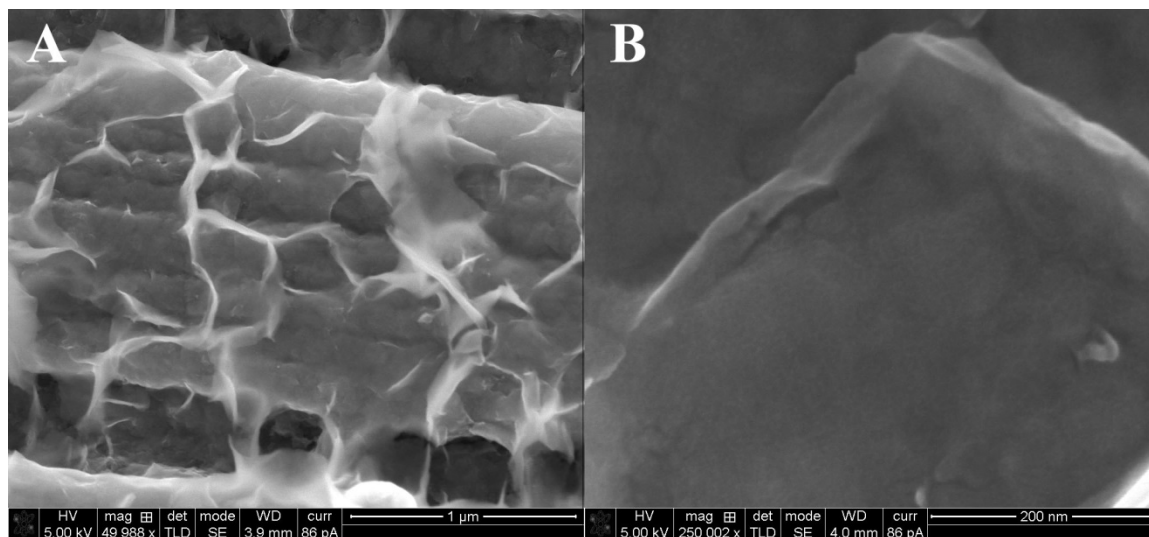


Figure 23. SEM images of the 4 mM “precipitation method” sample before pyrolysis. The surface is shown at (A) 49,998x and (B) 250,002x magnification.

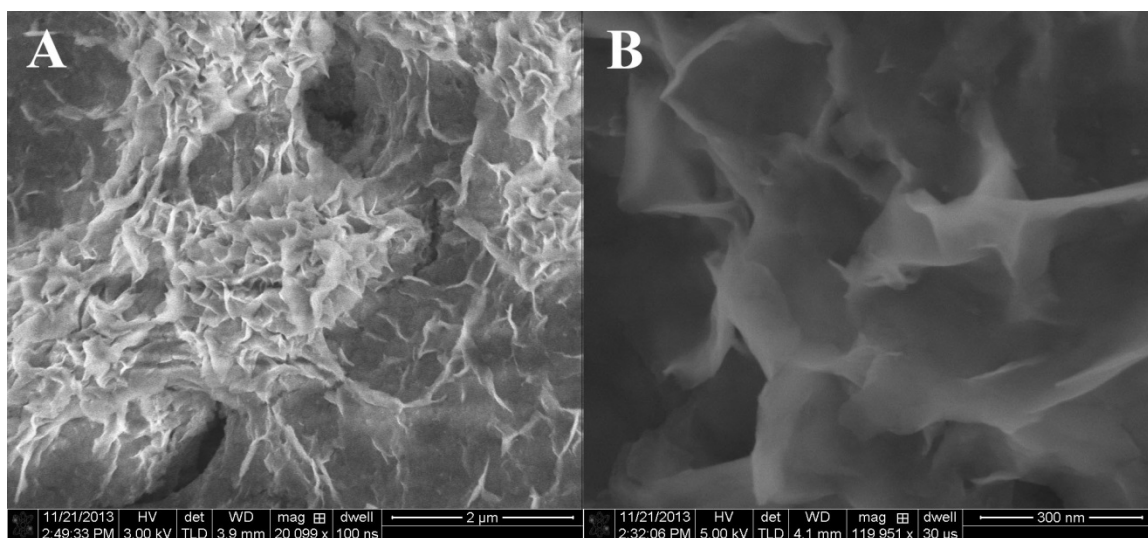


Figure 24. SEM images of the 8 mM “precipitation method” sample before pyrolysis. The surface is shown at (A) 20,099x and (B) 119,951x magnification.

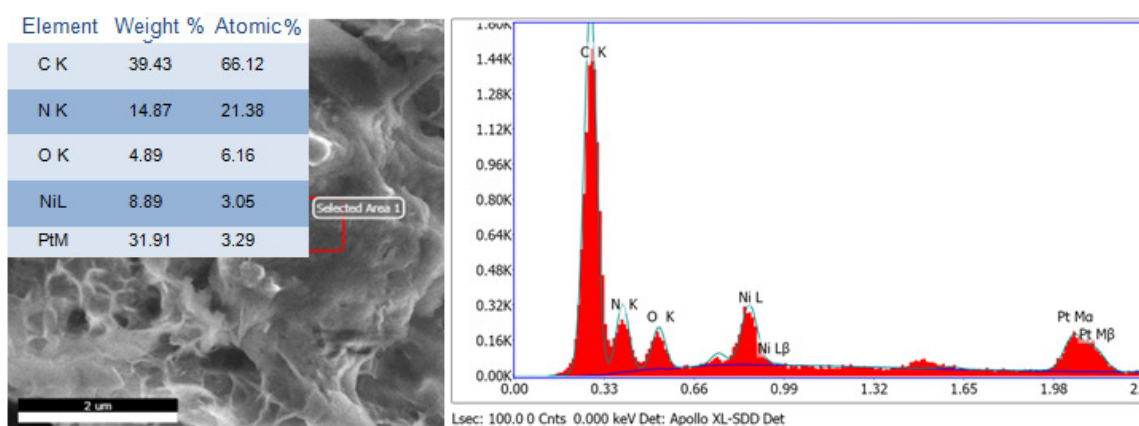


Figure 25. SEM image and EDS data from the 4 mM “precipitation method” sample before pyrolysis.

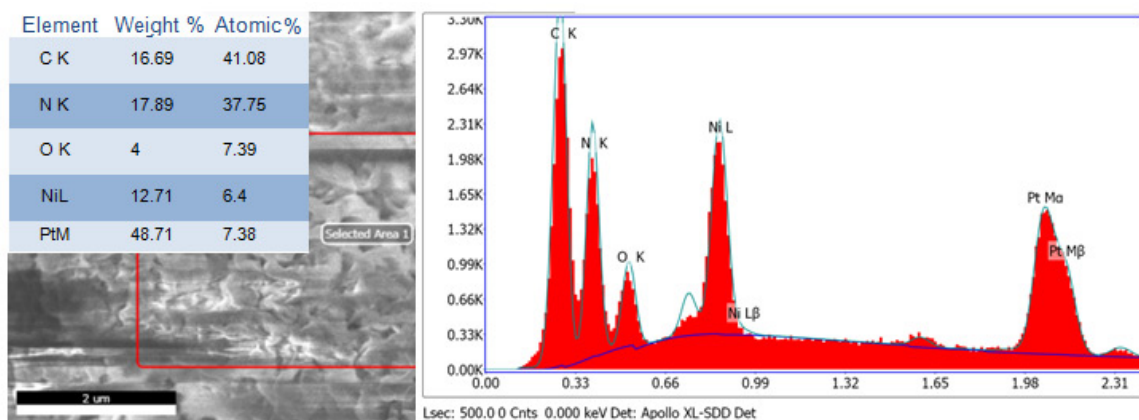


Figure 26. SEM image and EDS data from the 8 mM “precipitation method” sample before pyrolysis.

3.1.3.2 Thermogravimetric Analysis and Wide Angle X-Ray Diffraction of $\text{NiPt}(\text{CN})_4$

Thermogravimetric analysis (TGA) and wide angle X-Ray diffraction (WAXD) data were analyzed to determine structural and compositional data for the compound. The percent weight loss versus temperature plot is shown in Figure 27. The TGA data was obtained in air at a ramp of 20 °C/min to determine the degree of hydration of the compound. The loss ending at just over 160 °C corresponds to the loss of water in the structure. This indicates an initial formula of $\text{NiPt}(\text{CN})_4 \cdot 6\text{H}_2\text{O}$ and corresponds well with data from previous work on $\text{FeNi}(\text{CN})_4 \cdot 6\text{H}_2\text{O}$ multilayer cyanide-bridged metal compounds.⁸

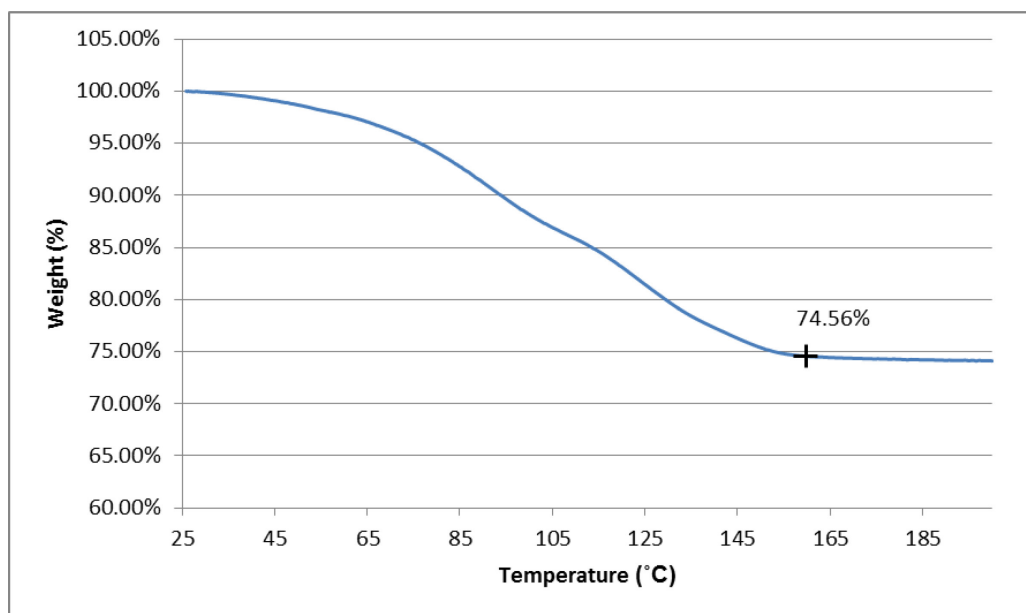


Figure 27. Weight percent versus temperature plot showing water loss in air.

The WAXD data was examined for any structural information that could be obtained. A single phase appeared to be present, and the pattern was analyzed using the CHEKCELL program. First, parameters similar to the known $\text{FeNi}(\text{CN})_4$ structure were chosen.⁸ The initial parameters used an orthorhombic crystal system and a Pnma space group. A fit could not be found for this space group, so it is likely that the $\text{NiPt}(\text{CN})_4 \cdot 6\text{H}_2\text{O}$ compound belongs to a different group. Using the lowest symmetry space group in the orthorhombic system, P222, tentative assignments were made to the unit cell parameters and the Miller indices. Of the unit cell, the c parameter has the most uncertainty. The unit cell parameters were $a = 14.4 \text{ \AA}$, $b = 10.2 \text{ \AA}$, and $c = 7.7 \text{ \AA}$. The experimental data and tentative peak assignments are shown in Figure 28. The 200 peak likely corresponds to the interlayer sheet distance and is the strongest assignment. The WAXD data coupled with the TGA data indicates a multilayer $\text{NiPt}(\text{CN})_4 \cdot 6\text{H}_2\text{O}$ structure for the bulk material, similar to $\text{FeNi}(\text{CN})_4 \cdot 6\text{H}_2\text{O}$ material explored previously.

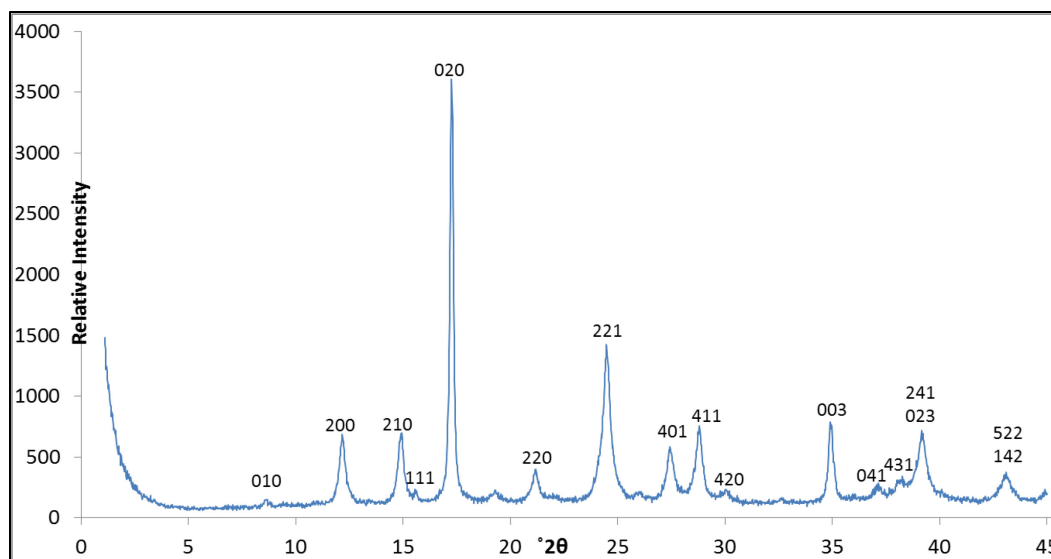


Figure 28. $\text{PtNi(CN)}_4 \cdot 6\text{H}_2\text{O}$ powder diffraction pattern with tentative peak assignments.

3.1.3.3 SEM/EDS Analysis After Pyrolysis

Figures 29 and 30 show the surface of the 2 mM and 4 mM catalysts after pyrolysis, respectively. The image of the 2 mM surface reveals evenly distributed spherical particles with a diameter range of 3-5 nm. A representative sample of particle measurements is shown in Figure 29B. The increase in precursor concentration in the 4 mM sample led to a much broader distribution of particles. The particles ranged from 3 nm spherical particles to around 100 nm semi-spherical particles. The larger particles formation was the result of higher nanosheet concentration where sheets meet at the edges. A correlation can be made when comparing the distribution and regularity of sheet edge collision and outward growth in the image before pyrolysis to the occurrence of larger particles in the image after pyrolysis.

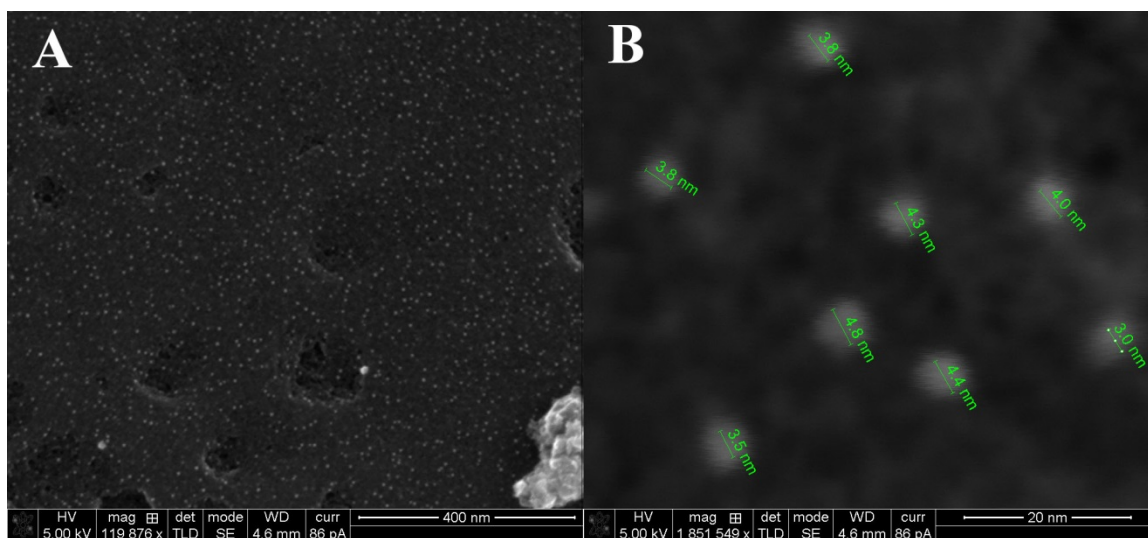


Figure 29. SEM images of the 2 mM “precipitation method” sample after pyrolysis. The surface is shown at (A) 119,878x and (B) 1,851,549x magnification.

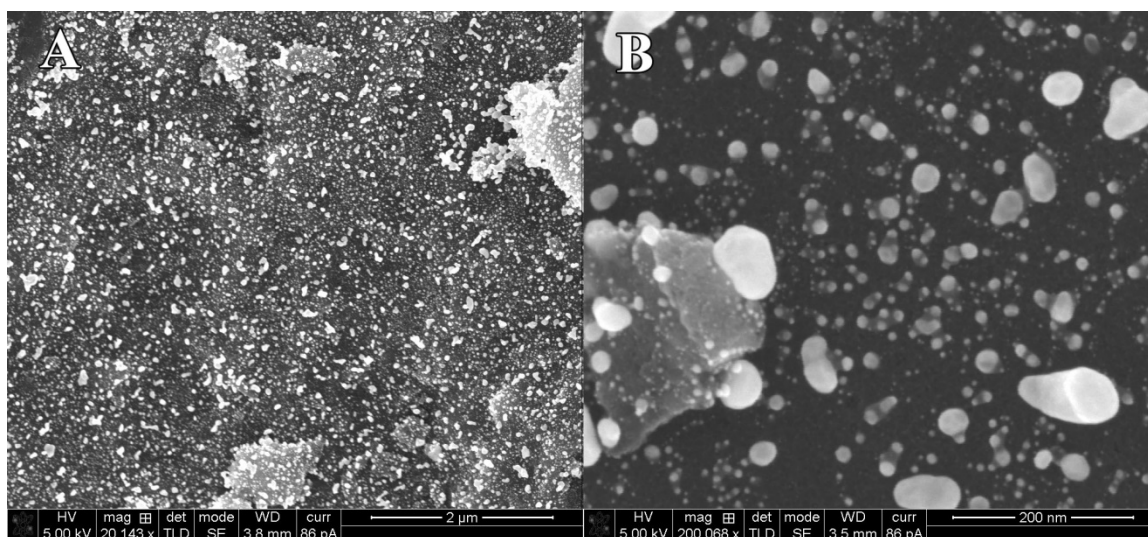


Figure 30. SEM images of the 4 mM “precipitation method” sample after pyrolysis. The surface is shown at (A) 20,143x and (B) 200,088x magnification.

The 8 mM catalyst, with a much higher concentration of metals, developed a more complex surface structure. SEM images of the two different types of areas found on the 8 mM sample surface are shown in Figures 31 and 32. In Figure 31B, the surface resembles the 4 mM sample surface, but the larger particles have started to fuse together. A different type of structure is seen in Figure 32B. A sponge-like metal structure extends

from the surface, with bridging structures on the order of 100 nm in width. These structures are derived from the higher concentration areas of precursor in which prolific sheet growth extends from the surface in the carbon, as seen in Figure 24A. Based on the particle size and even distribution on the surface, the 2 mM catalyst was expected to have the best activity of the series on a platinum mass basis.

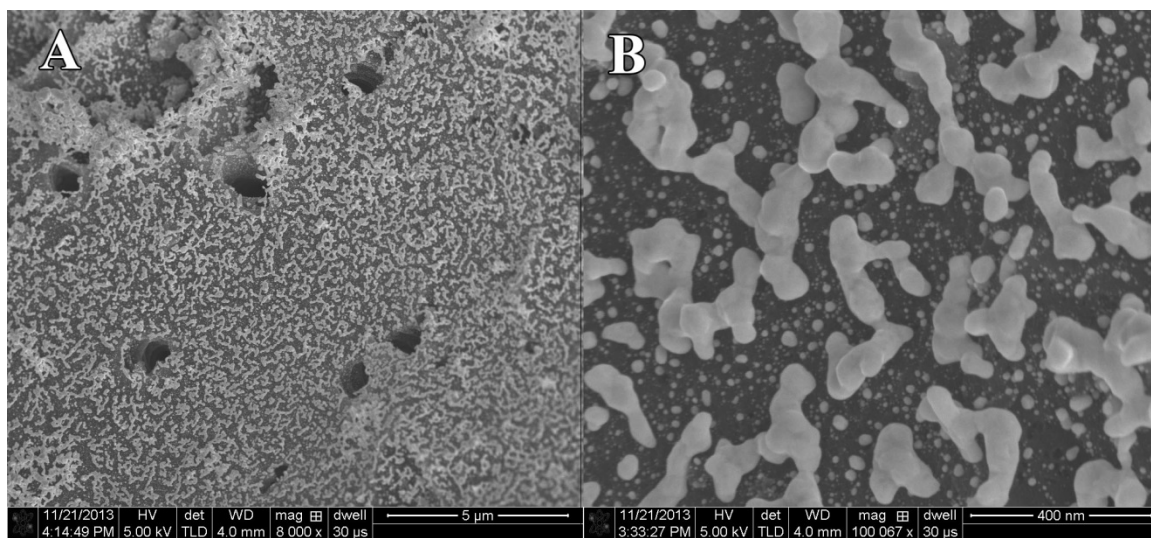


Figure 31. SEM images of the 8 mM “precipitation method” sample after pyrolysis. The surface is shown at (A) 8,000x and (B) 100,067x magnification.

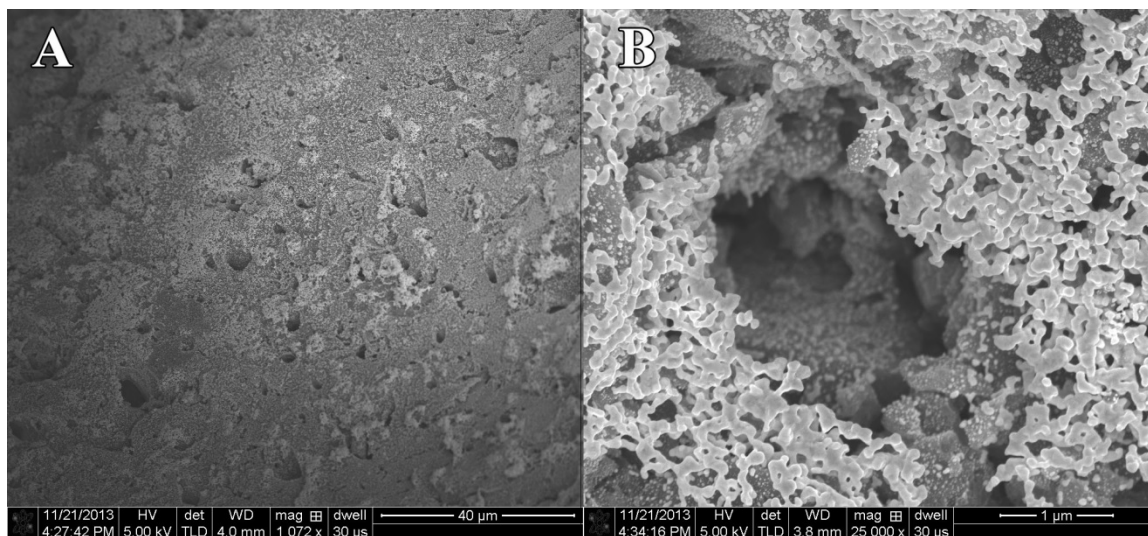
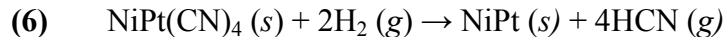
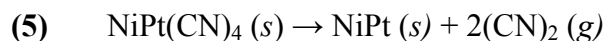


Figure 32. SEM images of the 2 mM “precipitation method” sample after pyrolysis. The surface of an area of higher Pt/Ni concentration is shown at (A) 1,072x and (B) 25,000x magnification.

The EDS data is shown for the 2 mM and 4 mM samples in Figures 33 and 34. Both samples have nickel and platinum present in the spectrum and are close to a 1:1 ratio. The loss of the cyanide ligand during pyrolysis is apparent from the absence of nitrogen in the spectrum. This result differs from the carbon nitride core Pt-Ni shell catalyst obtained by Di Noto, et al., in which a similar cyanide-bridged Pt-Ni precursor was used.⁸² In a related study by Kumar, et al., cyanide-bridged nickel(II) on carbon formed metallic nickel when heated at 700 °C in an argon atmosphere.⁹³ This was attributed to the loss of the cyanide ligands through cyanogen formation. Bocarsly, et al. reported the formation of various bimetallic alloys from cyanide-bridged metal cyanogel precursors through the loss of the cyanide ligand in the form of cyanogen and, to a lesser extent, hydrogen cyanide.^{94,95} The work by Kumar, et al. and Bocarsly, et al. was carried out under argon atmosphere. The work in this manuscript was carried out with a small percentage of hydrogen present. Although the $\text{PtNi}(\text{CN})_4$ compound is not a cyanogel, the cyanide-bridged metal structure is similar. The two proposed reduction pathways are:



Since the reduction is carried out with hydrogen, the primary pathway is likely that of eq. (6).

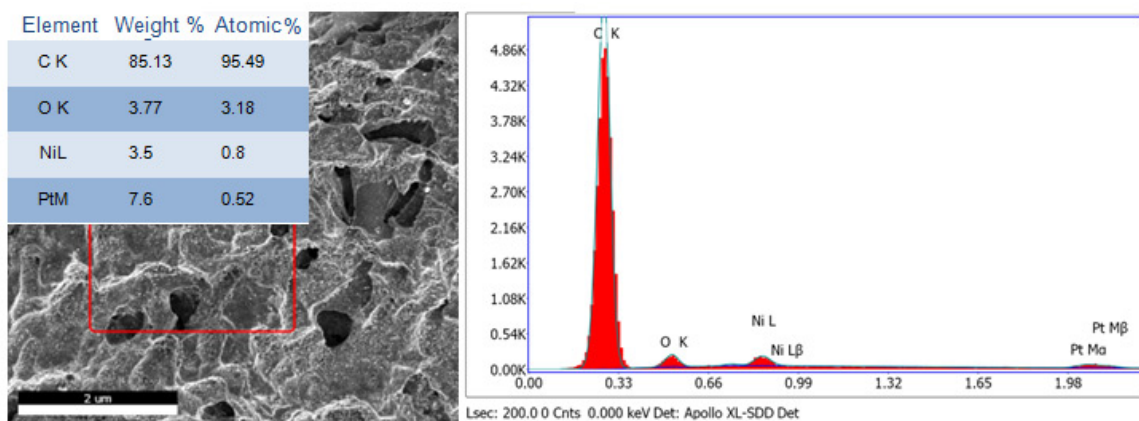


Figure 33. SEM image and EDS data from the 2 mM “precipitation method” sample after pyrolysis.

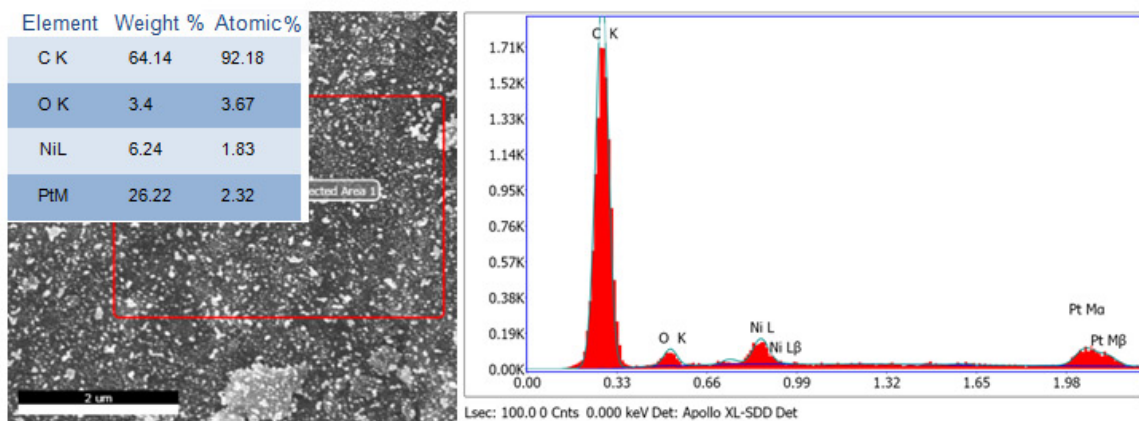


Figure 34. SEM image and EDS data from the 4 mM “precipitation method” sample after pyrolysis.

The EDS data for the 8 mM sample, shown in Figure 35, provides insight on the arrangement of nickel and platinum in this series of catalysts. The post-pyrolysis data shows significantly higher percentages of platinum than the pre-pyrolysis data. This is due to the interaction area of the electron beam rather than the actual loss of nickel,

which would not occur at the pyrolysis temperature. At 5 kV, the interaction area of the electron beam is small enough that the nickel signal would be significantly diminished if it were in higher concentration at the core of the structure. This theory was reinforced by Monte Carlo simulations of the electron beam interaction with a surface model in which the nickel is in the core and the platinum at the surface.

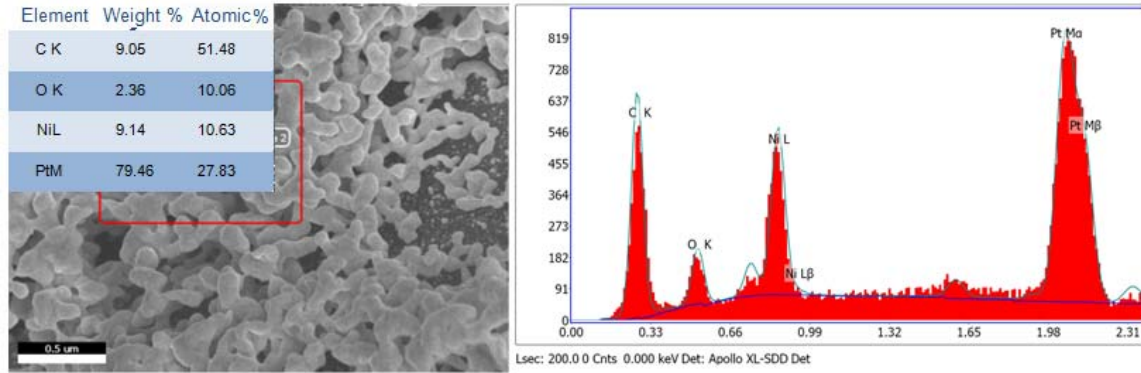


Figure 35. SEM image and EDS data from the 8 mM “precipitation method” sample after pyrolysis.

A cylinder with a diameter of 100 nm was used to approximate the shape of the features on the surface of the 8 mM sample. Based on a platinum density of 21.45 g/cm^3 and a nickel density of 8.908 g/cm^3 , the molar densities of platinum and nickel are 0.1115 mol/cm^3 and 0.1518 mol/cm^3 , respectively. Therefore, in any given volume with a 1:1 Pt:Ni ratio and completely segregated platinum and nickel phases, 57.63% of the volume is platinum and 42.37% of the volume is nickel. For our system, this is an approximation because the platinum and nickel phases are likely not completely segregated. A cylinder of 100 nm length and 100 nm diameter has a volume of $785,400 \text{ nm}^3$. Based on 42.37 vol. % nickel, the total volume of the inner nickel core would be $332,800 \text{ nm}^3$. The diameter of this inner nickel core is 65.08 nm, leaving a platinum shell thickness of 17.46 nm.

Monte Carlo simulations of electron trajectory were carried out using the Casino 2.48 software package. A total of 100,000 electron trajectories were carried out at a 5 kV accelerating voltage and a 10 nm beam radius. The simulation model consisted, from top to bottom, of a 17.46 nm platinum layer, a 65.08 nm nickel layer, and another 17.46 nm platinum layer on top of a carbon substrate. This horizontal sequence approximated the center of the model cylinder. The results of the simulation, including the trajectories of the last 200 electrons and depth versus intensity plots for X-rays of each element are given in Appendix II. Figures A2-3, A2-4, and A2-5 show the depth versus intensity plots for X-ray intensity at the detector. The platinum plot in figure A2-3 shows no significant decrease of the platinum X-ray signal across the 17.46 nm surface. The nickel X-ray intensity, shown in Figure A2-4, shows a rapid decline as the electrons travel deeper into the surface. This “sandwich” horizontal layer model predicts the nickel response at its level of highest intensity when compared to the more realistic cylinder model. In the cylinder model, the platinum signal would be even higher since the effective platinum depth increases toward the edges of the cylinder. If slicing in a straight line on either edge of the cylinder, the last 17.46 nm on either edge would yield cross-section composed entirely of platinum. Thus, the interaction area of the electron beam reinforces the theory of nickel core segregation.

3.1.3.4 XPS Analysis

XPS analysis was performed on the 8 mM concentration sample before and after pyrolysis. The platinum 4f_{7/2} signal was used to determine the valence state and chemical environment of the platinum atoms. The platinum XPS data before pyrolysis is shown in Figure 36. The platinum 4f_{7/2} peak at 73.70 eV correlates well with a previously

published value for a tetracyanoplatinate(II) structure, reported as 73.8 eV.⁹⁶

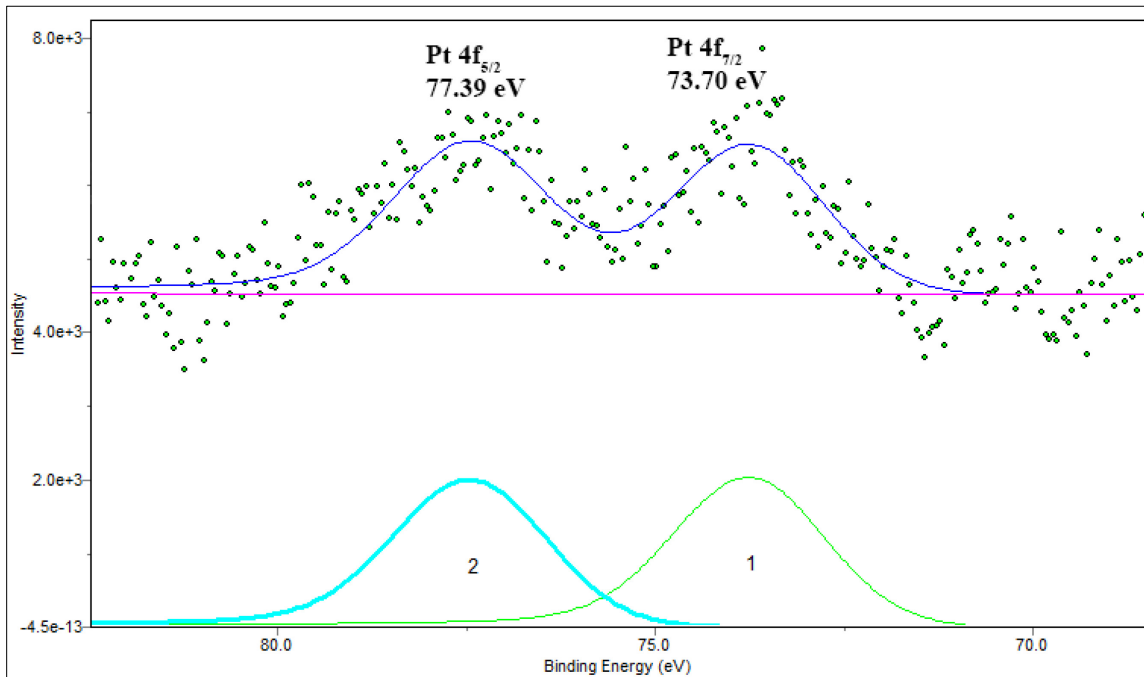


Figure 36. XPS data for the platinum 4f_{5/2} and 4f_{7/2} peaks of the 8 mM sample before pyrolysis.

Figure 37 shows the platinum XPS data for the 8 mM sample after pyrolysis. The platinum 4f_{7/2} peak at 71.16 eV corresponds to elemental platinum, which is typically reported in the range of 71.1-71.3 eV.^{97,98} Upon scanning the 840-900 eV region, no nickel 2p_{1/2} and 2p_{3/2} signals were found. This evidence supports the theory that platinum segregates to the surface, since XPS measurements only probe a few nanometers into the surface.

Despite prolonged scan times and collection attempts in multiple locations on the sample surface, no resolvable XPS signals corresponding to the catalyst material could be detected. The lower concentrations and loss of signal due to very high surface roughness and height variation on the carbon granule surface were the primary contributing factors.

Based on SEM images and EDS data, the outer surface concentration was much higher in the 8 mM sample, allowing for higher counts on the XPS detector.

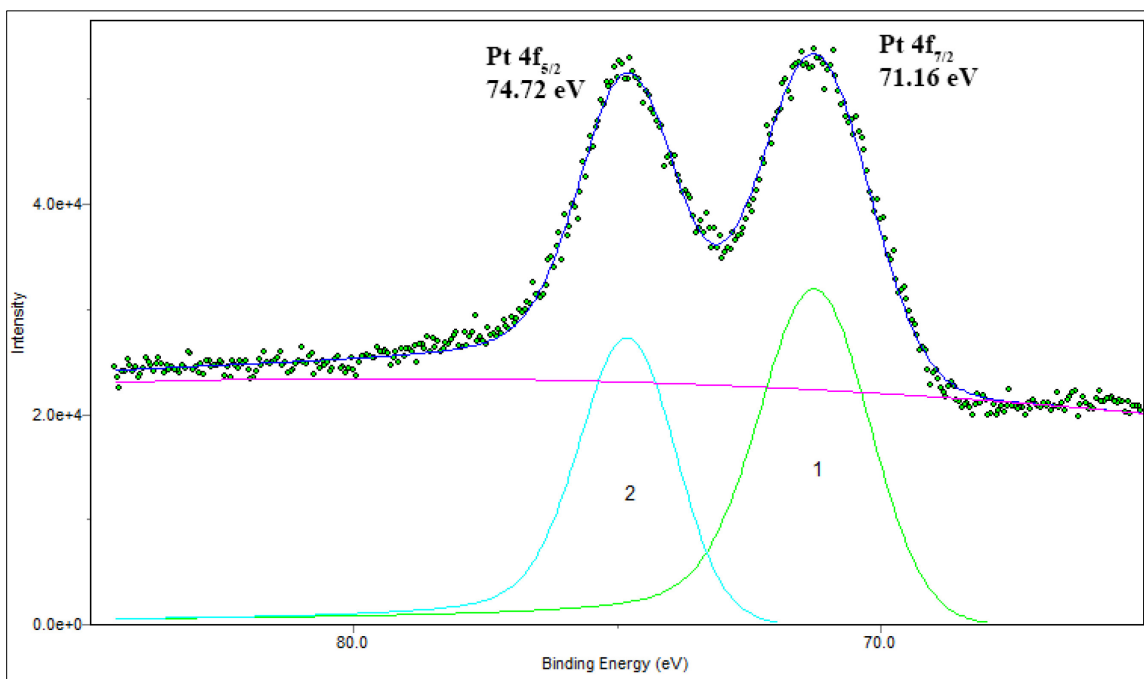


Figure 37. XPS data for the platinum $4f_{5/2}$ and $4f_{7/2}$ peaks of the 8 mM sample after pyrolysis.

The segregated structure indicated by XPS and EDS data contradicts the NiPt phase diagram for the bulk material. The calculated phase diagram for an NiPt system from Lu, et al. predicts a single NiPt phase in the entire temperature range of the reaction at a Pt mole fraction of 0.5.⁹⁹ Exceptions to this region of the phase diagram have been observed in nanoparticles by experimental and theoretical data.^{100,101} The segregation was shown to occur in a relatively short distance from the surface, and a single layer platinum shell formed on the surface. This short-range segregation helps to explain the lack of nickel in the XPS spectrum, but it does not completely explain the longer range segregation indicated by EDS data. One possible explanation is that the nickel atoms are reduced before the platinum atoms during the reduction process. Though

observed in a different system, previous work has shown that highly segregated core-shell Pt-Ru structures can be formed if one metal is reduced before the other in the reduction process.¹⁰² Despite the reason for the longer-range anomaly, the 8 mM sample does have a higher platinum concentration on the surface of its features. Based on the phase diagram, a true core-shell structure may be unlikely. A better approximation may be a gradient model, in which there is increasing nickel content toward the core of the features. . Since all of the catalysts were processed under the same pyrolysis conditions with the same precursor material, the data from the higher concentration 8 mM sample is likely representative of the series as a whole. The platinum shell would be much smaller on the 2 mM and 4 mM samples, likely resembling the single-layer platinum shell proposed by Wang, et al.¹⁰¹

3.1.4 The “Dip and Dry Method” – pH Modification

A pH modification step was added to the “dip and dry method” to release nickel(II) from the surface of the carbon. The proposed advantage of this method over the “precipitation method” was that any excess nickel(II) would be removed in the first solution, leaving just enough nickel(II) to cover the carbon surface in a monolayer of nanosheets. The pH was adjusted to 3 in the presence of excess potassium tetracyanoplatinate(II) so that a reaction would occur at the surface as the nickel(II) ions were released, forming the nanosheets on the surface of the carbon.

The SEM imaging and EDS data revealed that a very thin layer of NiPt(CN)₄ did grow on the surface of the carbon. The SEM image and EDS spectrum of the surface before pyrolysis are shown in Figures 38 and 39, respectively. The surface appeared relatively featureless, indicative of very small particle formation at the numerous well-

distributed nucleation sites on the carbon surface. The particles are either similar in size to the surface features of the activated carbon or too small to be resolved by SEM. The EDS spectrum revealed the presence of N, Pt, and Ni, though the amounts present were just above the limit of detection of the instrument. This sample resembled the 2 mM “precipitation method” sample, but the concentrations were lower.

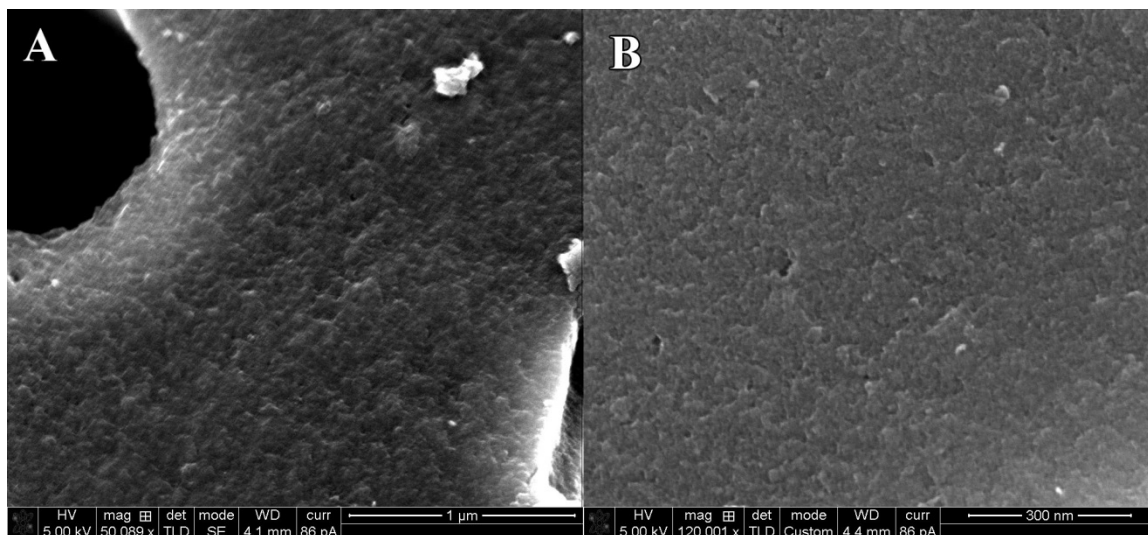


Figure 38. SEM images of the pH-modified “dip and dry method” sample before pyrolysis. The surface is shown at (A) 50,089x and (B) 120,001x magnification.

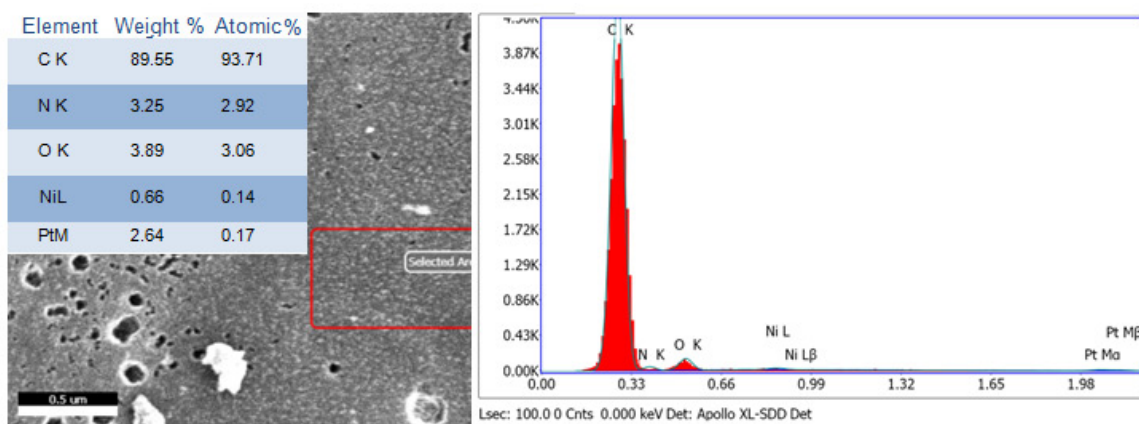


Figure 39. SEM image and EDS data from the pH-modified “dip and dry method” sample before pyrolysis.

The SEM image and EDS spectrum of the surface after pyrolysis are shown in Figures 40 and 41, respectively. Areas of metallic deposition could be seen. Most of the

features were dome-shaped and appeared to coat the nano-sized features on the surface of the carbon. Platinum and nickel were detected in the EDS spectrum. The result of pyrolysis was a very thin metallic Pt-Ni layer, with spherical features beginning to form. Due to the high percentage of exposure of the metals on the surface, this catalyst was expected to have the highest activity on a metal mass basis of all catalysts produced thus far.

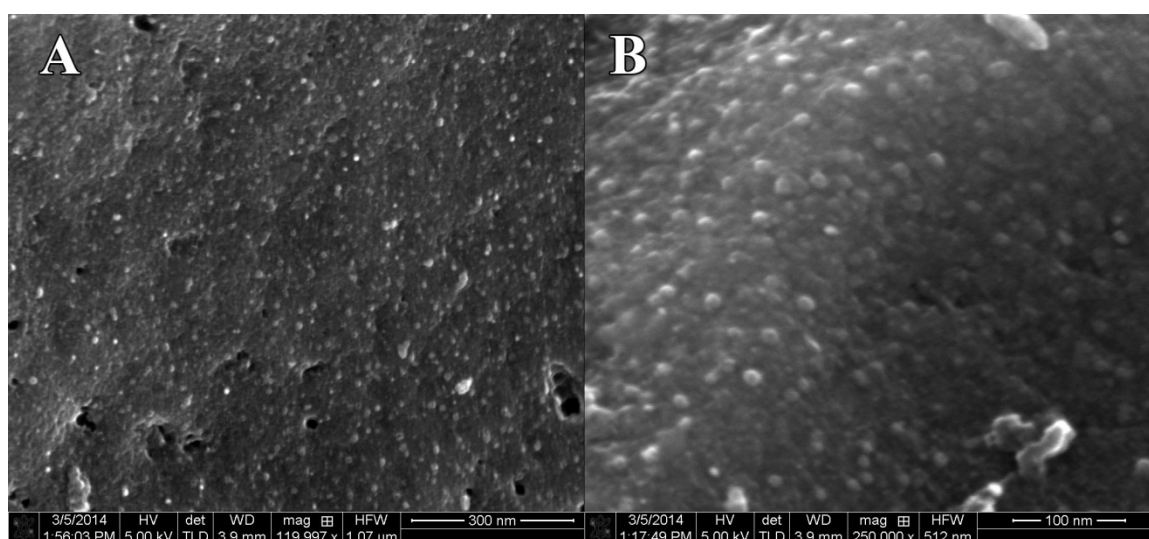


Figure 40. SEM images of the pH-modified "dip and dry method" sample after pyrolysis. The surface is shown at (A) 119,997x and (B) 250,000x magnification.

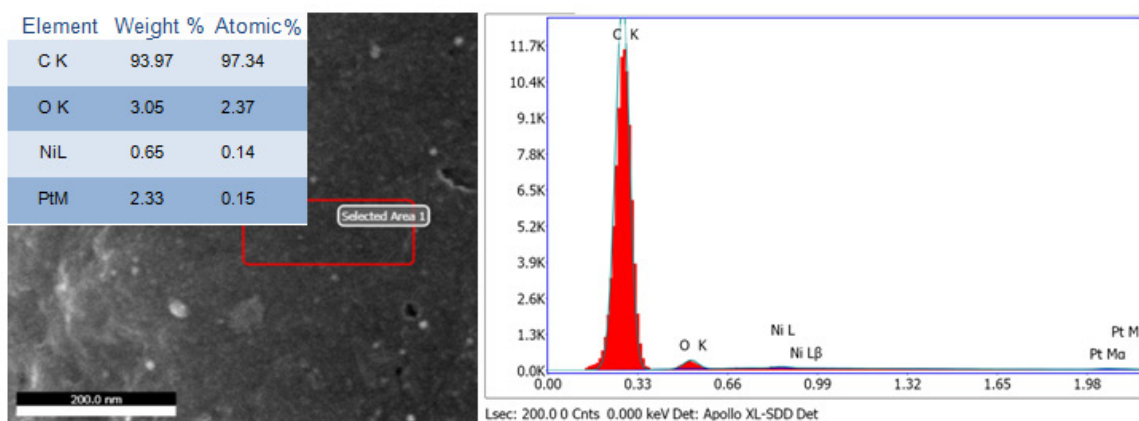


Figure 41. SEM image and EDS data from the pH-modified "dip and dry method" sample after pyrolysis.

3.1.5 ICP-AES Results

Nickel assays were performed on the catalysts to determine the metal loading on each sample. The platinum content in the “dip and dry” samples with no pH modification was unknown, so only the nickel content is reported. In samples produced via the remaining two methods, the Ni:Pt ratio in the precursor compound is 1:1, therefore the platinum is present in the same loading as nickel on a molar basis. Table 5 lists the results of the nickel assay on a weight percent basis, the calculated platinum content on a weight percent basis, and the associated loading of both metals on a molar basis. Figure 42 shows the reactant concentration versus Ni/Pt molar loading plot for all four of the samples produced via a pH-modified technique. The slope decreases in magnitude toward higher reactant concentration as the activated carbon surface becomes saturated with NiPt(CN)₄ nanosheet material during synthesis.

Table 5. Metal content of samples based on ICP-AES results.

Sample	Nickel (From ICP-AES)			Platinum (Calculated)		
	Loading (mg/g)	Wt %	mmol/g	Loading (mg/g)	Wt %	mmol/g
1/8th (1:20 Pt:Ni)	0.890	0.089%	0.0151	Unknown	-	-
1 (1:20 Pt:Ni)	3.608	0.361%	0.0612	Unknown	-	-
Dip and Dry-pH Mod.	0.921	0.092%	0.0156	3.048	0.305%	0.0156
Precip - 2 mM	2.490	0.249%	0.0422	8.240	0.824%	0.0422
Precip - 4 mM	3.120	0.312%	0.0529	10.325	1.032%	0.0529
Precip - 8 mM	3.530	0.353%	0.0599	11.682	1.168%	0.0599

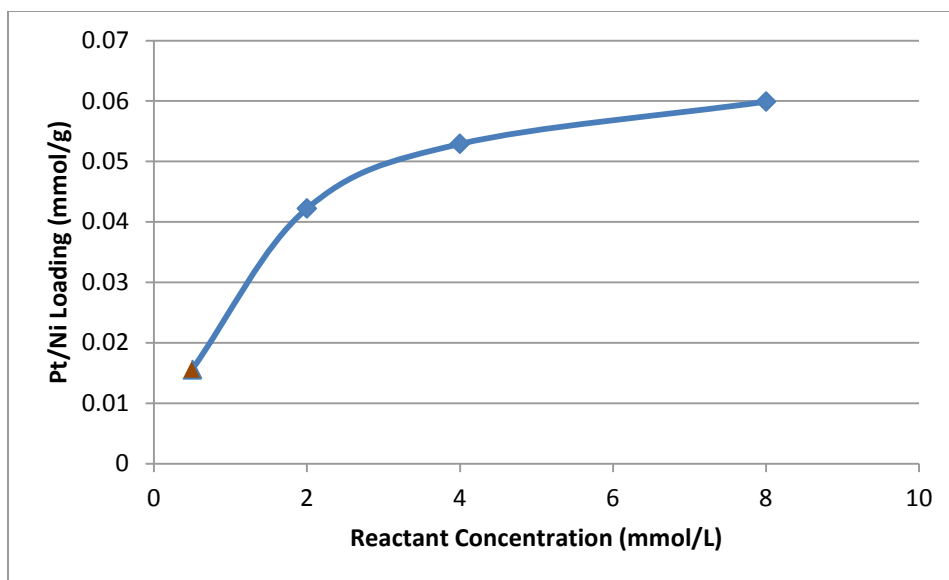


Figure 42. Molar loading versus reactant concentration. The triangle represents the data for the pH modified “dip and dry method”, and the diamond points represent the “precipitation method” data.

3.2 Styrene Hydrogenation Results

The $\text{PtNi}(\text{CN})_4$ nanosheet-derived Pt/Ni catalysts were tested in the hydrogenation of styrene to ethylbenzene. Plots of concentration versus time were generated by withdrawing small aliquots of sample from the reactor at regular intervals. The individual reactions were measured in a similar concentration range. Reactions were found to be zero-order initially and deviated to first-order at high conversion. This result is in agreement with previous work in which the Langmuir-Hinshelwood kinetic model was shown to fit styrene hydrogenation data.^{103,104} In this model, both the styrene and hydrogen bind to the solid surface of the metallic catalyst before reacting with each other to produce the hydrogenation product.

The concentration versus time plot for the pH-modified “dip and dry method” sample is shown in Figure 43. The plots for the 2 mM, 4 mM, and 8 mM “precipitation

method” samples are shown in Figures 44, 45, and 46, respectively. Figure 47 shows the reaction plot for the 8 mM standard catalyst. A linear regression is shown for the linear portion of plots corresponding to zero-order kinetics. Since the reaction is zero-order in this range, the slope is the rate constant and the rate of reaction.

The moles of styrene converted per hour, the moles of platinum in the reactor, and the ratio of moles of styrene converted per hour per mole of platinum are shown in Table 6. The ratio of the first two values represents the efficiency of the platinum metal in the catalyst. The catalyst prepared by the pH-modified “dip and dry method” has the highest ratio, therefore represents the most efficient use of platinum metal. The high homogeneity, high surface area, small particle size, and Ni-Pt alloying effect all play a role in the high efficiency of this catalyst. An increasing efficiency trend occurs from low to high concentration in the series of “precipitation method” catalysts. As concentration increases, the particle size on the surface grows, reducing surface area. This effect is countered as the sponge-like structures grow off the surface of the carbon in the 4 mM and 8 mM samples, effectively increasing the exposed platinum and surface area. The 8 mM samples had the most prolific growth of sponge-like structures, and this corresponds with the highest efficiency in the “precipitation method” series. The 8 mM “precipitation method” catalyst shows higher activity than the 8 mM platinum standard, primarily from the effect of the Ni-Pt alloy and platinum distribution on catalytic activity, since both catalysts have the same loading of platinum on the same substrate.

On a platinum metal basis, the pH-modified “dip and dry” method catalyst demonstrated 2.8x the catalytic activity of the standard, and the 8 mM “precipitation method catalyst demonstrated 1.4x the activity of the standard catalyst. The 2 mM and 4

mM catalysts showed 1.1x and 0.98x the activity of the standard catalyst on a platinum basis, respectively. Work by Betti, et al. showed up to a 1.3x increase in the styrene hydrogenation rate of a γ -Al₂O₃-supported bimetallic PtNi catalyst over a monometallic Pt catalyst, with a Pt loading of 1 wt% in all samples.¹⁰⁵ Wu et al. revealed that, when under the same conditions and time period in the hydrogenation of styrene, PtNi nanoparticles had a 1.5x higher percent conversion than Pt nanoparticles.¹⁰⁶ Though the tests performed in the aforementioned manuscripts were under slightly different conditions, the pH-modified “dip and dry method” sample compared favorably with a 2.8x increase in activity on a platinum metal basis.

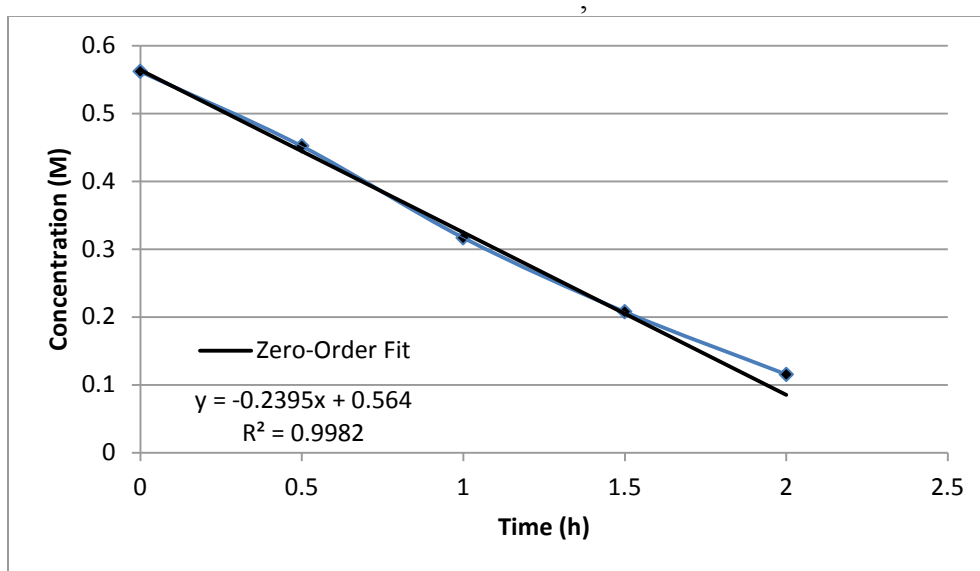


Figure 43. Concentration versus time plot for pH-modified “dip and dry method” catalyst.

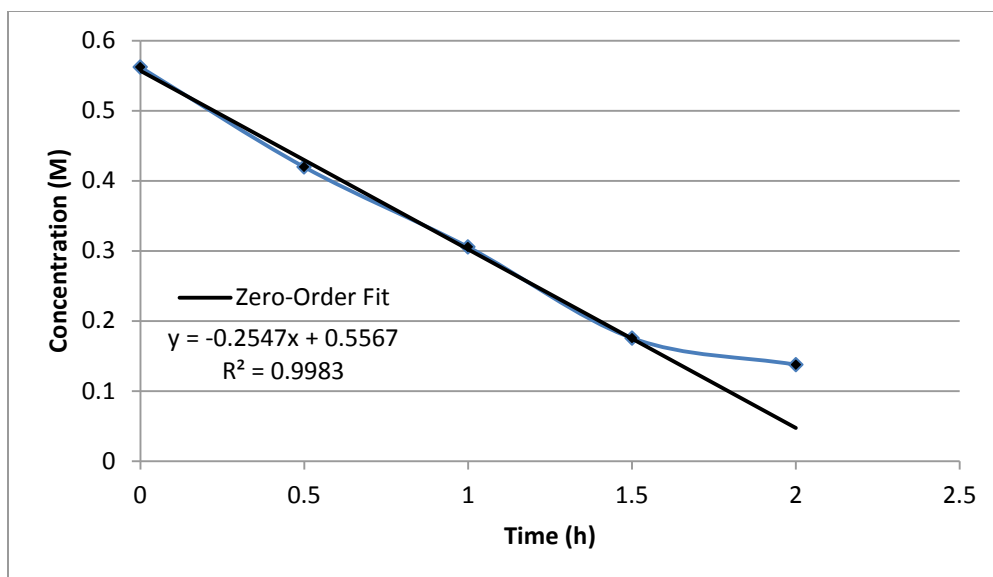


Figure 44. Concentration versus time plot for 2 mM “precipitation method” catalyst.

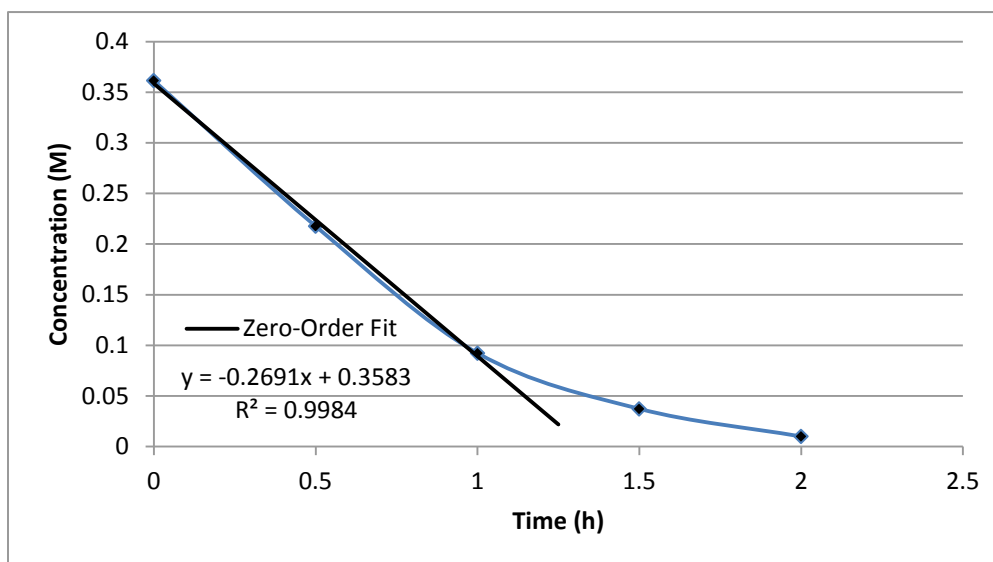


Figure 45. Concentration versus time plot for 4 mM “precipitation method” catalyst.

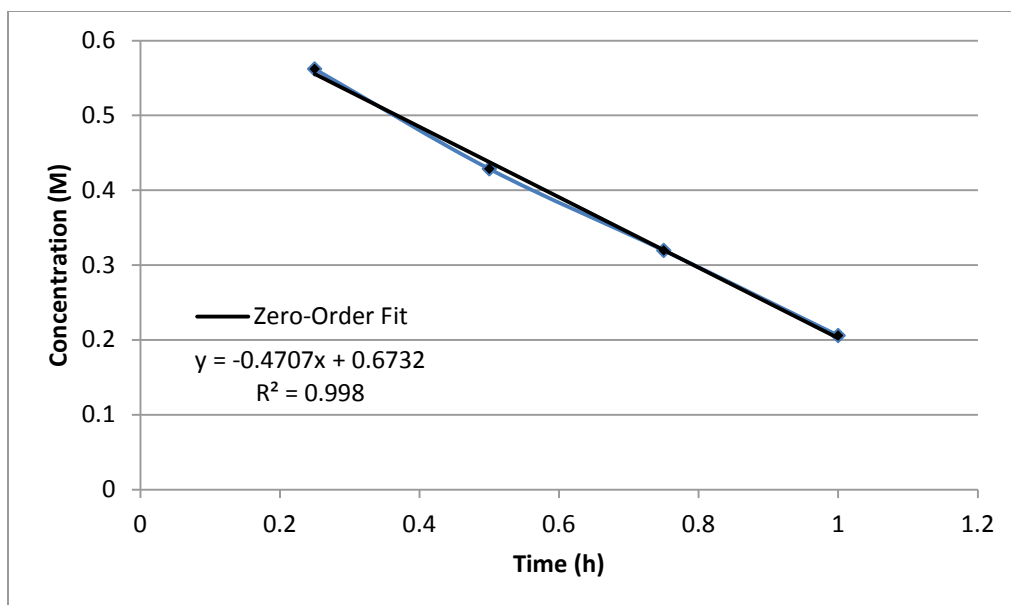


Figure 46. Concentration versus time plot for 8 mM “precipitation method” catalyst.

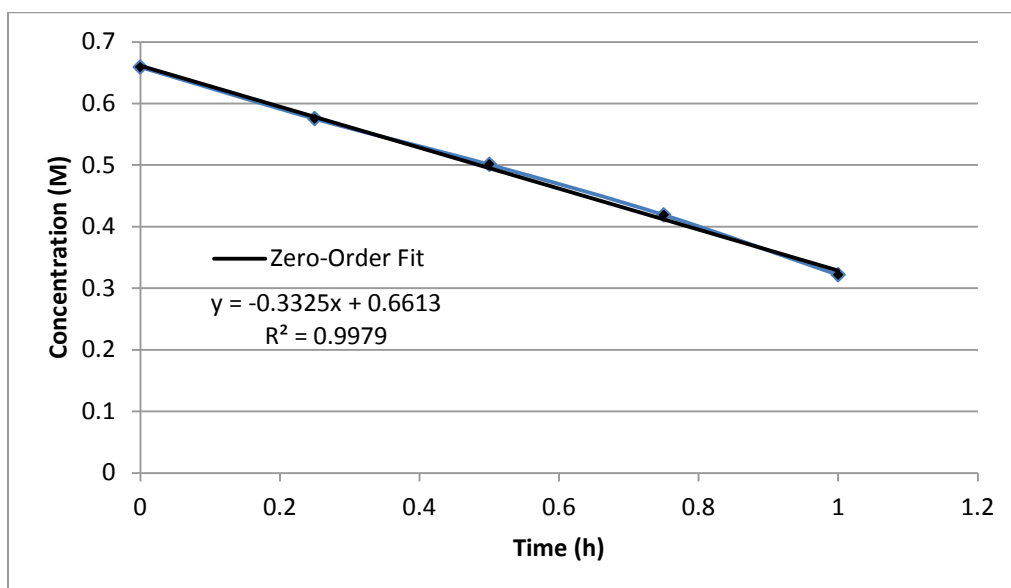


Figure 47. Concentration versus time plot for 8 mM standard catalyst.

Table 6. Styrene conversion on a platinum molar basis.

Sample	Moles styrene/hour	Moles Pt	Ratio
pH-modified "dip and dry" method	0.072	0.00234	30.7051282
2 mM "precipitation method"	0.076	0.00633	12.07109
4 mM "precipitation method"	0.086	0.00794	10.8733459
8 mM "precipitation method"	0.141	0.00899	15.7161937
8 mM platinum standard	0.100	0.00899	11.1018364

CHAPTER 4

Conclusions

4.1 Summary

The pH-modified “dip and dry method” and the “precipitation method” both resulted in the formation of $\text{NiPt}(\text{CN})_4$ nanosheets on the surface of the activated carbon substrate. Without lowering the pH to 3, the activated carbon substrate rendered the nickel(II) ions unable to participate in the reaction. Pyrolysis of the nanosheet-coated carbon yielded a Pt-Ni alloy. EDS and XPS data revealed that platinum had segregated to the surface in the 8 mM sample. The nanosheet-derived catalysts were compared to a traditional platinum catalyst. The pH-modified “dip and dry method” catalyst and the 8 mM precipitation method catalyst exhibited increased activity on a platinum metal basis. The pH-modified “dip and dry method” catalyst had 2.8x increase in activity on a platinum basis, attributed to high homogeneity, high surface area, small particle size, and Ni-Pt alloying effect.

4.2 Future Work

The results of this study have shown that cyanide-bridged metal nanosheets are effective precursors for high activity catalyst materials with reduced precious metal content. Exploration of these materials can be expanded into the following realms:

- Substrate-dependence study – The substrate may have profound effects on sheet formation, catalytic activity, and the preparation method employed.
- Use of other platinum group metals – Nanosheets can be formed using other catalytically active metals. For example, potassium tetracyanopalladate(II) could be substituted for potassium tetracyanoplatinate(II) in the preparation process,

yielding a Pd-Ni catalyst. The effect of varying the ratio of metals would prove beneficial to the catalyst properties. Research exploring the use of other alloys and metal ratios prepared via nanosheet precursors could reveal increased activity and selectivity in many cases.

- Testing in other catalytic processes – The Pt-Ni materials presented here were shown to have high catalytic activity in the hydrogenation of styrene, but this material would also be beneficial to other process that use platinum catalysts. This family of catalysts has high potential for use in fuel cells, autocatalysts, and other hydrogenation processes. The results of this study show that testing in these applications is warranted.
- Variation of preparation conditions – Reactant concentration, drying conditions, pyrolysis time, pyrolysis temperature, pyrolysis gas composition, and many other factors could influence the morphology, distribution, and activity of the catalyst material.

Exploration of the aforementioned factors would yield a catalyst material with an increase in catalytic activity and decrease in precious metal content higher than reported here. The catalysts reported in this work and any potential variations of this material would represent a significant environmental and economic impact upon commercialization of the technology.

APPENDIX SECTION

Appendix I

Internal Standard Calibration Data for GC Runs

GC FID Run Date: **2-4-2014**

Samples: “pH-modified dip and dry method” sample; 2 mM and 4 mM “precipitation method” samples

Table A1-1. Internal standard calibration integration results plot 1.

Styrene conc. (mM)	Styrene integ.	Decane conc. (mM)	Decane integ.	R
0.90	8720491	0.5	6134876	1.421462
0.45	3550881	0.5	4699186	0.755637
0.23	2671686	0.5	6572946	0.406467
0.11	728801	0.5	4896282	0.148848
0.06	446189	0.5	5069135	0.088021

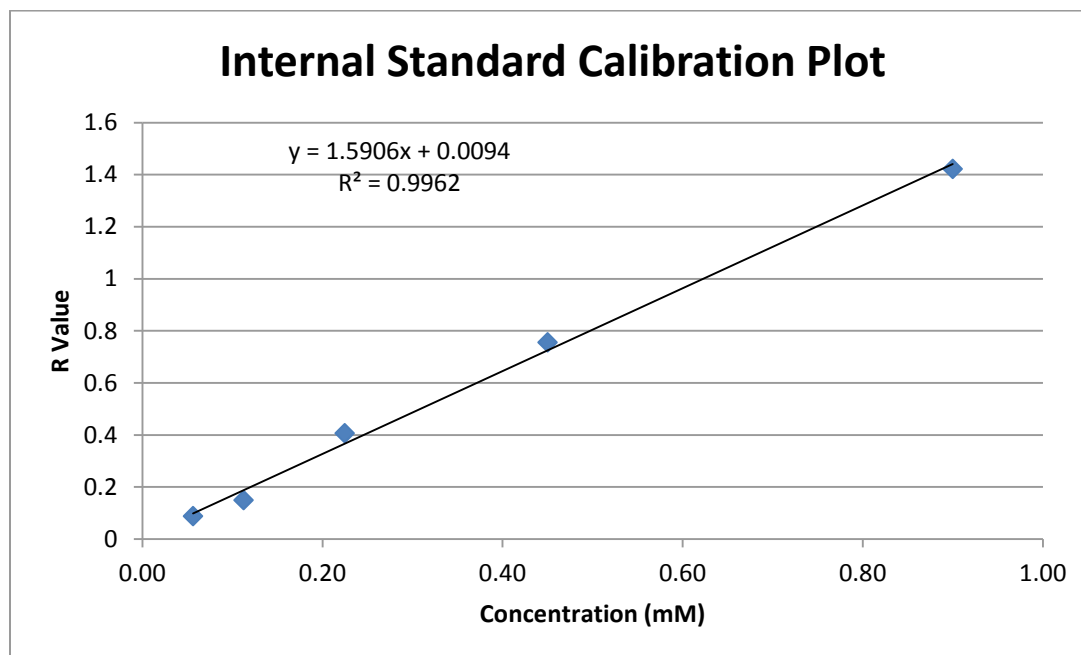


Figure A1-1. Internal standard calibration plot 1.

GC FID Run Date: **2-26-2014**

Samples: 8 mM “precipitation method” sample

Table A1-2. Internal standard calibration integration results plot 2.

Styrene conc. (mM)	Styrene integ.	Decane conc. (mM)	Decane integ.	R
0.90	6209778	0.5	4380053	1.41774
0.45	3639034	0.5	4945455	0.735834
0.23	2024138	0.5	5069284	0.399295
0.11	677728	0.5	4383864	0.154596
0.06	423833	0.5	4109041	0.103146

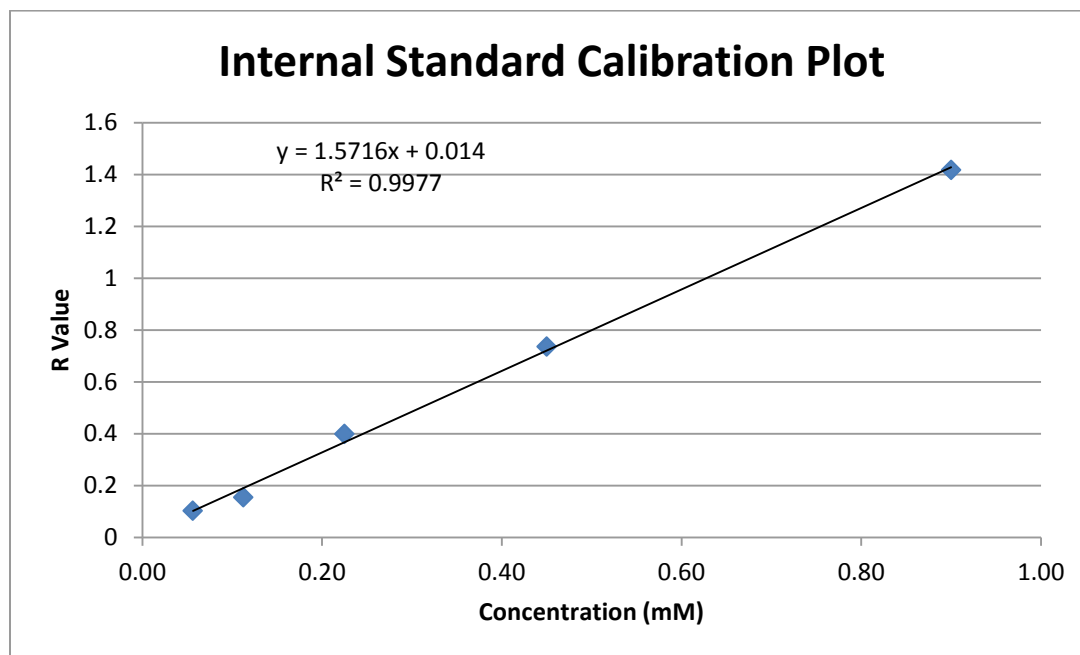


Figure A1-2. Internal standard calibration plot 2.

GC FID Run Date: **3-21-2014**

Sample: 3.530 mg/g platinum standard catalyst

Table A1-3. Internal standard calibration integration results plot 3.

Styrene conc. (mM)	Styrene integ.	Decane conc. (mM)	Decane integ.	R
0.90	7724663	0.5	5265963	1.466904
0.45	3872567	0.5	5160474	0.750429
0.23	2106494	0.5	5644612	0.373187
0.11	788454	0.5	5346735	0.147465
0.06	392212	0.5	4304338	0.09112

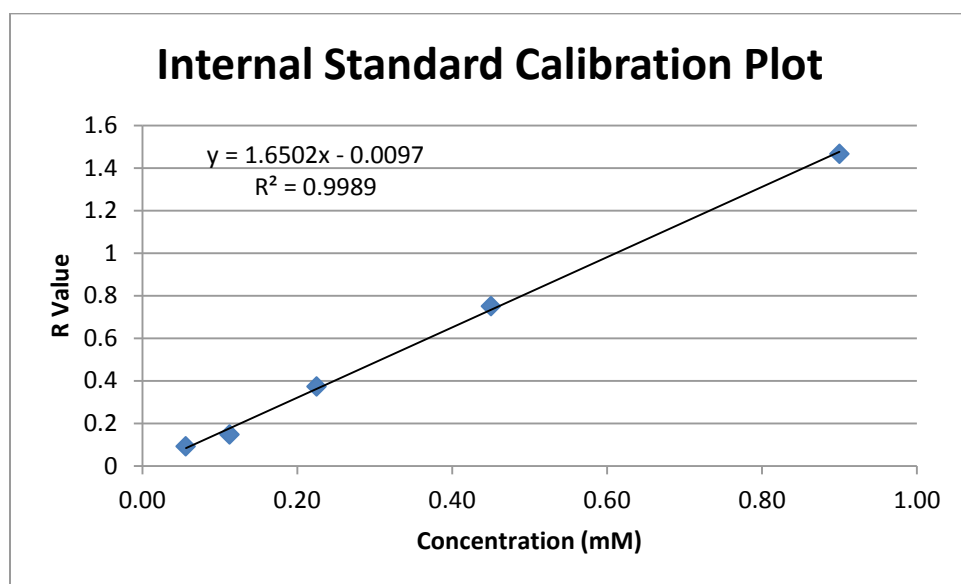


Figure A1-3. Internal standard calibration plot 3.

Appendix II

Monte Carlo Electron Trajectory Simulation Results with X-Ray Data

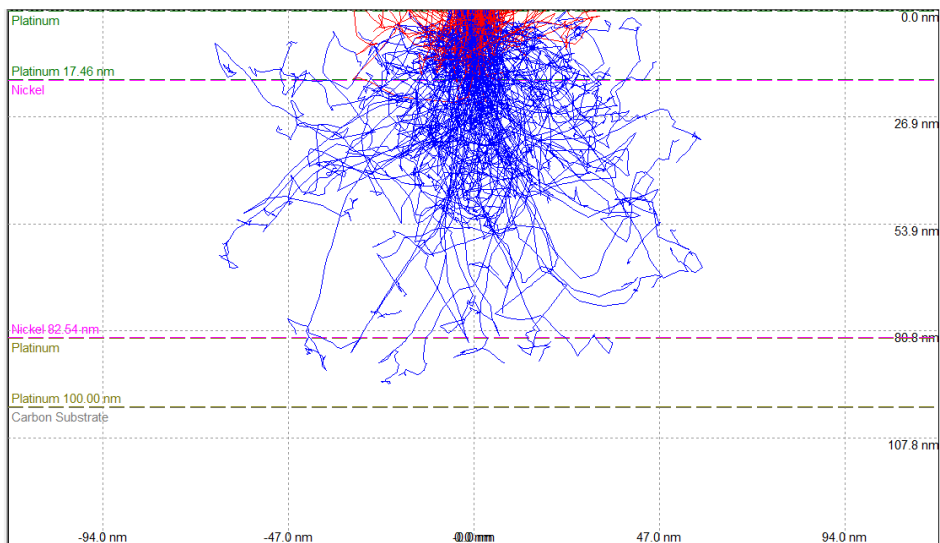


Figure A2-1. Electron trajectories in Monte Carlo simulation. This figure depicts the last 200 electron trajectories in the Pt-Ni-Pt-C model simulation.

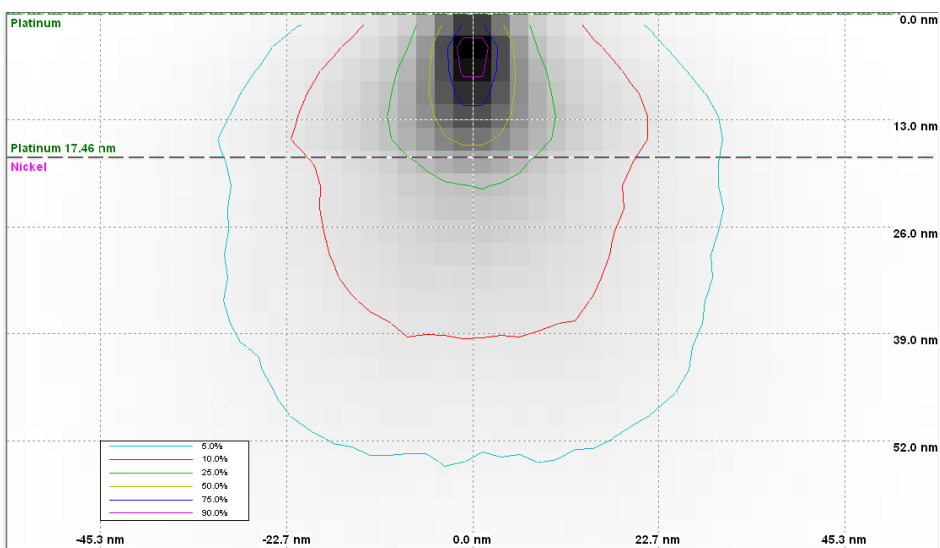


Figure A2-2. Electron energy by position. The relative electron energies are shown as a function of their position in the model material.

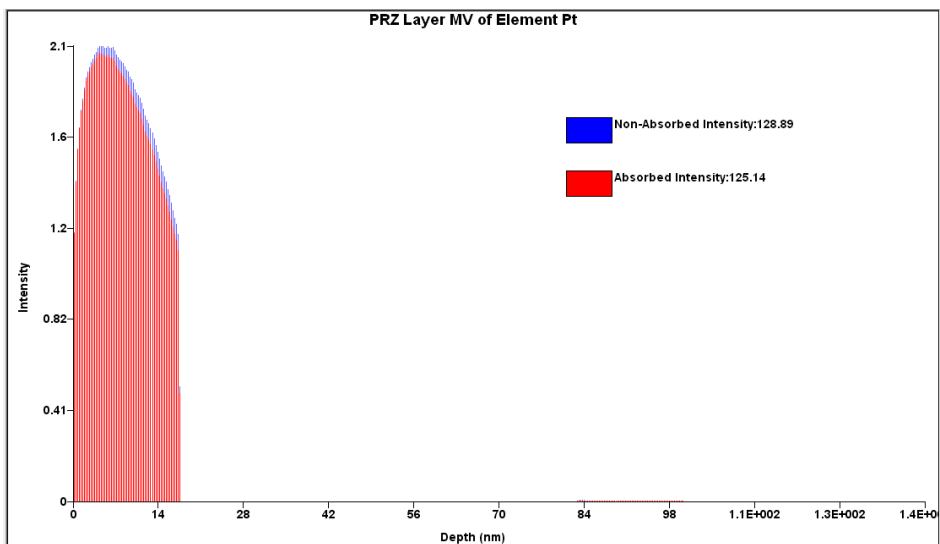


Figure A2-3. X-ray intensity as a function of depth from the sample surface – platinum. The “absorbed intensity” is the intensity of the X-rays that escape the sample surface and reach the detector.

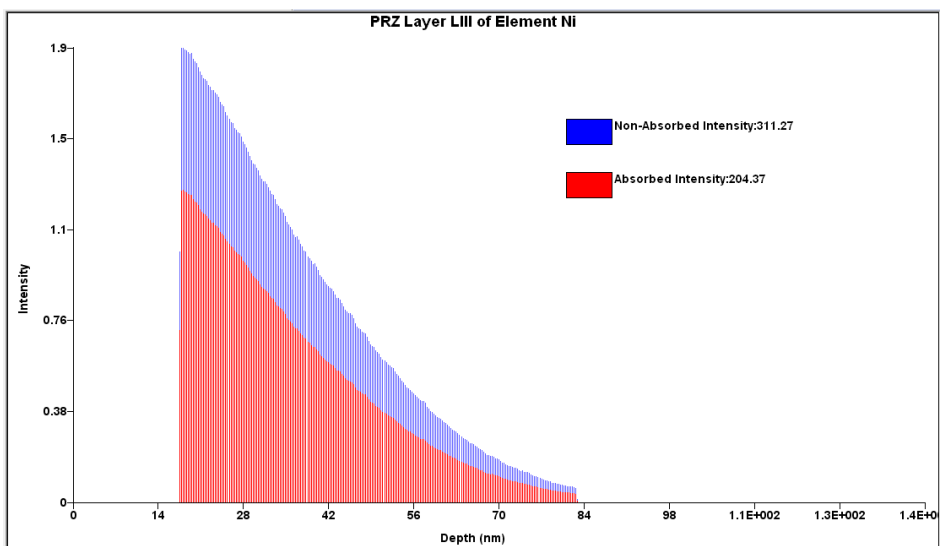


Figure A2-4. X-ray intensity as a function of depth from the sample surface – nickel. The “absorbed intensity” is the intensity of the X-rays that escape the sample surface and reach the detector.

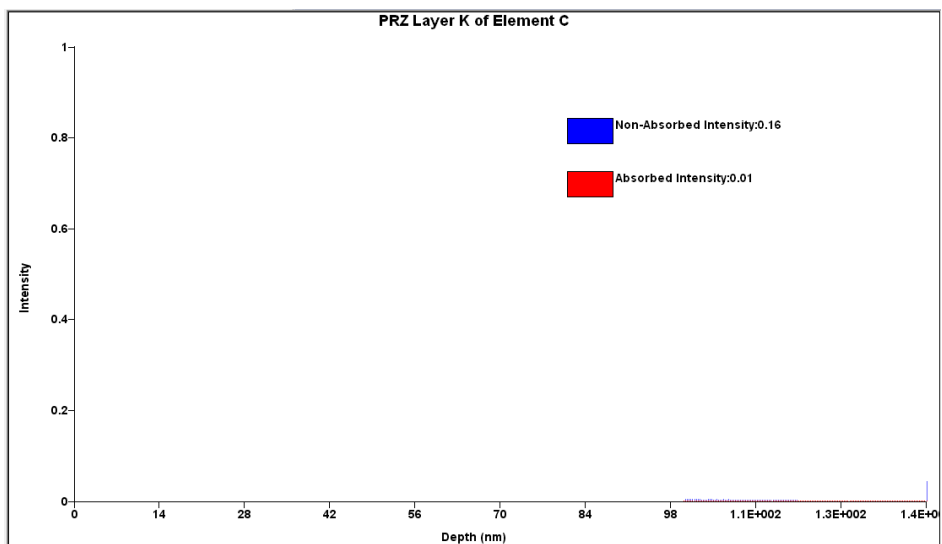


Figure A2-5. X-ray intensity as a function of depth from the sample surface – carbon. The “absorbed intensity” is the intensity of the X-rays that escape the sample surface and reach the detector. The intensity for carbon is so low that is barely visible in the plot.

Appendix III

Data from GC-FID Runs

Table A3-1. GC-FID data for hydrogenation with raw activated carbon.

Sample #	Styrene Integration	Decane Integration	R	styrene conc. (mM)	Corrected for Dilution (M)	Time (h)
1	9015038	5702098	1.581	0.7900	0.6876	0.00
2	9251899	5923535	1.562	0.7809	0.6796	1.00
3	8587121	5632858	1.524	0.7630	0.6641	2.00
4	7797274	5737195	1.359	0.6839	0.5952	3.00
5	10204360	7972460	1.280	0.6460	0.5622	4.00

Table A3-2. GC-FID data for hydrogenation with the 2 mM “precipitation method” catalyst.

Sample #	Styrene Integration	Decane Integration	R	styrene conc. (mM)	Corrected for Dilution (M)	Time (h)
1	4681703	4516504	1.037	0.6458	0.5621	0.00
2	3604749	4644524	0.776	0.4821	0.4195	0.50
3	2646578	4663635	0.567	0.3509	0.3054	1.00
4	1515092	4587939	0.330	0.2017	0.1756	1.50
5	1320546	5064945	0.261	0.1580	0.1375	2.00

Table A3-3. GC-FID data for hydrogenation with the 4 mM “precipitation method” catalyst.

Sample #	Styrene Integration	Decane Integration	R	styrene conc. (mM)	Corrected for Dilution (M)	Time (h)
1	3851283	5749364	0.670	0.4153	0.3614	0.00
2	1967000	4831982	0.407	0.2500	0.2176	0.50
3	807978	4537220	0.178	0.1061	0.0923	1.00
4	344778	4446030	0.078	0.0429	0.0373	1.50
5	127370	4607528	0.028	0.0115	0.0100	2.00

Table A3-4. GC-FID data for hydrogenation with the 8 mM “precipitation method” catalyst.

Sample #	Styrene Integration	Decane Integration	R	styrene conc. (mM)	Corrected for Dilution (M)	Time (h)
1 (Bad sample withdrawal)	6056386	4287775	1.412	0.8898	0.7744	0.00
2	5647389	5489887	1.029	0.6456	0.5619	0.25
3	3957504	5023214	0.788	0.4924	0.4285	0.50
4	2708552	4582034	0.591	0.3672	0.3196	0.75
5	1628987	4221210	0.386	0.2366	0.2059	1.00

Table A3-5. GC-FID data for hydrogenation with the pH-modified “dip and dry method” catalyst.

Sample #	Styrene Integration	Decane Integration	R	styrene conc. (mM)	Corrected for Dilution (M)	Time (h)
1	3961178	3824349	1.036	0.6453	0.5616	0.00
2	4563712	5466251	0.835	0.5190	0.4517	0.50
3	3782841	6432294	0.588	0.3638	0.3167	1.00
4	2233413	5748801	0.389	0.2384	0.2075	1.50
5	1207339	5485492	0.220	0.1325	0.1153	2.00

Table A3-6. GC-FID data for hydrogenation with the 8 mM platinum standard catalyst.

Sample #	styrene	decane	R	styrene conc. (mM)	Corrected for Dilution (M)	Time (h)
1	5918321	4772897	1.240	0.7573	0.6591	0.00
2	5639732	5217924	1.081	0.6608	0.5751	0.25
3	4652967	4951396	0.940	0.5753	0.5007	0.50
4	3829561	4880336	0.785	0.4814	0.4190	0.75
5	4427740	7379956	0.600	0.3694	0.3215	1.00

LITERATURE CITED

- 1) Harper S D. Preparation of lactone polymers using double metal cyanide catalysts. U.S. Patent 5032671, July 16, 1991
- 2) Grosch G H, Larbig H, Lorenz R, Junge D and Kammel U. Manufacture of supported double metal cyanide catalysts and their use for producing polyether alcohols. U.S. Patent 6,362,126, March 26, 2002
- 3) Iwamoto, T. Past, present and future of the clathrate inclusion compounds built of cyanometallate hosts *J. Incl. Phenom. Macro* **24**(1-2) 61-132 (1996).
- 4) Iwamoto, T., Nakano, T., Morita, M., Miyoshi, T., Miyamoto, T. & Sasaki, Y. The metal ammine cyanide aromatics clathrates. V. The Hofmann-type clathrate: $M(NH_3)_2M'(CN)_4 \cdot 2G$ *Inorg. Chim. Acta* **2**(3) 313-6 (1968).
- 5) Mathey, Y. & Mazieres, C. Phases of nickel(II) cyanide hydrates *Can. J. Chem.* **52**(21) 3637-44 (1974).
- 6) Niu, T., Crisci, G., Lu, J. & Jacobson, A. J. Diaquacobalt tetracyanonickelate hexahydrate. *Acta Cryst.* **54** 565-7 (1998).
- 7) Ham W K, Weakley T J R and Page C J 1993 Synthesis and crystal structure of $Cd(H_2O)_2Ni(CN)_4 \cdot 4H_2O$ *J. Solid State Chem.* 107(1) 101-7.
- 8) Nash, T. L., Beall, G. W., Lee, B. & Higgins, C. Modeling, Characterization, and Exfoliation of a New Family of 2-D Materials. *Science of Advanced Materials* **6**, 703–713 (2014).
- 9) “Fuel Cell Cost Analysis Summary”. International Partnership for Hydrogen and Fuel Cells in the Economy.
<http://www.iphe.net/docs/Resources/IPHE%20Fuel%20Cell%20Cost%20Comparison%20Report.pdf>. (Accessed October 25, 2012)
- 10) Technical Plan — Fuel Cells in *Fuel Cell Technologies Office Multi-Year Research, Development and Demonstration Plan*. Updated March, 2012.
http://www1.eere.energy.gov/hydrogenandfuelcells/mypp/pdfs/fuel_cells.pdf. (Accessed April 10, 2013)
- 11) Platinum Today: Platinum Charts. Johnson Matthey, 2012.
<http://www.platinum.matthey.com/publications/market-data-charts/platinum-charts/>. (Accessed October 22, 2012)

- 12) Platinum Today: Palladium Charts. Johnson Matthey, 2012.
<http://www.platinum.matthey.com/publications/market-data-charts/palladium-charts/>.
(Accessed October 22, 2012)
- 13) Platinum Today: Rhodium Charts. Johnson Matthey, 2012.
<http://www.platinum.matthey.com/publications/market-data-charts/rhodium-charts/>.
(Accessed October 22, 2012)
- 14) “Emission Control Catalysts”. IHS, November, 2011.
<http://www.ihs.com/products/chemical/planning/scup/emission-control-catalysts.aspx>.
(Accessed October 24, 2012)
- 15) Min, M.-K., Cho, J., Cho, K. & Kim, H. Particle size and alloying effects of Pt-based alloy catalysts for fuel cell applications. *Electrochimica Acta* **45**(25-26), 4211-4217 (2000).
- 16) Yang, H., Vogel, W., Lamy, C. & Alonso-Vante, N. Structure and Electrocatalytic Activity of Carbon-Supported Pt–Ni Alloy Nanoparticles Toward the Oxygen Reduction Reaction. *J. Phys. Chem. B* **108**, 11024–11034 (2004).
- 17) Jalan, V. & Taylor, E.J. Importance of Interatomic Spacing In Catalytic Reduction Of Oxygen In Phosphoric Acid. *J. Electrochem. Soc.*, **130** (1983), pp. 2299–2302.
- 18) Vogel, W. M. & Baris, J. M. The reduction of oxygen on platinum black in acid electrolytes. *Electrochimica Acta* **22**, 1259–1263 (1977).
- 19) Mukerjee, S., Srinivasan, S., Soriaga, M.P. & McBreen, J. Role of Structural and Electronic Properties of Pt and Pt Alloys on Electrocatalysis of Oxygen Reduction. *J. Electrochem. Soc.* **142**(5), 1409-1422 (1995).
- 20) Toda, T., Igarashi, H., Uchida, H. & Watanabe, M. Enhancement of the electroreduction of oxygen on Pt alloys with Fe, Ni, and Co. *Journal of the Electrochemical Society*. **46**(10), 3750-3756 (1999).
- 21) Wang, C. *et al.* Rational Development of Ternary Alloy Electrocatalysts. *J. Phys. Chem. Lett.* **3**, 1668–1673 (2012).
- 22) Liu, H. *et al.* A review of anode catalysis in the direct methanol fuel cell. *Journal of Power Sources* **155**, 95–110 (2006).
- 23) Martz, N., Roth, C. & Fueß, H. Characterization of different Pt/Metal/Complex catalysts as anode catalysts for the PEM fuel cell. *J Appl Electrochem* **35**, 85–90 (2005).

- 24) Cunningham, N., Irissou, E., Lefevre, M., Denis, M.-C., Guay, D. & Dodelet, J.-P. PEMFC Anode with Very Low Pt Loadings Using Pulsed Laser Deposition. *Electrochem. Solid-State Lett.* 1099-0062, **6**(7), A125 (2003).
- 25) Mukerjee, S., Srinivasan, S. & Appleby, A. J. Effect of sputtered film of platinum on low platinum loading electrodes on electrode kinetics of oxygen reduction in proton exchange membrane fuel cells. *Electrochimica Acta* **38**, 1661–1669 (1993).
- 26) Saha, M. S., Gullá, A. F., Allen, R. J. & Mukerjee, S. High performance polymer electrolyte fuel cells with ultra-low Pt loading electrodes prepared by dual ion-beam assisted deposition. *Electrochimica Acta* **51**, 4680–4692 (2006).
- 27) Secanella, M.; Karanb, K.; Sulemana, A. & Djilalia, N. Optimal Design of Ultralow-Platinum PEMFC Anode Electrodes *J. Electrochem. Soc.* **155**(2), B125-B134 (2008).
- 28) Abbet, S. *et al.* Acetylene Cyclotrimerization on Supported Size-Selected Pd_n Clusters (1 ≤ n ≤ 30): One Atom Is Enough! *J. Am. Chem. Soc.* **122**, 3453–3457 (2000).
- 29) Zhai, Y. *et al.* Alkali-Stabilized Pt-OH_x Species Catalyze Low-Temperature Water-Gas Shift Reactions. *Science* **329**, 1633–1636 (2010).
- 30) Thomas, J., Saghi, Z. & Gai, P. Can a Single Atom Serve as the Active Site in Some Heterogeneous Catalysts? *Topics in Catalysis* **54**, 588–594 (2011).
- 31) Kyriakou, G. *et al.* Isolated Metal Atom Geometries as a Strategy for Selective Heterogeneous Hydrogenations. *Science* **335**, 1209–1212 (2012).
- 32) Toshima, N.; Yonezawa, T. Bimetallic nanoparticles - novel materials for chemical and physical applications. *New J. Chem.* 1179 (1998).
- 33) Han, X., Zhou, R., Lai, G., Yue, B. & Zheng, X. Effect of transition metal (Cr, Mn, Fe, Co, Ni and Cu) on the hydrogenation properties of chloronitrobenzene over Pt/TiO₂ catalysts. *Journal of Molecular Catalysis A: Chemical* **209**, 83–87 (2004).
- 34) Lu, P., Teranishi, T., Asakura, K., Miyake, M. & Toshima, N. Polymer-Protected Ni/Pd Bimetallic Nano-Clusters: Preparation, Characterization and Catalysis for Hydrogenation of Nitrobenzene. *J. Phys. Chem. B* **103**, 9673–9682 (1999).
- 35) Bögner, W.; Krämer, M.; Krutsch, B.; Pischinger, S.; Voigtländer, D.; Wenninger, G.; Wirbeleit, F.; Brogan, M.S.; Brisley, R.J. & Webster, D.E. Removal of nitrogen oxides from the exhaust of a lean-tune gasoline engine. *Appl. Catal. B: Environ.* **7**, 153 (1995).

- 36) Gill, L., Blakeman, P., Twigg, M. & Walker, A. The Use of NO_x Adsorber Catalysts on Diesel Engines. *Topics in Catalysis* **28**, 157–164 (2004).
- 37) Twigg, M. V. Progress and future challenges in controlling automotive exhaust gas emissions. *Applied Catalysis B: Environmental* **70**, 2–15 (2007).
- 38) Epling, W. S., Campbell, L. E., Yezerets, A., Currier, N. W. & Parks, J. E. Overview of the Fundamental Reactions and Degradation Mechanisms of NO_x Storage/Reduction Catalysts. *Catalysis Reviews* **46**, 163–245 (2004).
- 39) Burch, R., Millington, P. J. & Walker, A. P. Mechanism of the selective reduction of nitrogen monoxide on platinum-based catalysts in the presence of excess oxygen. *Applied Catalysis B: Environmental* **4**, 65–94 (1994).
- 40) Yu, W., Porosoff, M. D. & Chen, J. G. Review of Pt-Based Bimetallic Catalysis: From Model Surfaces to Supported Catalysts. *Chem. Rev.* **112**, 5780–5817 (2012).
- 41) Pinna, F. Supported metal catalysts preparation. *Catalysis Today* **41**, 129–137 (1998).
- 42) Silvestre-Albero, J., Serrano-Ruiz, J. C., Sepúlveda-Escribano, A. & Rodríguez-Reinoso, F. Modification of the catalytic behaviour of platinum by zinc in crotonaldehyde hydrogenation and iso-butane dehydrogenation. *Applied Catalysis A: General* **292**, 244–251 (2005).
- 43) I. Albertazzi, S., Busca, G., Finocchio, E., Glöckler, R. & Vaccari, A. New Pd/Pt on Mg/Al basic mixed oxides for the hydrogenation and hydrogenolysis of naphthalene. *Journal of Catalysis* **223**, 372–381 (2004).
- 44) Jongpatiwut, S. *et al.* Competitive hydrogenation of poly-aromatic hydrocarbons on sulfur-resistant bimetallic Pt-Pd catalysts. *Applied Catalysis A: General* **262**, 241–253 (2004).
- 45) Plomp, A. J. *et al.* Catalysts based on platinum–tin and platinum–gallium in close contact for the selective hydrogenation of cinnamaldehyde. *Journal of Catalysis* **263**, 146–154 (2009).
- 46) M. Kotter, L. Riekert, in: B. Delmon, P. Grange, P. A. Jacobs, G. Poncelet (Eds.), *Preparation of Catalysts II*, Elsevier, Amsterdam, 1979, p. 51
- 47) J.P. Boumonville, J. P. Franck, G. Martino, in: G. Poncelet, P. Grange, P. A. Jacobs (Eds.), *Preparation of Catalysts III*, Elsevier, Amsterdam, 1983, p. 81.
- 48) Shu, Y. *et al.* The effect of impregnation sequence on the hydrogenation activity and selectivity of supported Pt/Ni bimetallic catalysts. *Applied Catalysis A: General* **339**, 169–179 (2008).

- 49) Lonergan, W. W., Vlachos, D. G. & Chen, J. G. Correlating extent of Pt–Ni bond formation with low-temperature hydrogenation of benzene and 1,3-butadiene over supported Pt/Ni bimetallic catalysts. *Journal of Catalysis* **271**, 239–250 (2010).
- 50) Candy, J.-P., Didillon, B., Smith, E. L., Shay, T. B. & Basset, J.-M. Surface organometallic chemistry on metals: a novel and effective route to custom-designed bimetallic catalysts. *Journal of Molecular Catalysis* **86**, 179–204 (1994).
- 51) Tsao, Ying-Yen P. "Multimetallic catalysts and their method of preparation from organometallic precursors." U.S. Patent No. 4,513,098. 23 Apr. 1985.
- 52) Merlo, A. B., Vetere, V., Ruggera, J. F. & Casella, M. L. Bimetallic PtSn catalyst for the selective hydrogenation of furfural to furfuryl alcohol in liquid-phase. *Catalysis Communications* **10**, 1665–1669 (2009).
- 53) Koh, A. C. W. *et al.* Ethanol steam reforming over supported ruthenium and ruthenium–platinum catalysts: Comparison of organometallic clusters and inorganic salts as catalyst precursors. *International Journal of Hydrogen Energy* **34**, 5691–5703 (2009).
- 54) Graf, I. V. G. *et al.* Cluster Chemistry on Surfaces: Characterization and Catalytic Studies of Phosphine-Stabilized Platinum–Gold Clusters on Silica and Alumina Supports. *Inorg. Chem.* **35**, 689–694 (1996).
- 55) Chandler, B. D., Schabel, A. B. & Pignolet, L. H. Preparation and Characterization of Supported Bimetallic Pt–Au and Pt–Cu Catalysts from Bimetallic Molecular Precursors. *Journal of Catalysis* **193**, 186–198 (2000).
- 56) Chandler, B. D. & Pignolet, L. H. DRIFTS studies of carbon monoxide coverage on highly dispersed bimetallic Pt–Cu and Pt–Au catalysts. *Catalysis Today* **65**, 39–50 (2001).
- 57) Ugo, R., Dossi, C. & Psaro, R. Molecular metal carbonyl clusters and volatile organometallic compounds for tailored mono and bimetallic heterogeneous catalysts. *Journal of Molecular Catalysis A: Chemical* **107**, 13–22 (1996).
- 58) Alexeev, O. S. & Gates, B. C. Supported Bimetallic Cluster Catalysts. *Ind. Eng. Chem. Res.* **42**, 1571–1587 (2002).
- 59) Hurtado-Juan, M.-A., Yeung, C. M. Y. & Tsang, S. C. A study of co-precipitated bimetallic gold catalysts for water–gas shift reaction. *Catalysis Communications* **9**, 1551–1557 (2008).
- 60) Telkar, M. M., Nadgeri, J. M., Rode, C. V. & Chaudhari, R. V. Role of a co-metal in bimetallic Ni–Pt catalyst for hydrogenation of m-dinitrobenzene to m-phenylenediamine. *Applied Catalysis A: General* **295**, 23–30 (2005).

- 61) Sandoval, A., Aguilar, A., Louis, C., Traverse, A. & Zanella, R. Bimetallic Au–Ag/TiO₂ catalyst prepared by deposition–precipitation: High activity and stability in CO oxidation. *Journal of Catalysis* **281**, 40–49 (2011).
- 62) Prüsse, U. & Vorlop, K.-D. Supported bimetallic palladium catalysts for water-phase nitrate reduction. *Journal of Molecular Catalysis A: Chemical* **173**, 313–328 (2001).
- 63) J. W. Geus, in: G. Poncelet, P. Grange, P. A. Jacobs (Eds.), *Preparation of Catalysts III*, Elsevier, Amsterdam, 1983, p.1.
- 64) Veisz, B. *et al.* Palladium-platinum powder catalysts manufactured by colloid synthesis: I. Preparation and characterization. *Journal of Molecular Catalysis A: Chemical* **238**, 56–62 (2005).
- 65) Alayoglu, S. *et al.* CO₂ Hydrogenation Studies on Co and CoPt Bimetallic Nanoparticles Under Reaction Conditions Using TEM, XPS and NEXAFS. *Top Catal* **54**, 778–785 (2011).
- 66) Bonnemann, H., *et al.* Nanoscopic Pt-bimetal colloids as precursors for PEM fuel cell catalysts." *Journal of New Materials for Electrochemical Systems* **3.3** (2000): 199-206.
- 67) Roucoux, Alain, Jürgen Schulz, and Henri Patin. Reduced transition metal colloids: a novel family of reusable catalysts? *Chemical Reviews* **102.10** (2002): 3757-3778.
- 68) Nilekar, A. U., Alayoglu, S., Eichhorn, B. & Mavrikakis, M. Preferential CO Oxidation in Hydrogen: Reactivity of Core–Shell Nanoparticles. *J. Am. Chem. Soc.* **132**, 7418–7428 (2010).
- 69) Mayrhofer, Karl JJ, *et al.* "Adsorbate-Induced Surface Segregation for Core–Shell Nanocatalysts." *Angewandte Chemie International Edition* **48.19** (2009): 3529-3531.
- 70) Yang, X., Cheng, F., Liang, J., Tao, Z. & Chen, J. Carbon-supported Ni_{1-x}@Pt_x (x = 0.32, 0.43, 0.60, 0.67, and 0.80) core–shell nanoparticles as catalysts for hydrogen generation from hydrolysis of ammonia borane. *International Journal of Hydrogen Energy* **36**, 1984–1990 (2011).
- 71) Zhang, X.-B., Yan, J.-M., Han, S., Shioyama, H. & Xu, Q. Magnetically Recyclable Fe@Pt Core–Shell Nanoparticles and Their Use as Electrocatalysts for Ammonia Borane Oxidation: The Role of Crystallinity of the Core. *J. Am. Chem. Soc.* **131**, 2778–2779 (2009).
- 72) Cheney, B. A., Lauterbach, J. A. & Chen, J. G. Reverse micelle synthesis and characterization of supported Pt/Ni bimetallic catalysts on γ -Al₂O₃. *Applied Catalysis A: General* **394**, 41–47 (2011).

- 73) Zhang, X., Tsang, K.-Y. & Chan, K.-Y. Electrocatalytic properties of supported platinum–cobalt nanoparticles with uniform and controlled composition. *Journal of Electroanalytical Chemistry* **573**, 1–9 (2004).
- 74) Ekou, T., Vicente, A., Lafaye, G., Especel, C. & Marecot, P. Bimetallic Rh-Ge and Pt-Ge catalysts supported on TiO₂ for citral hydrogenation: I. Preparation and characterization of the catalysts. *Applied Catalysis A: General* **314**, 64–72 (2006).
- 75) Ekou, T., Vicente, A., Lafaye, G., Especel, C. & Marecot, P. Bimetallic Rh-Ge and Pt-Ge catalysts supported on TiO₂ for citral hydrogenation: II. Catalytic properties. *Applied Catalysis A: General* **314**, 73–80 (2006).
- 76) Plomp, A. J. *et al.* Catalysts based on platinum–tin and platinum–gallium in close contact for the selective hydrogenation of cinnamaldehyde. *Journal of Catalysis* **263**, 146–154 (2009).
- 77) Margitfalvi, J. L., Borbáth, I., Hegedűs, M. & Tompos, A. Preparation of new type of Sn-Pt/SiO₂ catalysts for carbonyl activation. *Applied Catalysis A: General* **229**, 35–49 (2002).
- 78) Scott, R. W. J. *et al.* Titania-Supported PdAu Bimetallic Catalysts Prepared from Dendrimer-Encapsulated Nanoparticle Precursors. *J. Am. Chem. Soc.* **127**, 1380–1381 (2005).
- 79) Scott, Robert WJ, Orla M. Wilson, and Richard M. Crooks. "Synthesis, characterization, and applications of dendrimer-encapsulated nanoparticles." *The Journal of Physical Chemistry B* **109**.2 (2005): 692-704.
- 80) Albiter, M. A., Morales, R. & Zaera, F. Dendrimer-based synthesis of Pt catalysts for hydrocarbon conversion. *Applied Catalysis A: General* **391**, 386–393 (2011).
- 81) Guo, Z. *et al.* Carbon nanotube-supported Pt-based bimetallic catalysts prepared by a microwave-assisted polyol reduction method and their catalytic applications in the selective hydrogenation. *Journal of Catalysis* **276**, 314–326 (2010).
- 82) Di Noto, V. & Negro, E. Pt–Fe and Pt–Ni Carbon Nitride-Based ‘Core–Shell’ ORR Electrocatalysts for Polymer Electrolyte Membrane Fuel Cells. *Fuel Cells* **10**, 234–244 (2010).
- 83) Di Noto, V. *et al.* Pt and Ni carbon nitride electrocatalysts for the oxygen reduction reaction. *Journal of The Electrochemical Society* **154**, B745–B756 (2007).
- 84) Negro, E. & Di Noto, V. Polymer electrolyte fuel cells based on bimetallic carbon nitride electrocatalysts. *Journal of Power Sources* **178**, 634–641 (2008).

- 85) Di Noto, V. & Negro, E. Development of nano-electrocatalysts based on carbon nitride supports for the ORR processes in PEM fuel cells. *Electrochimica Acta* **55**, 7564–7574 (2010).
- 86) Di Noto, V., Negro, E., Lavina, S., Gross, S. & Pace, G. Pd-Co carbon-nitride electrocatalysts for polymer electrolyte fuel cells. *Electrochimica Acta* **53**, 1604–1617 (2007).
- 87) Di Noto, V.; Negro, E.; Lavina, S., Pace, G. Electrocatalysts based on mono/plurimetallic carbon nitrides for polymer electrolyte membrane fuel cells fuelled with hydrogen (pemfc) and methanol (dmfc) and for hydrogen electrogenerators. US Patent 8158548, April 17, 2012.
- 88) Aksoylu, A. E., Madalena, M., Freitas, A., Pereira, M. F. R. & Figueiredo, J. L. The effects of different activated carbon supports and support modifications on the properties of Pt/AC catalysts. *Carbon* **39**, 175–185 (2001).
- 89) Regalbuto, J. R. Dry impregnation of platinum on a carbon substrate. U.S. Patent 20070105007, May 10, 2007.
- 90) Okhlopkova, L., Lisitsyn, A., Likholobov, V., Gurrath, M. & Boehm, H. Properties of Pt/C and Pd/C catalysts prepared by reduction with hydrogen of adsorbed metal chlorides: Influence of pore structure of the support. *Applied Catalysis A: General* **204**, 229–240 (2000).
- 91) Rodríguez-Reinoso, F. & Molina-Sabio, M. Textural and chemical characterization of microporous carbons. *Advances in Colloid and Interface Science* **76–77**, 271–294 (1998).
- 92) Kadirvelu, K., Thamaraiselvi, K. & Namasivayam, C. Adsorption of nickel(II) from aqueous solution onto activated carbon prepared from coirpith. *Separation and Purification Technology* **24**, 497–505 (2001).
- 93) Kumar, A. N., Harish, S. & Joseph, J. New route for the synthesis of electrocatalytic Ni (OH) 2 modified electrodes–Electro-oxidation of borohydride as probe reaction. *Bulletin of Materials Science*, Forthcoming article BOMS-D-12-00738. (<http://www.ias.ac.in/maternal/forthcoming/bms/BOMS-D-12-00738.pdf>)
- 94) Heibel, M., Kumar, G., Wyse, C., Bukovec, P. & Bocarsly, A. B. Use of Sol–Gel Chemistry for the Preparation of Cyanogels as Ceramic and Alloy Precursors. *Chem. Mater.* **8**, 1504–1511 (1996).
- 95) Vondrova, M., McQueen, T. M., Burgess, C. M., Ho, D. M. & Bocarsly, A. B. Autoreduction of Pd–Co and Pt–Co Cyanogels: Exploration of Cyanometalate Coordination Chemistry at Elevated Temperatures. *J. Am. Chem. Soc.* **130**, 5563–5572 (2008).

- 96) Hanks T.W., Ekeland R.A., Emerson K., Larsen R.D. & Jennings P.W. *Organometallics* **6**, 28 (1987). Available from the NIST XPS Database. <http://srdata.nist.gov/xps/> (accessed 3/17/2014).
- 97) Thiele J., Barrett N.T., Belkhou R., Guillot C. & Koundi H. *J. Phys. Cond. Matter* **6**, 5025 (1994). Available from the NIST XPS Database. <http://srdata.nist.gov/xps/> (accessed 3/17/2014).
- 98) Alnot M., Gorodetskii V., Cassuto A., Ehrhardt J.J. *Thin Solid Films* **151**, 251 (1987). Available from the NIST XPS Database. <http://srdata.nist.gov/xps/> (accessed 3/17/2014).
- 99) Lu, X.-G., Sundman, B. & Ågren, J. Thermodynamic assessments of the Ni–Pt and Al–Ni–Pt systems. *Calphad* **33**, 450–456 (2009).
- 100) Cui, C., Gan, L., Heggen, M., Rudi, S. & Strasser, P. Compositional segregation in shaped Pt alloy nanoparticles and their structural behaviour during electrocatalysis. *Nat Mater* **12**, 765–771 (2013).
- 101) Wang, G., Van Hove, M. A., Ross, P. N. & Baskes, M. I. Monte Carlo simulations of segregation in Pt–Ni catalyst nanoparticles. *The Journal of Chemical Physics*, **122**, 024706 (2005).
- 102) Vinodgopal, K., He, Y., Ashokkumar, M. & Grieser, F. Sonochemically Prepared Platinum–Ruthenium Bimetallic Nanoparticles. *J. Phys. Chem. B* **110**, 3849–3852 (2006).
- 103) Nijhuis, T. A., Dautzenberg, F. M. & Moulijn, J. A. Modeling of monolithic and trickle-bed reactors for the hydrogenation of styrene. *Chemical Engineering Science* **58**, 1113–1124 (2003).
- 104) Badano, J., Lederhos, C., Quiroga, M., L’Argentièrre, P. & Coloma-Pascual, F. Low metal loading catalysts used for the selective hydrogenation of styrene. *Quimica Nova* **33**, 48–51 (2010).
- 105) Betti, C. *et al.* Effect of the sequence of impregnation on the activity and sulfur resistance of Pt–Ni/ γ -Al₂O₃ bimetallic catalysts for the selective hydrogenation of styrene. *Applied Catalysis A: General* **435–436**, 181–186 (2012).
- 106) Wu, Y., Cai, S., Wang, D., He, W. & Li, Y. Syntheses of Water-Soluble Octahedral, Truncated Octahedral, and Cubic Pt–Ni Nanocrystals and Their Structure–Activity Study in Model Hydrogenation Reactions. *J. Am. Chem. Soc.* **134**, 8975–8981 (2012).